

# **Dynamics of Rydberg atom lattices in the presence of noise and dissipation**

DISSERTATION

zur Erlangung des akademischen Grades

**Doctor rerum naturalium  
(Dr. rer. nat.)**

**vorgelegt**

**der Fakultät Mathematik und Naturwissenschaften  
der Technischen Universität Dresden**

**von**

Wildan Abdussalam M.Sc.

geboren am 21.05.1986 in Bandung

**Eingereicht am 19.1.2017**

**Verteidigt am 07.08.2017**

Eingereicht am 19.1.2017

Verteidigt am 07.08.2017

1. Gutachter: Prof. Dr. Jan Michael Rost
2. Gutachter: Prof. Dr. Walter Strunz

*To my family and teachers*



# Abstract

The work presented in this dissertation concerns dynamics of Rydberg atom lattices in the presence of noise and dissipation. Rydberg atoms possess a number of exaggerated properties, such as a strong van der Waals interaction. The interplay of that interaction, coherent driving and decoherence leads to intriguing non-equilibrium phenomena.

Here, we study the non-equilibrium physics of driven atom lattices in the presence of decoherence caused by either laser phase noise or strong decay. In the first case, we compare between global and local noise and explore their effect on the number of excitations and the full counting statistics. We find that both types of noise give rise to a characteristic distribution of the Rydberg excitation number. The main method employed is the Langevin equation but for the sake of efficiency in certain regimes, we use a Markovian master equation and Monte Carlo rate equations, respectively.

In the second case, we consider dissipative systems with more general power-law interactions. We determine the phase diagram in the steady state and analyse its generation dynamics using Monte Carlo rate equations. In contrast to nearest-neighbour models, there is no transition to long-range-ordered phases for realistic interactions and resonant driving. Yet, for finite laser detunings, we show that Rydberg atom lattices can undergo a dissipative phase transition to a long-range-ordered antiferromagnetic phase. We identify the advantages of Monte Carlo rate equations over mean field predictions.

Having studied the dynamics of Rydberg atom lattices, we study an application of the strong interactions in such systems for quantum information processing. We investigate the coherent exchange of a single photon between a superconducting microwave cavity and a lattice of strongly interacting Rydberg atoms in the presence of local electric field fluctuations plaguing the cavity surface. We show that despite the increased sensitivity of Rydberg states to electric fields, as compared to ground state atoms, the Rydberg dipole-dipole interaction can be used to protect the system against the dephasing induced by the local noise. Using  $1/f$  and laser phase noise models, we show that compared to the case with non-interacting atoms, our system exhibits longer coherence lifetimes and larger retrieval efficiency of the photon after storing into the atoms.



# Contents

<b>1</b>	<b>Introduction</b>	<b>1</b>
1.1	Outline . . . . .	2
<b>2</b>	<b>Rydberg atoms</b>	<b>5</b>
2.1	Basic properties . . . . .	6
2.1.1	The hydrogen atom . . . . .	6
2.1.2	Alkali atoms . . . . .	8
2.1.3	Dipole moments . . . . .	9
2.1.4	Lifetimes . . . . .	11
2.2	Rydberg-Rydberg interactions . . . . .	12
<b>3</b>	<b>Rydberg ensembles in the presence of noise</b>	<b>17</b>
3.1	Basic Setup . . . . .	18
3.2	1D lattice of two-level atoms . . . . .	18
3.2.1	Light-atom coupling . . . . .	19
3.2.2	Langevin equation . . . . .	21
3.2.3	Master equation . . . . .	22
3.2.4	Classical rate equation . . . . .	24
3.3	Two interacting atoms . . . . .	25
3.4	Few-body simulations . . . . .	26
3.5	Atom counting statistics . . . . .	28
3.6	Implications for experiments . . . . .	31
<b>4</b>	<b>Rydberg ensembles in the presence of dissipation</b>	<b>33</b>
4.1	Basic Setup . . . . .	35
4.2	Rydberg lattices with two-level atoms . . . . .	35
4.3	Rydberg lattices with three-level atoms . . . . .	38
4.4	Emergence of long-range order . . . . .	43
4.5	Implications for experiments . . . . .	45
<b>5</b>	<b>Interfacing Rydberg atoms and solid-state qubits</b>	<b>47</b>
5.1	The Jaynes-Cummings Model . . . . .	49

5.2	1/f noise . . . . .	51
5.3	Noise effects on single-atom dynamics . . . . .	52
<b>6</b>	<b>Noise-resistant quantum interface</b>	<b>57</b>
6.1	Noise effects on non-interacting ensembles . . . . .	58
6.1.1	The Tavis-Cummings Model . . . . .	59
6.1.2	The Langevin equation . . . . .	61
6.2	Effects of dipole-dipole interactions . . . . .	62
6.3	Effects of dissipative processes . . . . .	67
6.4	Transfer fidelities . . . . .	69
6.5	Robustness against 1/ $f$ noise . . . . .	72
	<b>Conclusions and Outlook</b>	<b>77</b>
6.6	Future perspective . . . . .	78
	<b>Appendices</b>	<b>81</b>
	<b>Appendix</b>	<b>81</b>
	<b>Appendix A The multipole expansion of dipole-dipole interactions</b>	<b>83</b>
A.1	Multipole expansion of dipole-dipole interactions . . . . .	83
	<b>Appendix B Simulation Methods</b>	<b>85</b>
B.1	Quantum simulations of smaller lattice . . . . .	85
B.2	Dynamic and Steady-state Monte Carlo . . . . .	88
B.3	Mean field . . . . .	89
	<b>Appendix C The population inversion due to the presence of dark state</b>	<b>93</b>
	<b>Appendix D State truncation</b>	<b>95</b>
	<b>References</b>	<b>97</b>
	<b>Nomenclature</b>	<b>111</b>



# List of Figures

2.1	The radial charge and a comparison of effective potentials for hydrogen and alkaline atoms. . . . .	8
2.2	Radial wave function of Rubidium . . . . .	10
2.3	Scheme of two interacting atoms . . . . .	13
2.4	Scheme of two three-states atoms . . . . .	14
2.5	Comparison of eigenenergy $E_+$ (a, b) and state $E_-$ (c, d) as the function the interaction strength $V_0/\Delta$ (a, c) and $R/R_{vdw}$ . . . . .	15
3.1	Schematics of a one-dimensional lattice in the presence of noise . . . . .	18
3.2	Time variations of the random force $F(t)$ and phase $\phi(t)$ of the electric field of the laser wave. . . . .	22
3.3	The averaged fraction of Rydberg atoms as a function of time in the presence of noise for the case of Markovian and strong decoherence limit . . . . .	24
3.4	The steady state of excitation distribution in the presence of global and local noise for a two-atom scenario . . . . .	26
3.5	Relaxation of the fraction of Rydberg atoms for a few atoms system . . . . .	27
3.6	Variance as a function of time for a few atom system . . . . .	28
3.7	Dynamics of the excitation distribution in the presence of global and local noise for a few atom system . . . . .	30
3.8	Steady-state variance in the presence of global and uncorrelated noise . . . . .	31
4.1	Schematics of a two-dimensional lattice with a three-level ladder-type system in the presence of dissipative processes . . . . .	34
4.2	Fraction of Rydberg atoms in a two-dimensional lattice as a function of $p_0$ for a Monte Carlo wave function and a classical rate equation . . . . .	37
4.3	$q$ parameter as a function of excitation probability $p_0$ for the case 1D and 2D . . . . .	38
4.4	Ground and excited population of single-atom case for three level scheme . . . . .	39
4.5	Comparison between a rate equation and optical bloch equation . . . . .	41
4.6	(a) $q$ parameter as a function of $p_0$ for the case of 1D system and (b) 2D system. The $q$ parameter as a function of $\Delta$ for the case of 2D system is shown in panel (c) . . . . .	43
4.7	Order parameter $q$ as a function the power-law exponent . . . . .	44

4.8	Order parameter $q$ as a function laser detunings $\Delta$ . . . . .	44
4.9	Comparison of order parameters $q$ via a Monte carlo rate equation and mean field method . . . . .	45
5.1	Schematics of a Rydberg atom coupled to SC cavity . . . . .	48
5.2	Schematics of eigen states and energies for atom-cavity interactions. . . . .	50
5.3	Rabi oscillation of single photon between cavity and single atom. . . . .	50
5.4	$1/f$ power spectral density . . . . .	53
5.5	Atoms-cavity coupling as the function of atoms-cavity surface distance . . . . .	53
5.6	Rabi oscillation of single photon between cavity and single atom in the presence of $1/f$ noise. . . . .	54
6.1	Schematics of Rydberg atoms coupled to superconducting cavity . . . . .	58
6.2	Rabi oscillation of single photon between cavity and $N=16$ non-interacting atom. . . . .	60
6.3	Rabi oscillation of single photon between cavity and $N=100$ non-interacting atom. . . . .	62
6.4	Coupling strengths between SC cavity and the symmetric state of $10 \times 10$ interacting atoms subjected to fluctuating noise from the cavity surface . . . . .	65
6.5	Cavity population for the case of 1D and 2D lattices . . . . .	66
6.6	Collective coupling of atoms as the function of eigen energies for for (a) 1D lattice and (b) 2D lattice. The energy of symmetric state and $\Delta_E$ is shown in (c) and (d), respectively. The rest parameters are $N = 100$ and $V_0 = 25g$ . . . . .	66
6.7	Cavity population in the presence of decay for $\gamma_s = 0.1g$ and $N = 4$ . . . . .	67
6.8	The dynamics of cavity population and the shift of eigen energy of symmetric state . . . . .	68
6.9	Storing and retrieval of microwave photon between SC cavity and atoms . . . . .	70
6.10	Panel (a) and (c) shows the maximum retrieval $\eta_0$ and the storage lifetime $\tau_{stor}$ as the function of interaction strength in the absence (triangles) $\gamma_s = 0$ and the presence of spontaneous decay (crosses) $\gamma_s = 0.01g$ , $\gamma_p = 0.01g$ for a 2D case . (b) and (d) shows of $\eta_0$ and $\tau_{stor}$ as the function of atom number in the absence (stars) and the presence of interactions (1D-squares, 2D-triangles) for $V_0 = 25g$ . The rest of parameters are $\Gamma = 5g$ and $\gamma = 14g$ . . . . .	71
6.11	Cavity population as a function of time for realistic parameters . . . . .	73
6.12	Storage lifetime and efficiency offset as the function of lattice spacing and atom number . . . . .	75
B.1	Comparison of simulation results between monte carlo wave function and density matrix master equation . . . . .	88
D.1	The truncation of state during atom loss processes . . . . .	95

# List of Tables

- 2.1 The properties of Rydberg states . . . . . 6
- 2.2 The free parameters of Rubidium . . . . . 9



# Introduction

The work presented in this dissertation concerns the interface between atomic physics, quantum optics, and quantum information. The first aim is to theoretically study non-equilibrium phenomena of Rydberg atom lattices in the presence of noise and dissipative processes. The second aim is to propose a solution for a long-standing problem of coupling quantum states in atoms to solid state quantum devices.

Non-equilibrium phenomena are ubiquitous in nature and can be found in fluids [1], cells [2, 3], light harvesting complexes [4] and polymers [5]. They can be studied in controllable artificial systems, in which the presence of driving and decoherence leads to intriguing physics that differs from the equilibrium situation. This has motivated much theoretical [6–11] and experimental work [12–21], based on different experimental platforms ranging from ultracold atoms [13–16] to driven semiconductor heterostructures [17–21]. Among such platforms, Rydberg atoms constitute a powerful tool for creating controllable interaction potentials [22, 23]. Together with decoherence and coherent driving, this can lead to non-equilibrium relaxation [24–28], which was also observed experimentally [29–32], and, to non-equilibrium steady-state phase transitions [33–45] in the limit of strong dephasing.

Decoherence may arise from laser phase noise or from the spontaneous decay of excited atoms. In the first case, we compare between homogeneous or inhomogeneous phase noise: the first one acts globally on the excited states (also referred to as correlated noise), while the second one acts locally on the excited states (uncorrelated noise). Previous works assumed that the noise is uncorrelated [24–28, 46–50]. However, as the laser features modes, practically it acts globally on the excited states of atoms. The consequences for the steady states of Rydberg ensembles are yet to be understood.

Although the presence of strong radiative decay prevents the preparation of Rydberg states, the interplay of coherent laser excitation and strongly interacting Rydberg atoms in the presence of strong radiative decay can lead to the non-equilibrium steady-

state phase transitions [33–45]. Most previous works have predicted the emergence of steady states with antiferromagnetic order on the basis of mean field theory assuming nearest neighbour interactions [33]. Yet, large single-site fluctuations due to a simple two-level driving scheme restrict the emergence of such ordering to short length scales in all lattice dimensionalities [34]. The other driving scheme (e.g. in three-level systems) in a 1D setting fails to realise crystallisation [34–36]. Meanfield predictions are also in conflict with variational calculations [37, 38] and field-theoretical methods [39], which raises the validity of the results. This motivates theoretical study of the possibility of long-range order in dissipative Rydberg atom lattices.

On the other hand, decoherence is a long-standing problem of coupling quantum states in atoms to superconducting cavity [51–55]. The implementation of such a quantum interface offers a major breakthrough for quantum information science. It allows the development of a powerful hybrid architecture, where long-lived states of atoms store quantum information that can be processed rapidly using superconducting circuits. For such a hybrid system, a strong coherent coupling between them is required for an efficient and fast information exchange, which can be achieved by exploiting the large dipole moment of Rydberg states [56–59]. However, it makes Rydberg states more susceptible to fluctuating electric fields, which are present close to the metallic cavity surface. The fluctuations shift the energy states of the atoms leading to random inhomogeneous phases (if the noise acts locally) being accumulated in the dynamics of each atomic transition.

Most previous works investigated the Rydberg-atom-surface interactions in atom-chip traps [60–63]. Although the coherent driving of a Rydberg transition near the surface of atomic chips has been demonstrated [53, 61], the coherent evolution is limited by the described noise mechanisms. For instance, adatoms are shown to be the major cause of electrostatic fields in atom chip surfaces [60, 64]. Although, harmful effects from electrostatic fields due to adsorbates have been mitigated by carefully designing the cryogenic chamber and cooling sequences [65], or by covering the surface of an atom-chip with a thin metallic layer [66], the problem of uncontrolled fluctuating fields is more difficult to address [61]. Hence, the realisation of noise-resistant quantum interfaces between Rydberg atoms and superconducting cavities remains a major challenge.

## 1.1 Outline

In chapter 2, a short introduction into the theory of Rydberg atoms will be given. In chapter 3, we study the dynamics of driven atom lattices in the presence of global noise and analyse its difference to the case of local noise. We will show that both types of noise give rise to a characteristic distribution of the Rydberg excitation number. The results of this work have been published in the article:

- Wildan Abdussalam and Laura I. R. Gil  
*Non-equilibrium Physics of Rydberg lattices in the presence of noise and dissipative processes,*

European Physical Journal for Special Topics **225**, Issue 15-16, 1325-1347, (2016).

In chapter 4, instead of the presence of noise, we study the dynamics of driven atom lattices in the presence of strong decay. We will show that a long-range-ordered antiferromagnetic phase can be realised in dissipative Rydberg atom lattices when subjected to appropriate coherent driving. In contrast to the equilibrium physics of the corresponding unitary systems, which is well described by mean field models [67] and nearest-neighbour approximations [68], fluctuations as well as the weak tail of the rapidly decaying interactions are both found to be essential for the physics of the dissipative phase transition. The results of this work have been published in the articles:

- M. Höning, W. Abdussalam, M. Fleischhauer and T. Pohl  
*Antiferromagnetic long-range order in dissipative Rydberg lattices*,  
Phys. Rev. A **90**, 021603 (R).  
and the extension in the article
- Wildan Abdussalam and Laura I. R. Gil  
*Non-equilibrium Physics of Rydberg lattices in the presence of noise and dissipative processes*,  
European Physical Journal for Special Topics **225**, Issue 15-16, 1325-1347, (2016).

In chapter 5, the coupling quantum states in atoms to superconducting circuits will be introduced. In chapter 6, we propose a noise-resistant interface between a collection of Rydberg atoms and a single photon in a superconducting cavity by means of (resonant) dipole-dipole interactions. Instead very large atoms clouds ( $N \simeq 10^6$  atoms) [60], we use an atomic lattice with up to hundreds atoms. In such system, (resonant) dipole-dipole interactions are exploited to compensate dephasing of Rydberg states due to fluctuating electric field from the superconducting cavity surface. We will show that this scenario is not only robust to the fluctuating noise from the cavity surface but also robust to the dissipative processes. The results of this work are summarised in

- W. Abdussalam, D. Viscor, T. Lahaye, J. Fortagh, A. Browaeys, and T. Pohl  
*Noise-resistant coupling between Rydberg atoms and a superconducting cavity via dipole-dipole interaction*.  
In preparation. To be submitted to Physical Review Letters.

In the appendix of this thesis, the supplementary informations are added. They contain the derivation of dipole-dipole interactions (Appendix A.1) for chapter 2, the simulation methods (Appendix B) for chapter 4, 5, and 6, the population inversion (Appendix C) for chapter 4 and the states truncation (Appendix D) for chapter 6.





# Rydberg atoms

## Contents

---

<b>2.1 Basic properties . . . . .</b>	<b>6</b>
2.1.1 The hydrogen atom . . . . .	6
2.1.2 Alkali atoms . . . . .	8
2.1.3 Dipole moments . . . . .	9
2.1.4 Lifetimes . . . . .	11
<b>2.2 Rydberg-Rydberg interactions . . . . .</b>	<b>12</b>

---

Rydberg atoms are atoms in which an electron is excited to a state with a very high principal quantum number  $n$  with energies close to the ionization limit. They are gigantic; the electron’s orbital radius extends over several thousands of bohr radii. As a result, Rydberg atoms possess a number of exaggerated properties [69] (see table 2.1): (i) a large dipole polarisability, which scales as  $\sim n^7$ , making them very sensitive to electric fields; (ii) long radiative lifetimes, scaling as  $\sim n^3$  such that the  $n = 50$  state of Rubidium has a lifetime of  $\sim 141.31 \mu\text{s}$  [70]; (iii) a dipole-dipole interaction which scales as  $\sim n^4$ , and, consequently, (iv) a strong van der Waals interaction  $C_6/r^6$  with  $C_6$  scaling approximately as  $C_6 \sim n^{11}$ . Owing to these interesting properties, Rydberg atoms have been widely studied, for example, in astrophysics [71, 72], plasma physics [73–75] and quantum optics [76–80], quantum information [22, 23, 81, 82], and quantum simulations [15, 83–85]. Most relevant for the present thesis work, interacting Rydberg atoms confined in lattices can be used for quantum simulations of many body phases [86–88] and provide a well suited platform for studying non-equilibrium phenomena [8, 24, 32, 33].

In this chapter, we will review some basic properties of Rydberg atoms as a prerequisite for describing the resulting many-particle physics in subsequent chapters. In Sec. 2.1, we first describe how to determine Rydberg states of single-electron atoms and their energy spectrum. We will discuss the electronic structure, dipole moments and

Property	Expression	$n$ dependence
Binding energy	$E_n$	$n^{-2}$
Level spacing	$E_n - E_{n-1}$	$n^{-3}$
Orbital radius	$\langle nl r nl\rangle$	$n^2$
Dipole matrix element between low-lying state and Rydberg state	e.g. $\langle 5P r nS\rangle$	$n^{-3/2}$
Dipole matrix element between two Rydberg states	e.g. $\langle nP r nS\rangle$	$n^2$
Radiative lifetime	$\tau_{nlj}^0$	$n^3$

**Table 2.1:** Properties of Rydberg states

lifetime of alkaline atoms. In Sec. 2.2, we consider two atoms and their mutual dipole-dipole coupling that gives rise to van der Waals interactions.

## 2.1 Basic properties

In this Section, we briefly introduce selected basic single-atom properties of Rydberg states, which are most relevant for the considerations of the present thesis. We will focus on the simplest case of effective single-electron atoms, such as the alkalines, which are being employed in the majority of Rydberg gas experiments [22]. The electronic properties alkaline atoms are very similar to those of hydrogen atoms, and we will first consider this most simple case in the next section.

### 2.1.1 The hydrogen atom

The Hamiltonian for the hydrogen atom can be written as <sup>†</sup>

$$\hat{H}_a = -\frac{1}{2}\nabla^2 - \frac{1}{r} + \frac{\alpha^2}{r^3}\hat{\mathbf{L}} \cdot \hat{\mathbf{S}}, \quad (2.1)$$

where the first term describes the kinetic energy, and the second accounts for the Coulomb interaction between the electron and the singly charged nucleus. The third term is the spin-orbit coupling, where  $\alpha$  is the fine structure constant and  $\hat{\mathbf{L}}$  and  $\hat{\mathbf{S}}$  are the orbital and spin angular momentum operators of the electron. The eigenenergies and eigenstates can be obtained analytically by solving the time-independent Schrödinger equation

$$\hat{H}_a\psi_{nljm_j}(r, \theta, \phi) = E_{nlj}\psi_{nljm_j}(r, \theta, \phi). \quad (2.2)$$

<sup>†</sup> Here, we use Hartree atomic units, in which all length scales are in units of the Bohr radius  $a_0 = 5.29 \cdot 10^{-11}m$ , and energies are scaled by the Hartree energy  $E_H = m\alpha^2c^2 = 4.3579 \cdot 10^{-18}J$ , where  $m$  is the electron mass,  $\alpha$  the fine structure constant, and  $c$  the speed of light.

Since the Coulomb potential as well as the spin-orbit coupling are radially symmetric, the wave function  $\psi_{nljm_j}(r, \theta, \phi)$  can be factorised into two terms as

$$\psi_{nljm_j}(r, \theta, \phi) = \mathcal{R}_{nlj}(r) \mathcal{Y}_{l,j,m_j}(\theta, \phi). \quad (2.3)$$

The first part denotes the radial wavefunction  $\mathcal{R}_{nlj}(r)$  while  $\mathcal{Y}_{l,j,m_j}(\theta, \phi)$  is the angular eigenstate given by the generalised spherical harmonics as [89]

$$\mathcal{Y}_{l,j,m_j}(\theta, \phi) = \sqrt{\frac{j+m_j}{2j}} |y^+\rangle + \sqrt{\frac{j-m_j}{2j}} |y^-\rangle \quad (j = l + \frac{1}{2}) \quad (2.4)$$

$$\mathcal{Y}_{l,j,m_j}(\theta, \phi) = \sqrt{\frac{j+1+m_j}{2(j+1)}} |y^+\rangle + \sqrt{\frac{j+1-m_j}{2(j+1)}} |y^-\rangle \quad (j = l - \frac{1}{2}),$$

where

$$|y^\pm\rangle = Y_l^{m_j \mp \frac{1}{2}}(\theta, \phi) \left| \frac{1}{2}, \pm \frac{1}{2} \right\rangle, \quad (2.5)$$

and  $\left| \frac{1}{2}, \pm \frac{1}{2} \right\rangle$  denotes a definite spin state,  $|s, m_s\rangle$ . The quantum numbers  $n, l, j, m$  obey the following conditions:

- The principal quantum number assumes positive integer values  $n > 0$ .
- The orbital quantum number  $l$  acquires integer values between 0 and  $n - 1$ .
- The quantum numbers  $j$  and  $m_j$  derive from the total angular momentum operator  $\hat{\mathbf{J}} = \hat{\mathbf{L}} + \hat{\mathbf{S}}$ . The quantum  $j$  follows from the eigenvalue,  $j(j+1)$ , of the operator  $\hat{\mathbf{J}}^2$ , such that  $j = l + \frac{1}{2}$  or  $j = l - \frac{1}{2}$  for  $l > 0$ , and  $j = +\frac{1}{2}$  for  $l = 0$ .
- The quantum number  $m_j$  corresponds to the projection of the total angular momentum onto the  $z$ -axis, and, therefore, acquires integer values between  $-j$  and  $+j$ .

Below, we will use the standard notation for low- $l$  orbitals, with  $l = 0$  denoted by  $S$ -states,  $l = 1$  by  $P$ -states,  $l = 2$  by  $D$ -states, and  $l = 3$  by  $F$ -states. Moreover, when the quantum numbers  $j$  and  $m_j$  are irrelevant, we will use the label  $nS$ ,  $nP$ , etc., to indicate the  $|n, l = 0, \dots\rangle$ ,  $|n, l = 1, \dots\rangle$ , etc., states. When only  $m_j$  is irrelevant, we will append the value of  $j$  as a subscript, e.g. write  $nP_{3/2}$  for the  $|n, l = 1, j = 3/2, \dots\rangle$  state.

The resulting radial Schrödinger equation

$$E_{nlj} \mathcal{R}_{nlj} = \left\{ -\frac{1}{2} \left[ \frac{d^2}{dr^2} + \frac{2}{r} \frac{d}{dr} \right] + \frac{l(l+1)}{2r^2} - \frac{1}{r} + \alpha^2 \frac{j(j+1) - l(l+1) - \frac{3}{4}}{2r^3} \right\} \mathcal{R}_{nlj}(r), \quad (2.6)$$

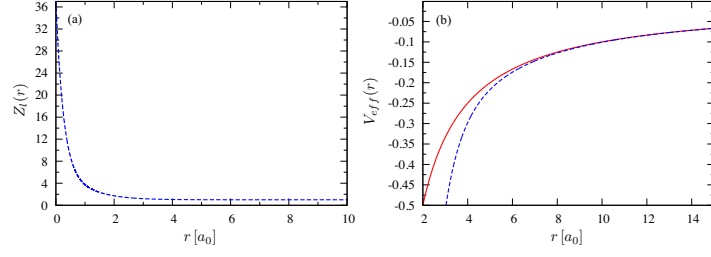


**Figure 2.1:** (a) Distance dependence of the radial charge of Rubidium and (b) the resulting effective core potential (blue dashed) line, as given by Eq. (2.9) compared to the pure Coulomb potential for the hydrogen atom (red line).

can be solved analytically, which yields the following eigenenergies and eigenstates

$$E_{nlj} = E_{nj} = -\frac{1}{2n^2} \left( 1 + \frac{\alpha^2}{n^2} \left[ \frac{n}{j + \frac{1}{2}} - \frac{3}{4} \right] \right), \quad (2.7)$$

$$\psi_{nlm_j}(r) = \sqrt{\left(\frac{2}{n}\right)^3 \frac{(n-l-1)!}{2n(n+l)!}} e^{\rho/2} \rho^l L_{n-l-1}^{2l+1}(\rho) \mathcal{Y}_{l,j,m_j}(\theta, \phi), \quad (2.8)$$

where  $\rho = 2r/n$  and  $L_{n-l-1}^{2l+1}$  is the generalised Laguerre polynomial.

### 2.1.2 Alkali atoms

Alkaline atoms represent the simplest non-hydrogenic systems. For a given nuclear charge  $z$ , they feature a single valence electron orbiting a compact core of the remaining  $z - 1$  electrons that occupy closed shells. Their interaction with weak external fields is thus dominated by the single active valence electron while the effects of the core electrons can be described by an effective core potential  $V_{eff}(r)$  replacing the Coulomb potential,  $-1/r$ , in Eq.(2.1). An accurate and, yet, simple form is described in [90] and given by

$$V_{eff}(r) = -\frac{Z_l(r)}{r} - \frac{\alpha_c}{2r^4} \left[ 1 - e^{-(r/r_c)^6} \right]. \quad (2.9)$$

Here,  $\alpha_c$  denotes the static dipole polarisability of the core and the effective radial charge  $Z_l$  reads

$$Z_l(r) = 1 + (z - 1) e^{-a_1 r} - r (a_3 + a_4 r) e^{-a_2 r}. \quad (2.10)$$

The explicit values of the five free parameters ( $a_1, a_2, a_3, a_4, r_c$ ) in Eqs. (2.10) and (2.9) have been determined for rubidium atoms in [90]. Fig. 2.1 shows the corresponding radial charge of rubidium and a comparison of the Coulomb potential of hydrogen and the effective core potential. For high principal quantum numbers with large orbital radii,  $\sim n^2$ , the effective potential deviates from the Coulomb potential only within a small fraction of the actual atomic radius such that the resulting correction to the atom's binding energy

l	j	$\delta_{l,j,0}$	$\delta_{l,j,2}$
0	1/2	3.1311804	0.1784
1	1/2	2.6548849	0.2900
1	3/2	2.6416737	0.2950
2	3/2	1.34809171	-0.60286
2	5/2	1.34646572	-0.596
3	5/2	0.0165192	-0.085
3	7/2	0.0165437	-0.086

**Table 2.2:** The free parameters of Rubidium

can be expressed by the quantum defect formula

$$E_{nl} = -\frac{Ry^*}{(n - \delta_{nlj})^2} \quad (2.11)$$

where  $Ry \sim 0.5\text{a.u.}$  is the Rydberg constant and  $\delta_{nlj}$  denotes quantum defect. It can be accurately calculated from the Rydberg-Ritz formula [91]:

$$\delta_{nlj} = \delta_0 + \frac{\delta_2}{(n - \delta_0)^2} + \frac{\delta_4}{(n - \delta_0)^4} + \frac{\delta_6}{(n - \delta_0)^6} + \dots \quad (2.12)$$

Accurate values for  $\delta_{nlj}$  and the parameters in Eq.(2.12) can be obtained from precise spectroscopic data, as reported in [92, 93] for rubidium atoms, and given in table 2.2. For high angular momenta  $l > 3$ , the centrifugal barrier prevents electrons from penetrating the core potential region rendering the corresponding quantum defects virtually negligible.

In Fig. 2.2 we show calculated radial probability densities  $|r\mathcal{R}_{nlj}|^2$  for different values of  $n$  and  $l$ , illustrating the strong increase of the orbital size,  $\propto n^2$  with growing principal quantum number  $n$  for  $l = 0$ . For the  $n$  but  $l = 20$  with  $j = l - 1/2$  the strong centrifugal barrier prevents the electron from penetrating the core region such that the resulting wave functions are identical to that of hydrogen. We furthermore show the radial density of circular Rydberg states [94] with  $l = n - 1$  for which the density features only a single maximum.

### 2.1.3 Dipole moments

The obtained wave function, e.g., allow us to determine transition dipole moments of high lying Rydberg states which are essential for a range of central properties. They determine the interaction of atoms with laser light or microwave radiation, the atomic response to electric fields, and the van der Waals or dipolar interaction between the Rydberg atoms. The dipole moment operator is defined as

$$\hat{\mu} = -e\hat{\mathbf{r}}, \quad (2.13)$$

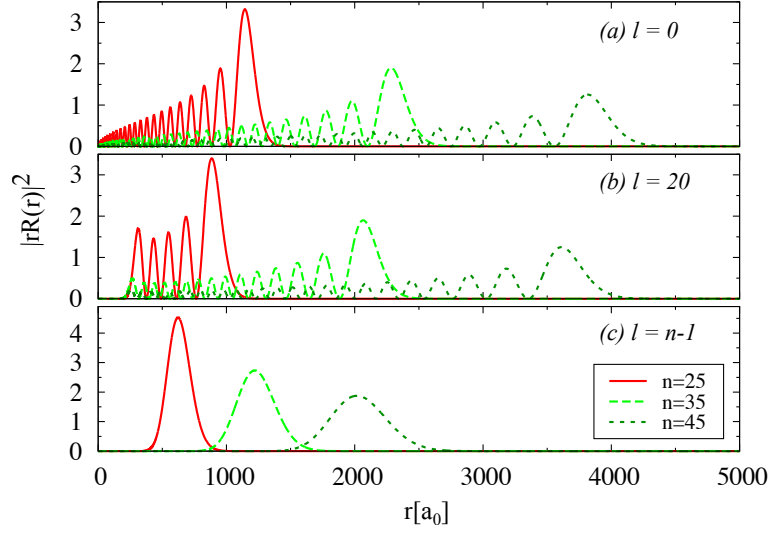


**Figure 2.2:** Radial probability densities  $|r\mathcal{R}_{nl}(r)|^2$  as a function of a distance from the core  $r [a_0]$  for  $n = 25, 35$ , and  $45$ . Panel (a) shows  $|r\mathcal{R}_{nl}(r)|^2$  for S states with  $l = 0$ , (b) a high value of  $l=20$ , showing the effects of the centrifugal barrier which pushes the valence electron away from the core, and (c)  $l = n - 1$  states, for which the wave function does not exhibit any nodes.

where  $\hat{\mathbf{r}}$  denotes the displacement vector of the valence electron from the nucleus, and  $e$  is the elementary charge, with  $e = 1$  in atomic units. Correspondingly the dipole matrix element for a transition between two states,  $|n, l, j, m_j\rangle$  and  $|n', l', j', m'_j\rangle$  is given by

$$\langle n, l, j, m_j | \hat{\mathbf{r}} | n', l', j', m'_j \rangle. \quad (2.14)$$

The aforementioned separability of the wave function carries over to the dipole matrix elements, which can be written as products,  $\mathcal{R}_{nlj}^{n'l'j'} \mathcal{C}_{ljm_j}^{l'j'm'_j}$ , of a radial matrix element

$$\mathcal{R}_{nlj}^{n'l'j'} = \int_0^\infty \mathcal{R}_{nlj}(r) r \mathcal{R}_{n'l'j'}(r) r^2 dr, \quad (2.15)$$

and matrix elements for the angular and spin component

$$\mathcal{C}_{ljm_j}^{l'j'm'_j} = \int d\phi d(\cos\theta) \overline{\mathcal{Y}_{l,j,m_j}(\theta, \phi)} \begin{pmatrix} \sin\theta \cos\phi \\ \sin\theta \sin\phi \\ \cos\theta \end{pmatrix} \mathcal{Y}_{l',j',m'_j}(\theta, \phi). \quad (2.16)$$

Using

$$\mathbf{e}_1 = \frac{\mathbf{e}_x + i\mathbf{e}_y}{\sqrt{2}}, \quad \mathbf{e}_2 = \frac{\mathbf{e}_x - i\mathbf{e}_y}{\sqrt{2}}, \quad \mathbf{e}_3 = \mathbf{e}_z \quad (2.17)$$

to define orthogonal polarization vectors from the cartesian basis vectors  $\mathbf{e}_x$ ,  $\mathbf{e}_y$  and  $\mathbf{e}_z$ , the matrix element can be most conveniently written as [95, 96]

$$\mathbf{e}_i \cdot \mathcal{C}_{l_j m_j}^{l' j' m'_j} = \sqrt{\frac{(2l+1)(2k+1)(2l'+1)}{4\pi}} \begin{pmatrix} j & k & j' \\ -m_j & \Delta m & m'_j \end{pmatrix} \begin{pmatrix} l & k & l' \\ 0 & 0 & 0 \end{pmatrix} \quad (2.18)$$

in terms of Wigner-3j symbol [95], where  $\Delta m = 0, \pm 1$  and  $k = 1$ .

### 2.1.4 Lifetimes

Applications of Rydberg atoms as quantum simulators or quantum computation platforms crucially rely on a long coherence of the excited state. The total lifetime  $\tau_{nlj}$  of a Rydberg state largely depends the spontaneous decay time  $\tau_{nlj}^0$  and the timescale  $\tau_{nlj}^{bb}$  for transition induced by black body radiation:

$$\frac{1}{\tau_{nlj}} = \frac{1}{\tau_{nlj}^0} + \frac{1}{\tau_{nlj}^{bb}}. \quad (2.19)$$

The rate of spontaneous decay from  $|nlj\rangle$  to  $|n'l'j'\rangle$  is given by the Einstein  $\mathcal{A}$  coefficient [69]

$$\mathcal{A}_{n'l'j',nlj} = \frac{e^2 \omega_{n'l'j',nlj}^3}{3\pi\epsilon_0 \hbar c^3} \frac{l_{max}}{2l+1} |\langle n'l'j' | \hat{\mathbf{r}} | nlj \rangle|^2, \quad (2.20)$$

where  $\omega_{n'l'j',nlj}$  denotes the frequency difference between the state  $|n'l'j'\rangle$  and the state  $|nlj\rangle$ ,  $\omega_{n'l'j',nlj} = (E_{n'l'j'} - E_{nlj})/\hbar$ , and  $l_{max}$  is the maximum of  $l$  and  $l'$ . The lifetime of a state  $|nlj\rangle$  is the reciprocal of the sum of decay rates to all possible final states  $|n'l'j'\rangle$ :

$$\tau_{nlj}^0 = \frac{1}{\sum_{n'l'j'} \mathcal{A}_{n'l'j',nlj}}. \quad (2.21)$$

Due to the strong dependence of the decay rate (2.20) on the frequency as  $\omega_{n'l'j',nlj}^3$ , transitions with the highest frequency difference generally contribute the largest terms in the sum (2.21). Thus, the predominant decay channel for a high-lying atomic state is a dipole-allowed transition to states with the lowest energy. For example, in rubidium  $|nS\rangle$  states decay predominantly to  $|5P\rangle$  and  $|6P\rangle$ , while  $|nP\rangle$  decays predominantly to  $|5S\rangle$ ,  $|6S\rangle$ , and  $|4D\rangle$  [97]. For high  $n$ , as  $n$  increases  $\omega_{n'l'j',nlj}$  converges due to the  $n^{-2}$ -scaling of the binding energy Eq. (2.11), and thus  $\mathcal{A}_{n'l'j',nlj}$  depends only on the matrix elements for the transition from the state  $|nlj\rangle$  to a low-lying state  $|n'l'j'\rangle$ . Thus for large  $n$ , we find the simple power-law scaling

$$\tau_{nlj}^0 \sim n^3, \quad (2.22)$$

showing that the lifetime rapidly increases with  $n$  which is essential for the applications mentioned above.

At a finite environmental temperature,  $T$ , black-body needs to be considered. Due to the small energy spacing between high-lying Rydberg states, and the large re-

spective matrix elements, black-body radiation can induce rather strong transitions with excited state manifolds. In equilibrium the frequency distribution of black body photons is given by [98]:

$$N(\omega) = \frac{1}{e^{\hbar\omega/k_bT} - 1}. \quad (2.23)$$

and features a linear temperature dependence if under the typical condition of  $\hbar\omega \ll k_bT$ . The resulting transition rates can be obtained from [69]:

$$K_{n'l'j',nlj} = \mathcal{A}_{n'l'j',nlj} N(\omega_{n'l'j',nlj}). \quad (2.24)$$

where  $\mathcal{A}_{n'l'j',nlj}$  is given in Eq.(2.20). At typical temperatures black-body radiation, hence, tends to cause transitions between energetically adjacent states with  $n' \sim n$ , in marked contrast to spontaneous emission, discussed above.

The total Rydberg state lifetime due to black-body radiation is obtained by summing the transition rates over all possible final states, which yields the approximate expression [69]

$$\tau_{nlj}^{bb} = \frac{3\hbar n^2}{4\alpha^3 k_b T}, \quad (2.25)$$

revealing a weaker  $n$ -dependence  $\tau_{nlj}^{bb} \sim n^2$ . As a result black body radiation can become the major lifetime limitation limiting factor as  $n$  increases. Accurate values for Rydberg lifetimes of alkaline atoms can be found in [70]. While black-body radiation is detrimental to many experiments, since it transfers atoms to Rydberg states that are not coupled by the initial excitation laser [99], it can be suppressed by working with cryogenic environments, as demonstrated experimentally in Ref. [56].

## 2.2 Rydberg-Rydberg interactions

Having discussed the most relevant single-atom properties of Rydberg states, we are now in a position to illuminate the interactions in atomic ensembles, which represent the most important aspect of the present thesis work. To this end, we consider two atoms separated by a distance vector  $\hat{\mathbf{R}}$ , whose interaction is composed of three contributions: the electrostatic repulsion between the core, the electrostatic attraction between one core and the Rydberg electron of the other atom, and the repulsion between the two Rydberg electrons. The Hamiltonian that represents these terms reads

$$\hat{H}_{dd} = \frac{e^2}{4\pi\epsilon_0} \cdot V_{dd}(\hat{\mathbf{R}}, \hat{\mathbf{r}}_{1A}, \hat{\mathbf{r}}_{2B}) \quad (2.26)$$

$$V_{dd}(\hat{\mathbf{R}}, \hat{\mathbf{r}}_{1A}, \hat{\mathbf{r}}_{2B}) = \left[ \frac{1}{|\hat{\mathbf{R}}|} - \frac{1}{|\hat{\mathbf{r}}_{1B}|} - \frac{1}{|\hat{\mathbf{r}}_{2A}|} + \frac{1}{|\hat{\mathbf{r}}_{12}|} \right] \quad (2.27)$$

$$= \left[ \frac{1}{|\hat{\mathbf{R}}|} - \frac{1}{|\hat{\mathbf{R}} - \hat{\mathbf{r}}_{1A}|} - \frac{1}{|\hat{\mathbf{R}} + \hat{\mathbf{r}}_{2B}|} + \frac{1}{|\hat{\mathbf{R}} - (\hat{\mathbf{r}}_{1A} - \hat{\mathbf{r}}_{2B})|} \right], \quad (2.28)$$



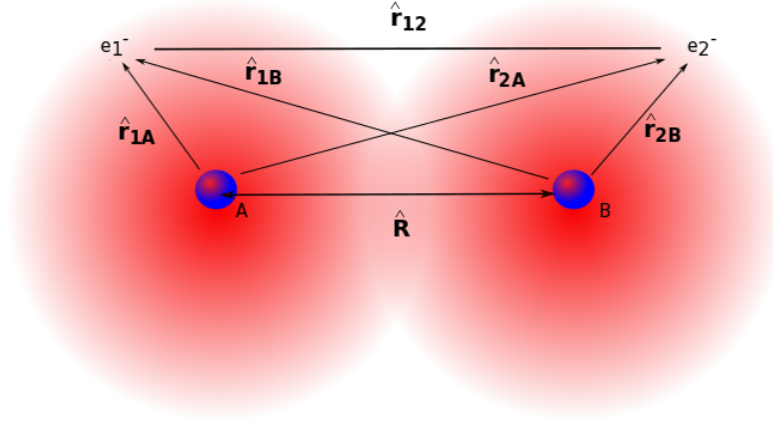


**Figure 2.3:** Illustration of two interacting Rydberg atoms in which A and B label the two atomic cores and 1 and 2 indicate the respective electrons.

where the distances  $\hat{\mathbf{R}}$ ,  $\hat{\mathbf{r}}_{2A}$ ,  $\hat{\mathbf{r}}_{1B}$ ,  $\hat{\mathbf{r}}_{1A}$ ,  $\hat{\mathbf{r}}_{2B}$  and  $\hat{\mathbf{r}}_{12}$  are shown in Fig. 2.3. Here,  $\hat{\mathbf{r}}_i = \{\hat{\mathbf{r}}_{1A}, \hat{\mathbf{r}}_{2B}\}$  and the characters A and B label the two cores and the numbers 1 and 2 indicate the respective Rydberg electrons. For large distances exceeding the typical size of the Rydberg orbits we can simplify Eq. (2.26) by means of a multipole expansion, which, to leading order, yields the dipole-dipole interaction Hamiltonian

$$\hat{H}_{dd} = \frac{\hat{\mu}_{1A} \cdot \hat{\mu}_{2B} - 3(\hat{\mu}_{1A} \cdot \mathbf{n})(\hat{\mu}_{2B} \cdot \mathbf{n})}{4\pi\epsilon_0 R^3}, \quad (2.29)$$

where the dipole moment operator is defined as  $\hat{\mu} = -e\hat{\mathbf{r}}_i$  and  $\mathbf{n} = \hat{\mathbf{R}}/R$ . A detailed derivation of Eq. (2.26) to (2.29) is given in Appendix A.1.

With the single-atom Hamiltonian  $\hat{h}_i$  and Eq. (2.29) the interaction potentials can be obtained by diagonalising the total two-atom Hamiltonian

$$\hat{H} = \hat{h}_1 + \hat{h}_2 + \hat{H}_{dd}. \quad (2.30)$$

While this typically requires a formidable numerical effort involving several  $10^4$  coupled pair states, we can obtain simple insights into the general scaling laws of the resulting interactions from the following simple model.

To this end, we consider only three relevant states  $|o_i\rangle, o = \{-, 0, +\}$  of an

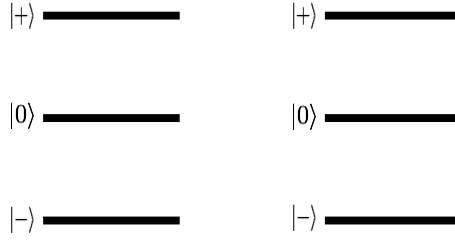


**Figure 2.4:** An example of two three-state atoms.

atom  $i$  (see Fig. 2.4) with

$$\langle +_i | \hat{\mathbf{r}}_i | -_i \rangle = \langle -_i | \hat{\mathbf{r}}_i | +_i \rangle = 0, \quad (2.31)$$

$$\langle 0_i | \hat{\mathbf{r}}_i | +_i \rangle = \langle +_i | \hat{\mathbf{r}}_i | 0_i \rangle = \mu_+ \neq 0, \quad (2.32)$$

$$\langle 0_i | \hat{\mathbf{r}}_i | -_i \rangle = \langle -_i | \hat{\mathbf{r}}_i | 0_i \rangle = \mu_- \neq 0. \quad (2.33)$$

The single atom energies are assumed to be given by

$$\varepsilon_0 = \langle 0_i | \hat{h}_i | 0_i \rangle = 0, \quad (2.34)$$

$$\varepsilon_+ = \langle +_i | \hat{h}_i | +_i \rangle > 0 \quad (2.35)$$

$$\varepsilon_- = \langle -_i | \hat{h}_i | -_i \rangle < 0, \quad (2.36)$$

such that the atomic pair energies at asymptotic distances  $R \rightarrow \infty$  are given by

$$\varepsilon_{00} = \langle 00 | \hat{h}_1 + \hat{h}_2 | 00 \rangle = 0, \quad (2.37)$$

$$\varepsilon_{+-} = \varepsilon_{-+} = \langle +- | \hat{h}_1 + \hat{h}_2 | +- \rangle = \varepsilon_+ + \varepsilon_-, \quad (2.38)$$

$$\varepsilon_{++} = \langle ++ | \hat{h}_1 + \hat{h}_2 | ++ \rangle = 2\varepsilon_+ \quad (2.39)$$

$$\varepsilon_{--} = \langle -- | \hat{h}_1 + \hat{h}_2 | -- \rangle = 2\varepsilon_-. \quad (2.40)$$

Since  $\varepsilon_+ > 0$  and  $\varepsilon_- < 0$ , we can assume that  $|\varepsilon_{++}|, |\varepsilon_{--}| \gg |\varepsilon_{+-}|$ . In addition, the states  $|++\rangle$  and  $|--\rangle$  are energetically far away and thus only give negligible contributions. Consequently, we only take into account the states  $|+-\rangle$  and  $|-+\rangle$ . The problem further simplifies in the rotated pair state basis

$$|m\rangle = \frac{|+-\rangle - |-+\rangle}{\sqrt{2}}, \quad (2.41)$$

$$|p\rangle = \frac{|+-\rangle + |-+\rangle}{\sqrt{2}}. \quad (2.42)$$

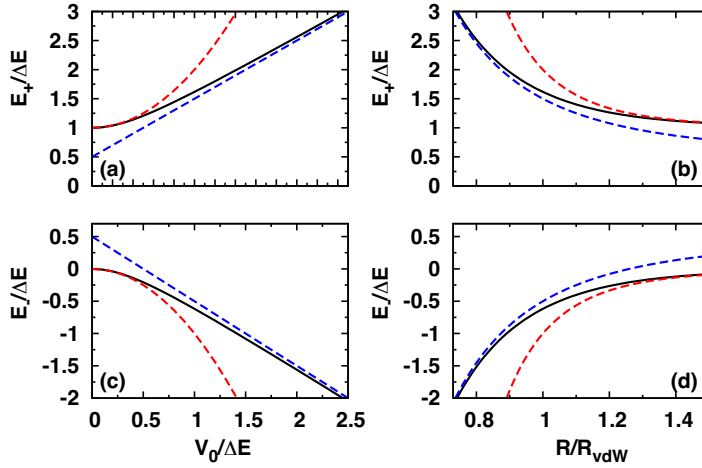


**Figure 2.5:** Comparison of eigenenergy associated with state  $|+\rangle$  (a, b) and state  $|-\rangle$  (c, d) as the function the interaction strength  $V_0/\Delta$  (a, c) and  $R/R_{vdw}$ . The exact solutions (black lines) from Eq. (2.46) are plotted together with the solutions for  $\Delta E \gg V_0$  (red dashed) from Eq. (2.47) and  $\Delta E \ll V_0$  (blue dashed) from Eq. (2.50).

for which

$$\langle 00 | \hat{H}_{dd} | m \rangle = 0, \quad (2.43)$$

$$\langle 00 | \hat{H}_{dd} | p \rangle = \frac{\sqrt{2}\mu_+\mu_-}{R^3} \quad (2.44)$$

and one obtains the following simple two-state Hamiltonian

$$\hat{H}_{2 \times 2} = \begin{pmatrix} 0 & V_0 \\ V_0 & \varepsilon_{+-} \end{pmatrix} \quad (2.45)$$

with  $V_0 = \sqrt{2}\mu_+\mu_-/R^3$ . Its eigenvalues

$$E_{\pm} = \frac{1}{2} \left( \varepsilon_{+-} \pm \sqrt{\varepsilon_{+-}^2 + 4V_0^2} \right). \quad (2.46)$$

allow to discriminate two distinct regimes. First, for weak dipole-dipole interaction,  $V_0 \ll \varepsilon_{+-}$  the pair energies

$$E_{\pm}/\varepsilon_{+-} \approx \frac{1}{2} \pm \frac{1}{2} \pm (V_0/\varepsilon_{+-})^2 \mp \mathcal{O}((V_0/\varepsilon_{+-})^4); \quad (2.47)$$

assume the characteristic form,  $C_6/R^6$ , of the van der Waals (vdW) interaction potential with the vdW-coefficient

$$C_6 = \frac{2\mu_+^2\mu_-^2}{\varepsilon_{+-}}. \quad (2.48)$$

Since  $\mu \sim n^2$  and  $\varepsilon_{+-} \sim n^{-3}$ , the  $C_6$  coefficient is found to scale as  $n^{11}$ . It follows from

the above discussion that the van der Waals potential is valid if  $R$  larger than the critical radius

$$R_{vdW} = \left( \frac{2\mu_+\mu_-}{\varepsilon_{+-}} \right)^{1/3}. \quad (2.49)$$

This is illustrated in Fig. 2.5. In the opposite limit where  $V_0 \gg \varepsilon_{+-}$ , the energies are approximately given by

$$E_{\pm}/\varepsilon_{+-} \approx \frac{1}{2} \pm V_0/\varepsilon_{+-} + \mathcal{O}(\varepsilon_{+-}/V_0), \quad (2.50)$$

corresponding to dipole-dipole interactions [96] with the coefficient

$$C_3 \sim \mu_+\mu_-. \quad (2.51)$$

scaling as  $n^4$ . This regime is valid for small distance  $R \ll R_{vdw}$ , as illustrated in Fig. 2.5. More detailed calculations of the  $C_6$  dispersion coefficients for alkali Rydberg atoms pairs are given in Ref. [100] and a numerical calculations for Rubidium beyond the simple power-law scaling with the distance  $R$  can be found in Ref [101, 102].

# Rydberg ensembles in the presence of noise

## Contents

---

<b>3.1 Basic Setup</b>	<b>18</b>
<b>3.2 1D lattice of two-level atoms</b>	<b>18</b>
3.2.1 Light-atom coupling	19
3.2.2 Langevin equation	21
3.2.3 Master equation	22
3.2.4 Classical rate equation	24
<b>3.3 Two interacting atoms</b>	<b>25</b>
<b>3.4 Few-body simulations</b>	<b>26</b>
<b>3.5 Atom counting statistics</b>	<b>28</b>
<b>3.6 Implications for experiments</b>	<b>31</b>

---

In the previous chapter, we have described basic properties of single and two-interacting atoms. In this chapter, we consider laser-driven lattice of Rydberg atoms and study the non-equilibrium physics in the presence of decoherence due to laser phase noise. We compare between homogeneous or inhomogeneous phase noise: the first one acts globally on the excited states (also referred to as correlated noise), while the second one acts locally on the excited states (uncorrelated noise). Most of previous work assumes that the noise is uncorrelated [24–28, 46–50]. However, as the laser features modes, practically it acts globally on the excited states of atoms. The consequences for the steady states of Rydberg ensemble are yet to be understood.

The chapter is organised as follows. In Sec. 3.1, we consider the setup, where the Hamiltonian that governs the system is provided in Sec. 3.2. For the simple case of two

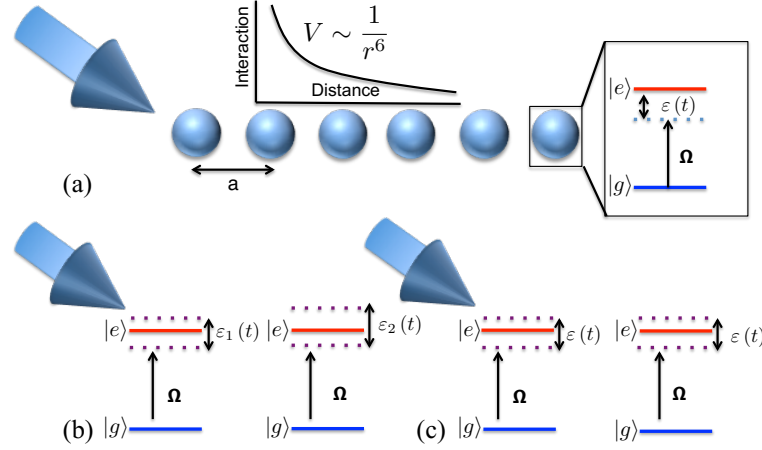


**Figure 3.1:** (a) Schematics of a one-dimensional lattice in which ground-state atoms  $|g\rangle$  are laser excited to the Rydberg state  $|e\rangle$  in the presence of local (b) or global (c) noise.

interacting atoms, we compare the steady states for global and local noise [see 3.3]. In Sec. 3.4 we extend the system to more atoms and characterise the Rydberg population and the full counting statistics (FCS) in Sec. 3.5. We will complete this chapter by considering implications for experiments in Sec. 3.6.

### 3.1 Basic Setup

We consider an ensemble of  $N$  two-level atoms, each with a ground state  $|g\rangle$  and a highly excited state  $|e\rangle$ , which are placed in neighbouring sites of a one-dimensional lattice with spacing  $a$  [see Fig.3.1(a)]. A pair of excited atoms at sites  $i$  and  $j$  experiences the repulsive van der Waals (vdW) interaction  $V_0/|i-j|^6$  with  $V_0 = C_6/a^6$  and  $C_6 > 0$ . The transitions between two states are driven by a laser, which is subject to local [see Fig.3.1(b)] and global [see Fig.3.1(c)] phase noise. We denote the Rabi frequency of laser by  $\Omega$  and detuning by  $\Delta = \omega_L - \omega_{eg}$ , where  $\omega_{eg} = (E_e - E_g)/\hbar$  denotes the atomic transition frequency and  $\omega_L$  denotes the laser frequency. We assume that the transitions are resonant in the sense that  $\Delta \simeq 0$ . As we will see, the interplay between the laser driving, vdW interaction and laser phase noise gives rise to a characteristic distribution of the Rydberg excitation number.

### 3.2 1D lattice of two-level atoms

In this section, we will consider the Hamiltonian that governs the system. As we are interested in exploiting the dynamics and steady state of the system, we will employ three different numerical methods. The main method employed is the Langevin equation, but for the sake of efficiency in certain regimes, we use a Markovian master equation and Monte Carlo rate equation, respectively.

### 3.2.1 Light-atom coupling

We firstly consider an atom with the atomic eigenstates  $|g\rangle$  and  $|e\rangle$ , under the influence of the laser field

$$\mathcal{E}(\mathbf{r}, t) = \mathcal{E}_0 \cos(\omega_L t + \phi(t) - \mathbf{k} \cdot \mathbf{r}) = \frac{1}{2} \mathcal{E}_0 \left( e^{i(\omega_L t + \phi(t) - \mathbf{k} \cdot \mathbf{r})} + e^{-i(\omega_L t + \phi(t) - \mathbf{k} \cdot \mathbf{r})} \right). \quad (3.1)$$

The amplitude of the field is denoted by  $\mathcal{E}_0$ , where  $\omega_L$  and  $\phi$  denotes the field frequency and the phase noise, respectively. The Hamiltonian that governs the system is given by

$$\hat{H}_{AL} = \hat{H}_{atom} + \hat{h}_{int} \quad (3.2)$$

$$= \hbar\omega_{eg} \hat{\sigma}_{ee} + q\hat{\mathbf{r}} \cdot \mathcal{E}(\hat{\mathbf{r}}, t) \quad (3.3)$$

$$= \hbar\omega_{eg} \hat{\sigma}_{ee} + \frac{1}{2} q\hat{\mathbf{r}} \cdot \mathcal{E}_0 \left( e^{i(\omega_L t + \phi(t) - \mathbf{k} \cdot \mathbf{r})} + e^{-i(\omega_L t + \phi(t) - \mathbf{k} \cdot \mathbf{r})} \right) \quad (3.4)$$

where  $q = -e$  denotes the electron charge and  $q\hat{\mathbf{r}} \exp(\pm i\mathbf{k} \cdot \hat{\mathbf{r}})$  can be expressed in the two-state basis  $\{|g\rangle, |e\rangle\}$ :

$$\begin{aligned} q\hat{\mathbf{r}} \exp(\pm i\mathbf{k} \cdot \hat{\mathbf{r}}) &= -\langle g|e\hat{\mathbf{r}} \exp(\pm i\mathbf{k} \cdot \hat{\mathbf{r}})|e\rangle|g\rangle\langle e| - \langle e|e\hat{\mathbf{r}} \exp(\pm i\mathbf{k} \cdot \hat{\mathbf{r}})|g\rangle|e\rangle\langle g| \\ &- \langle g|e\hat{\mathbf{r}} \exp(\pm i\mathbf{k} \cdot \hat{\mathbf{r}})|g\rangle|g\rangle\langle g| - \langle e|e\hat{\mathbf{r}} \exp(\pm i\mathbf{k} \cdot \hat{\mathbf{r}})|e\rangle|e\rangle\langle e|. \end{aligned} \quad (3.5)$$

The third and fourth part of Eq. (3.5) is zero  $\langle g|\hat{\mathbf{r}}|g\rangle = \langle e|\hat{\mathbf{r}}|e\rangle = 0$ . The first and second part can be simplified by performing a dipole approximation, i.e., an approach via neglecting the spatial dependence of the electric field. On the first glance, applying a dipole approximation is prohibited. This is due to the fact that the Rydberg state  $|e\rangle$  is on average a thousand Bohr radii far away from the core (see Chap. 2), which is the same order of magnitude of the laser wavelength  $2\pi/k$ . However, if the scalar products in (3.5) are written as integrals of the form

$$\int d^3r \overline{\psi_g(\mathbf{r})} e\mathbf{r} \exp(\pm i\mathbf{k} \cdot \mathbf{r}) \psi_e(\mathbf{r}), \quad (3.6)$$

the significant contributions only come from the positions where the products  $|\psi_g(\mathbf{r}) \psi_e(\mathbf{r})|$  is large. As the ground state  $|g\rangle$  has a size of only a few atomic units ( $1 \text{ nm} \ll 2\pi/k$ ), the product  $|\psi_g(\mathbf{r}) \psi_e(\mathbf{r})|$  has a size much smaller than the wavelength ( $\mathbf{k} \cdot \mathbf{r} \ll 1$ ). Therefore, we may apply the dipole approximation,

$$e\hat{\mathbf{r}} \exp(\pm i\mathbf{k} \cdot \mathbf{r}) \approx e\hat{\mathbf{r}} = \langle g|e\hat{\mathbf{r}}|e\rangle|g\rangle\langle e| + \langle e|e\hat{\mathbf{r}}|g\rangle|e\rangle\langle g| = \hat{\mu} (\hat{\sigma}_{ge} + \hat{\sigma}_{eg}), \quad (3.7)$$

where  $\hat{\mu} = e\langle g|\hat{\mathbf{r}}|e\rangle$  is the dipole matrix element. Here, we have also defined the operators  $\hat{\sigma}_{\alpha\beta} = |\alpha\rangle\langle\beta|$ . The Hamiltonian (3.2) becomes

$$\hat{H}_{AL} = \hbar\omega_{eg} \hat{\sigma}_{ee} + \frac{1}{2} \mathcal{E}_0 \cdot \hat{\mu} (\hat{\sigma}_{eg} + \hat{\sigma}_{ge}) \left( e^{i(\omega_L t + \phi(t))} + e^{-i(\omega_L t + \phi(t))} \right) \quad (3.8)$$

It is useful to transform the problem to the interacting picture by applying the unitary transformation

$$\hat{U} = e^{-i\hbar\omega_{ge}t\hat{\sigma}_{ee}}, \quad (3.9)$$

from which we obtain the Hamiltonian

$$\hat{H}_{AL}^I = \hat{U}^\dagger \hat{H}_{AL} \hat{U} - \hbar\omega_{eg}\hat{\sigma}_{ee} \quad (3.10)$$

$$= \frac{1}{2}\mathcal{E}_0 \cdot \hat{\mu} \left( \hat{\sigma}_{eg}e^{i\omega_{eg}t} + \hat{\sigma}_{ge}e^{-i\omega_{eg}t} \right) \left( e^{i(\omega_L t + \phi(t))} + e^{-i(\omega_L t + \phi(t))} \right) \quad (3.11)$$

$$= \frac{\hbar\Omega}{2} \left( \hat{\sigma}_{eg}e^{i[(\omega_{eg} + \omega_L)t + \phi(t)]} + \hat{\sigma}_{ge}e^{i(\Delta t + \phi(t))} + \hat{\sigma}_{eg}e^{-i(\Delta t + \phi(t))} + \hat{\sigma}_{ge}e^{-i[(\omega_{eg} + \omega_L)t + \phi(t)]} \right) \quad (3.12)$$

where  $\Delta = \omega_L - \omega_{eg}$  denotes the so-called detuning and  $\Omega = \mathcal{E}_0 \cdot \hat{\mu}/\hbar$  is the (resonant) Rabi frequency.

In order to eliminate the time dependence in (3.12), we perform another unitary transformation  $\hat{U} = e^{-i\hbar\Delta\hat{\sigma}_{ee}t}$ ,

$$\hat{H}_{AL}^I = \hat{U}^\dagger \hat{H}_{AL} \hat{U} - \hbar\Delta\hat{\sigma}_{ee} \quad (3.13)$$

$$= -\hbar\Delta\hat{\sigma}_{ee} + \frac{\hbar\Omega}{2} \left( \hat{\sigma}_{eg}e^{i[(\omega_{eg} + \omega_L)t + \phi(t)]} + \hat{\sigma}_{ge}e^{i\phi(t)} + \hat{\sigma}_{eg}e^{-i\phi(t)} + \hat{\sigma}_{ge}e^{-i[(\omega_{eg} + \omega_L)t + \phi(t)]} \right) \quad (3.14)$$

We use the Hilbert space basis ( $|e\rangle, |g\rangle$ ), i.e.,

$$|\psi\rangle = c_g|g\rangle + c_e|e\rangle \quad (3.15)$$

and numerically find the solution of the Schrödinger equation

$$i\hbar\partial_t|\psi(t)\rangle = \hat{H}_{AL}^I|\psi(t)\rangle \quad (3.16)$$

with the initial condition  $|\psi(0)\rangle = |g\rangle$ . For large values of  $\omega_L$ , the solution is a combination of slow oscillations (the so-called "Rabi oscillations") and small, fast oscillations. The latter vanish for  $\omega_L \rightarrow \infty$ . This is due to the quickly oscillating nature of the terms  $e^{\pm(\omega_{ge} + \omega_L + \Delta)t}$  in the Hamiltonian 3.14. Hence, if  $\omega_{ge} + \omega_L$  becomes large enough ( $\omega_{ge} + \omega_L \ll \Delta, \Omega$ ), they average out very short timescales  $\sim (\omega_L + \omega_{eg})^{-1} \ll \Delta^{-1}, \Omega^{-1}$  and it is justified to neglect them. This is known as the rotating wave approximation (RWA). This leaves us with

$$\hat{H}_{AL}^I = -\hbar\Delta\hat{\sigma}_{ee} + \frac{\hbar\Omega}{2} \left( \hat{\sigma}_{ge}e^{i\phi(t)} + \hat{\sigma}_{eg}e^{-i\phi(t)} \right). \quad (3.17)$$

At initial condition  $t = 0$ , the phase noise has the form  $e^{i\phi(0)}$ . The instantaneous change of phase noise can be defined as  $e^{i\phi(t-t')}$ . Thus, the Eq. (3.17) becomes

$$\hat{H}_{AL}^I = -\hbar\Delta\hat{\sigma}_{ee} + \frac{\hbar\Omega}{2} \left( \hat{\sigma}_{ge}e^{i(\phi(t) - \phi(t'))} + \hat{\sigma}_{eg}e^{-i(\phi(t) - \phi(t'))} \right). \quad (3.18)$$



The instantaneous change of phase is so-called the frequency noise

$$\varepsilon(t) = \dot{\phi} = \frac{d\phi}{dt}, \quad (3.19)$$

which corresponds to the energetic shifts of Rydberg state. Finally, we perform the transformation  $\hat{U} = e^{-i\hbar\varepsilon(t)\hat{\sigma}_{ee}}$  [103] to remove the time dependence of the frequency noise in the exponent,

$$\hat{H}_{AL}^I = -\hbar\Delta\hat{\sigma}_{ee} - \hbar\varepsilon(t)\hat{\sigma}_{ee} + \frac{\hbar\Omega}{2}(\hat{\sigma}_{ge} + \hat{\sigma}_{eg}), \quad (3.20)$$

which is the Hamiltonian that governs the interaction between a single atom and light. For  $N$ -interacting atoms, the total Hamiltonian reads

$$\hat{H} = \hat{H}_I - \hat{H}_n \quad (3.21)$$

$$\hat{H}_I = \frac{\Omega}{2} \sum_i (\hat{\sigma}_{eg}^{(i)} + \hat{\sigma}_{ge}^{(i)}) + V_0 \sum_{i<j} \frac{\hat{\sigma}_{ee}^{(i)} \hat{\sigma}_{ee}^{(j)}}{|i-j|^6} \quad (3.22)$$

$$\hat{H}_n = \sum_i \varepsilon^{(i)}(t) \hat{\sigma}_{ee}^{(i)} \quad (3.23)$$

where  $\hbar = 1$ ,  $V_0 = C_6/a^6$  and  $C_6 > 0$ , i.e., the repulsive van der Waals (vdW) interaction. As we consider a Rydberg ensemble in a one dimensional lattice, a pair of excited atoms at site  $i$  and  $j$  is separated by distance  $r_{ij} \equiv |i-j|$ . The transitions between two states are in resonance with the field frequency  $\Delta = \omega_{eg} - \omega_L \simeq 0$ . Hence, we neglect  $\Delta$  for the rest of the calculation in this chapter. The frequency noise  $\varepsilon(t)$  has the following relations:

$$\langle \varepsilon^{(i)} \varepsilon^{(j)} \rangle = C \delta_{ij} \quad (3.24)$$

$$\varepsilon^{(i)} = \varepsilon, \quad (3.25)$$

with (3.24) and (3.25) being local and global phase noise, respectively.

### 3.2.2 Langevin equation

The phase noise  $\phi(t)$  causes fast and slow fluctuation of the laser with correlation time  $\tau_c$ , where a characteristic time  $\tau_d \gg \tau_c$  [see Fig. 3.2(b)]. It acts as a time-dependent detuning and can be considered analogous to a one-dimensional Brownian motion in which the time evolution is quantitatively described by the Langevin equation [103, 104]

$$\ddot{\phi} = -\gamma\dot{\phi} + F(t) \quad (3.26)$$

where  $\gamma$  denotes the inverse of correlation time  $\tau_c = 1/\gamma$ , and  $F(t)$  is a Gaussian function which denotes a rapidly fluctuating force with zero ensemble average  $\overline{F(t)} = 0$  and  $\overline{F(t)^2} \neq 0$  [see Fig. 3.2(a)]. We assume that  $F(t)$  has an extremely short correlation time compared to all other characteristic time scales of the system [103, 104], and thus approx-

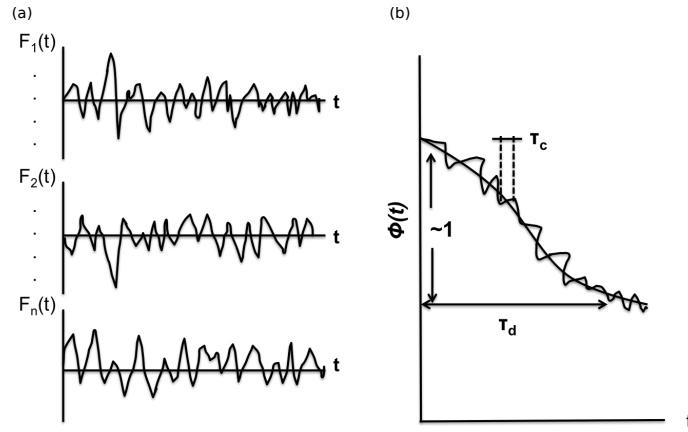


**Figure 3.2:** Panel (a) shows an example time dependence of random force  $F(t)$  for various realisations and (b) shows the phase  $\phi(t)$  of the electric field of the laser wave, exhibiting fast and slow fluctuations characterized by the correlation times  $\tau_c$  and  $\tau_d$ .

imate

$$\overline{F(t)F(t')} = 2D\delta(t - t'). \quad (3.27)$$

Here  $D$  describes the magnitude of the fluctuating forces and  $\delta(t - t')$  a Dirac delta, which is together with  $\gamma$  characterises the spectral width  $\Gamma$  of the Lorentzian line shape [103]

$$\Gamma = \frac{2D}{\gamma^2}. \quad (3.28)$$

We determine the quantum dynamics of this system by means of the Langevin equation in which a single realisation  $k$  of the time dependent wave function evolves as  $i|\dot{\psi}^{(k)}\rangle = \hat{H}|\psi^{(k)}\rangle$ . For  $M$  realisations  $|\psi^{(k)}\rangle$ , we calculate the excited state population  $\langle \hat{\sigma}_{ee}^{(k,i)} \rangle = \langle \psi^{(k)} | \hat{\sigma}_{ee}^{(i)} | \psi^{(k)} \rangle$  and take its average

$$N_{ee} = \frac{1}{M} \sum_{k=1}^M \sum_{i=1}^N \langle \hat{\sigma}_{ee}^{(k,i)} \rangle, \quad (3.29)$$

where  $N$  is the atom number. For sufficiently large  $M$ , the average converges.

### 3.2.3 Master equation

In order to test the Langevin equation, we now compare it to the result of a master equation for the  $n$ -body density matrix  $\hat{\rho}$ . The time evolution of the density matrix is given by

$$\dot{\hat{\rho}} = -i \left[ \hat{H}_I, \hat{\rho} \right] + \mathcal{L}[\hat{\rho}] \quad (3.30)$$

where  $\hat{H}_I$  is specified in Eq.(3.22). The superoperator  $\mathcal{L}$  accounts for the phase noise, which can be derived from a Born-Markov master equation [105]

$$\dot{\hat{\rho}} = - \int_{-\infty}^t dt' \text{tr}_B \left[ \hat{H}_n(t), \left[ \hat{H}_n(t'), \hat{\rho}(t) \right] \right], \quad (3.31)$$

with  $\hat{H}_n$  is given in (3.23) and  $\text{Tr}_B\{\cdot\}$  is equivalent to the average  $\langle \cdot \rangle$ . Inserting (3.23) into (3.31) we find

$$\begin{aligned} \dot{\hat{\rho}} &= - \int_{-\infty}^t dt' \sum_{i,j} \text{Tr}_B \left\{ \varepsilon^{(i)}(t) \varepsilon^{(j)}(t') \hat{\sigma}_{ee}^{(i)} \hat{\sigma}_{ee}^{(j)} \hat{\rho} + h.c. - \varepsilon^{(i)}(t) \hat{\sigma}_{ee}^{(i)} \hat{\rho} \varepsilon^{(j)}(t') \hat{\sigma}_{ee}^{(j)} + h.c. \right\} \\ &= - \sum_{i,j} \int_{-\infty}^t dt' \text{Tr}_B \left\{ \varepsilon^{(i)}(t) \varepsilon^{(j)}(t') \right\} \left[ \hat{\sigma}_{ee}^{(i)} \hat{\rho} \hat{\sigma}_{ee}^{(j)} - \frac{1}{2} \{ \hat{\sigma}_{ee}^{(i)} \hat{\sigma}_{ee}^{(j)}, \hat{\rho} \} \right] \\ &= \mathcal{L} [\hat{\rho}], \end{aligned} \quad (3.32)$$

where  $\text{Tr}_B \left\{ \varepsilon^{(i)}(t) \varepsilon^{(j)}(t') \right\} = \langle \varepsilon^{(i)}(t) \varepsilon^{(j)}(t') \rangle$ . For the local noise, similar to the relation Eq. (3.24), the correlation between the phase noise experience by atoms  $i$  and  $j$  at two different times is  $\langle \varepsilon^{(i)}(t) \varepsilon^{(j)}(t') \rangle = (\Gamma/2) \delta_{ij} \delta(t - t')$  and thus we find the superoperator for local phase noise

$$\mathcal{L} [\hat{\rho}]^{(l)} = \Gamma \sum_i \left[ \hat{\sigma}_{ee}^{(i)} \hat{\rho} \hat{\sigma}_{ee}^{(i)} - \frac{1}{2} \{ \hat{\sigma}_{ee}^{(i)} \hat{\sigma}_{ee}^{(i)}, \hat{\rho} \} \right], \quad (3.33)$$

and for global noise, similar to the relation Eq. (3.25), the correlation is  $\langle \varepsilon(t) \varepsilon(t') \rangle = (\Gamma/2) \delta(t - t')$  and the superoperator reads

$$\mathcal{L} [\hat{\rho}]^{(g)} = \Gamma \left[ \hat{\Sigma}_i \hat{\rho} \hat{\Sigma}_j - \frac{1}{2} \{ \hat{\Sigma}_i \hat{\Sigma}_j, \hat{\rho} \} \right] \quad (3.34)$$

where  $\hat{\Sigma}_i = \sum_e \hat{\sigma}_{ee}^{(i)}$ . The fraction of Rydberg atoms  $f_e$  is obtained by taking the trace  $\text{Tr} \{ \hat{\rho} \hat{\Sigma}_i \} / N$  which is equivalent to  $N_{ee} / N$  in Eq. (3.29).

We introduce the dimensionless rescaled time  $\tau = (4\Omega^2/\Gamma) \times t$ . The many-body state is determined by three independent dimensionless parameters: the spectral width of the noise  $\xi = \Gamma/\Omega$ , the damping term  $\bar{\gamma} = \gamma\Gamma/4\Omega^2$ , and the interaction strength parameter  $R^6 = C_6 / (\Gamma a^6)$ .

Fig. 3.3 (a) shows the relaxation of the fraction of Rydberg atoms in the presence of global noise. We show that in the limit  $\bar{\gamma} \gg \xi^2$ , i.e. for very short correlation time, the Langevin equation is in excellent agreement with Eq. (3.30). Later on in subsec. 3.4, we will discuss the dynamics in the strong coupling limit. There, the classical rate equation is computationally more efficient than the Langevin equation.

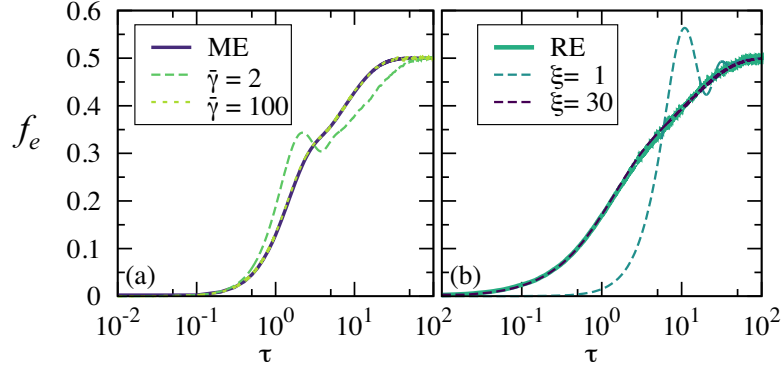


**Figure 3.3:** The averaged fraction of Rydberg atoms as a function of time (a) in the presence of global noise for  $N = 2$ ,  $\xi = 4$ ,  $R = 1$  and  $M = 10^4$  calculated by the Langevin equation (LE) for two different  $\bar{\gamma}$  is compared to the Markovian master equation (ME). (b) The averaged fraction of Rydberg atoms for  $N = 6$  and  $R = 1$  calculated by the classical rate equation (RE) with  $M = 10^4$  is compared to the Markovian master equation with two different  $\xi$  in the presence of local noise.

### 3.2.4 Classical rate equation

In order to derive a rate equation, let us consider the dimensionless rescaled time (3.30) with a Hamiltonian after rescaled time,

$$\hat{H}_I = \frac{\xi}{8} \sum_i \left( \hat{\sigma}_{ge}^{(i)} + \hat{\sigma}_{eg}^{(i)} \right) + \frac{\xi^2}{4} R^6 \sum_{i < j} \frac{\hat{\sigma}_{ee}^{(i)} \hat{\sigma}_{ee}^{(j)}}{|\mathbf{i} - \mathbf{j}|^6} \quad (3.35)$$

and superoperator for local

$$\mathcal{L}[\hat{\rho}]^{(l)} = \frac{\xi^2}{4} \sum_i \left[ \hat{\sigma}_{ee}^{(i)} \hat{\rho} \hat{\sigma}_{ee}^{(i)} - \frac{1}{2} \{ \hat{\sigma}_{ee}^{(i)} \hat{\sigma}_{ee}^{(i)}, \hat{\rho} \} \right]. \quad (3.36)$$

In the presence of local noise, the  $N$ -atom density matrix factorises,  $\hat{\rho} = \hat{\rho}_1^{(1)} \otimes \dots \otimes \hat{\rho}_N^{(1)}$ , conversely for global noise, the factorisation is precluded. Therefore, for local noise, the time evolution of non-interacting two-level atoms is completely determined by the master equation for the single-atom density matrix  $\hat{\rho}_k^1 \equiv \rho$ , i.e., the optical Bloch equation (OBE) for two level atom,

$$\begin{aligned} \dot{\rho}_{gg} &= i \frac{\xi}{8} [\rho_{ge} - \rho_{eg}] \\ \dot{\rho}_{ge} &= -\frac{\xi^2}{8} \rho_{eg} - i \frac{\xi}{8} (\rho_{gg} - \rho_{ee}) \\ \dot{\rho}_{eg} &= -\frac{\xi^2}{8} \rho_{ge} + i \frac{\xi}{8} (\rho_{gg} - \rho_{ee}) \\ \dot{\rho}_{ee} &= i \frac{\xi}{8} [\rho_{eg} - \rho_{ge}] \end{aligned} \quad (3.37)$$

The diagonal elements  $\rho_{\alpha\alpha}(\tau)$  of the density matrix indicate the probability of finding the atom at time  $\tau$  in the state  $|\alpha\rangle$ . The probability is conserved

$$\sum_{\alpha} \rho_{\alpha\alpha} = 1. \quad (3.38)$$

The off-diagonal elements, i.e., the coherences, contain the information about transition amplitudes between the levels. For sufficiently strong dephasing, the quantum dynamics can be reduced to the diagonal elements of  $\rho$  upon adiabatic elimination of its coherences by setting [106]

$$\dot{\rho}_{\alpha\beta} = 0 \quad \text{for} \quad \alpha \neq \beta. \quad (3.39)$$

We make use of relations (3.38) and (3.39) to simplify the time evolution to a classical rate equation model for the joint probabilities  $\rho_{S_1, \dots, S_N}$  of an atom  $i$  in the Rydberg state ( $S_i = 1$ ) or in the ground state ( $S_i = 0$ ). The time evolution is determined by

$$\begin{aligned} \dot{\rho}_{S_1, \dots, S_N} = & \sum_i \left[ (1 - S_i) D(\delta_i) + S_i P(\delta_i) \right] \rho_{S_1, \dots, 1-S_i, \dots, S_N} \\ & - \left[ (1 - S_i) P(\delta_i) + S_i D(\delta_i) \right] \rho_{S_1, \dots, S_i, \dots, S_N}, \end{aligned} \quad (3.40)$$

where  $P(\delta_i)$  and  $D(\delta_i)$  denote the excitation and de-excitation rates, respectively. The rates can be expressed as  $P(\delta_i) = 1/[4(1 + 4\delta_i^2)]$  and  $D(\delta_i) = 1/[4(1 + 4\delta_i^2)]$ . The interaction enters through an effective frequency detuning  $\delta_i = R^6 \sum_{j \neq i} S_j |\mathbf{r}_i - \mathbf{r}_j|^{-6}$  which accounts for the level shift of the  $i$ th atom due to its surrounding Rydberg excitations [24]. We solve the dynamics of Eq. (3.40) by means of dynamic Monte Carlo, where its algorithm is given in appendix B.2.

We use the Markovian master equation as a test for the classical rate equation. As shown on Fig.3.3(b), for  $\xi \gg 1$  the fraction of Rydberg atoms is indeed well reproduced by the Markovian master equation model (3.30). This is in agreement with the results of [106–108]. In the following, we will only consider short correlation times  $\bar{\gamma} \gg 1$  and strong dephasing  $\xi \gg 1$ .

### 3.3 Two interacting atoms

In this section, we investigate the difference between global and local noise for two atoms, with emphasis on the steady-state distribution in the non-interacting and interacting case.

For non-interacting atoms in the presence of global noise [see Fig. 3.4 (a) (red bar)], the distribution is uniform for any excitation number. This is due to the fact that the phase acquired by each atom is identical. Consequently, the coherent driving couples the ground state of atoms to the symmetric state  $|+\rangle = (1/\sqrt{2})(|ge\rangle + |eg\rangle)$  and the latter to the doubly excited state [see Fig. 3.4 (b) for  $V_{12} = 0$ ]. However, the antisymmetric state

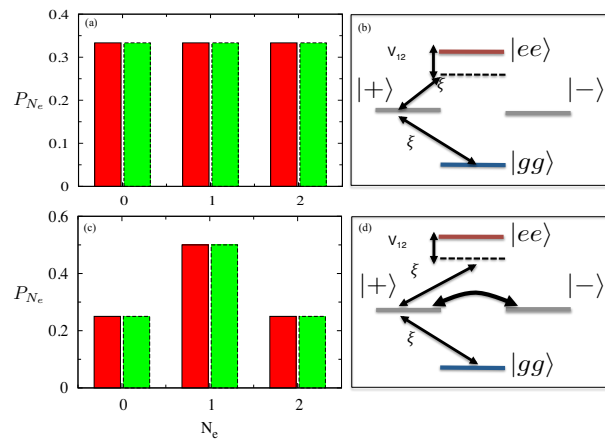


**Figure 3.4:** The excitation probability  $P_{N_e}$  in the steady state as a function of the number of excitations  $N_e$  in the presence of global (a) and local (c) noise. Red and green bars indicate non-interacting and interacting Rydberg atoms, respectively. (b) and (d) illustrate the couplings between the two-atom energy states in the presence of global and local noise.

$|-\rangle = (1/\sqrt{2})(|ge\rangle - |eg\rangle)$  is decoupled. Thus, the excitation probability  $P_{N_e}$  for any excitation number  $N_e$  is  $P_{N_e} = 1/3$ .

On the contrary, the steady-state distribution in the presence of local noise exhibits a non-uniform distribution [see Fig. 3.4 (c) (red bar)]. This is due to the fact that each atom acquires a different phase  $\varepsilon^{(i)}(t)$ . Consequently, the symmetric state  $|+\rangle$  couples to the antisymmetric state  $|-\rangle$  [see Fig. 3.4 (d) for  $V_{12} = 0$ ] which leads to a different population distribution with  $P_0 = 1/4$ ,  $P_1 = 1/2$ , and  $P_2 = 1/4$ .

In the presence of interactions  $V_{12} > 0$ , the steady-state distribution is the same as in the non-interacting case [see Fig. 3.4 (a) and (c) green bar]. Despite the presence of Rydberg-Rydberg interactions, the steady state for both types of noise remains unchanged, as the interaction only shifts the energy of the doubly-excited state. In the presence of global noise, the energetic shift of the doubly-excited state is unable to break the symmetry, resulting in the same distribution as in the non-interacting case. For the minimal example of two interacting atoms, we have shown that the steady-state distribution changes remarkably with the type of noise considered, yet it remains unchanged qualitatively by the presence of interaction. In the next section we investigate whether this finding persists in larger ensemble.

### 3.4 Few-body simulations

We determine the fraction of Rydberg atoms  $f_e(\tau)$  in the presence of global and local noise for different interaction strength. We classify the interaction strength  $R^6$  into weak interactions for ( $R^6 \ll \xi$ ), intermediate interactions for ( $R^6 \sim \xi$ ) and strong interactions for ( $R^6 \gg \xi$ ). Increasing the interaction strength between the atoms slows down the

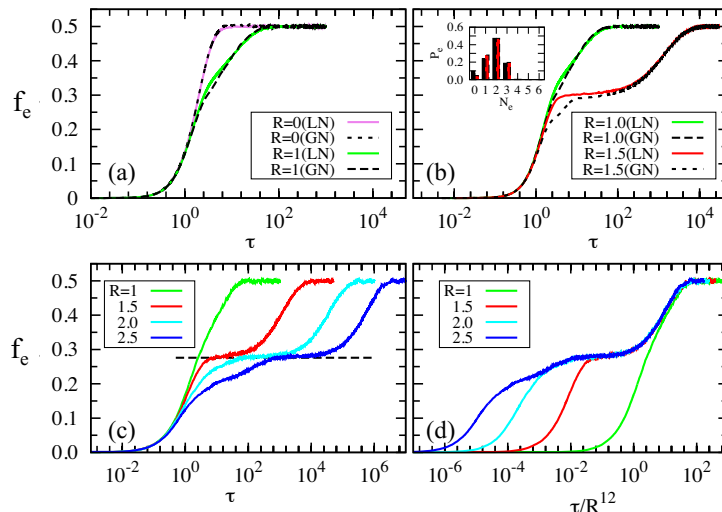


**Figure 3.5:** Relaxation of the fraction of Rydberg atoms in a one-dimensional system for  $N = 6$  and  $M = 10^4$  calculated by the Langevin equation [(a), (b)] and the rate equation [(c), (d)]. The comparison between global (GN) and local (LN) noise with  $\xi = 4$  and  $\bar{\gamma} = 100$  for non-interacting and interacting atoms is shown in (a) and for intermediate as well as strong interactions in (b). The inset in (b) shows the excitation distribution at the plateau for  $R = 1.5$ . Relaxation in the presence of local noise for different strong interactions is presented in (c), where the dashed line indicates the fraction of hard dimers. For long times the steady state is approached exponentially at a rate  $\propto R^{-12}$  (d).

relaxation time. Therefore, we will use three different methods for the three different limits : the Markovian master equation for the weak and intermediate interactions in the Markovian limit ( $\bar{\gamma} \gg \xi^2$ ), the Langevin equation for intermediate and strong interactions and arbitrary values of  $\bar{\gamma}$  and  $\xi$ , and the classical rate equation for strong interactions and dephasing ( $\xi \gg 1$ ) in the Markovian limit.

Fig. 3.5 shows the relaxation of the fraction of Rydberg atoms for  $N = 6$  for intermediate and strong interactions. The initial condition is  $f_e(0) = 0$  which corresponds to all atoms in the ground state. We vary the interaction strength and observe the characteristic of dynamics. We will see the slow down of relaxation accompanied the emergence of plateau before relaxing towards steady state. In the non-interacting case [see Fig. 3.5 (a)], the fraction of Rydberg atoms shows identical relaxation behaviour for both types of noise that reaches the steady state, with  $f_e(\infty) \simeq 0.5$ . As  $R^6$  is increased to intermediate interaction strength, the relaxation slows down because an excited atom suppresses the excitation of atoms at neighbouring sites.

We now consider an interaction strength of  $R^6 > \xi$ . Fig. 3.5 (b) shows that although the interaction strength is three times larger than the spectral width of the laser, the fraction of Rydberg atoms relaxation is nearly identical for both types of noise. A small discrepancy appears between global and local noise for intermediate interaction before entering the plateau which we will discuss in the next section. In the time window at which a plateau is present the excitation distribution for both types of noise is dominated by two excited atoms [see Fig. 3.5(b) inset]. As we increase the interaction strength [see

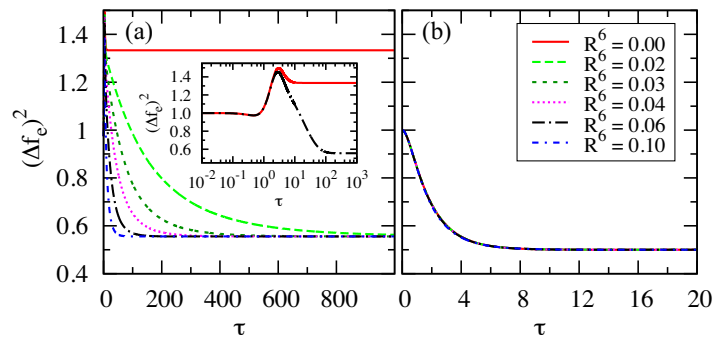


**Figure 3.6:** Variance  $(\Delta f_e)^2$  as a function of time for  $N = 6$ ,  $\xi = 5$  and various  $R^6$  in the presence of global noise (a) and local noise (b) calculated by the ME. Inset shows the relaxation in logarithmic x-axis scale for  $R^6 = 0$  and  $R^6 = 0.06$ .

Fig. 3.5 (c) and (d)], the plateau value becomes apparent.

Although the dynamics of the fraction of Rydberg atoms for both types of noise is nearly identical, the relaxation to the transient state shows a small discrepancy due to different excitation distributions. Therefore, in the next section, we will investigate the atom counting statistics for both types of noise.

### 3.5 Atom counting statistics

We now discuss the atom counting statistics for a small number of atoms with  $N \geq 6$ . One can quantify the distribution in terms of the **variance**  $(\Delta f_e)^2$  which corresponds to the fluctuations of a statistical distribution about its mean value. The variance is equal to the square of the standard deviation  $\Delta f_e$  and is defined by:

$$(\Delta f_e)^2 = \sum_i^N \frac{\langle \sigma_{ee}^{(i)2} \rangle - \langle \sigma_{ee}^{(i)} \rangle^2}{\langle \sigma_{ee}^{(i)} \rangle}. \quad (3.41)$$

Depending on the relation between the variance and the mean value one can distinguish three cases. In a sub-Poissonian distribution, the variance is less than the mean value  $(\Delta f_e)^2 < f_e$ . In a Poissonian distribution,  $(\Delta f_e)^2 = f_e$ . In a super-Poissonian distribution,  $(\Delta f_e)^2 > f_e$  [109].

In order to reach the steady state within a short relaxation time, we have performed the simulation in the weak interaction limit. In Fig. 3.6 we show the variance for various interaction strengths  $R^6$  in the presence of global (a) and local (b) noise. For global noise [see Fig. 3.6 (a) inset], the relaxation behaviour and steady-state variance for  $R = 0$  are fundamentally different from an interacting system with  $R \neq 0$ . This is due to the fact that for  $R = 0$  the ground state couples to the symmetric state, i.e. Dicke states [110], yet the symmetric states uncouple to the non-symmetric states. For  $R \neq 0$ , they no longer



uncouples to the non-symmetric states, instead the symmetric states with  $N_e \geq 2$  are shifted due to Rydberg-Rydberg interactions, resulting in a symmetry breaking and population transfer from symmetric states to non-symmetric ones. This leads to a different steady-state variance compared to  $R = 0$ . Furthermore, a slight increase in the interaction strength leads to strongly reduced relaxation times as long as  $R^6 \ll \xi$  [see Fig. 3.6 (a)]. Conversely, the variance in the presence of local noise shows a completely different relaxation behaviour and reaches a different steady state. As shown in Fig. 3.6 (b), the relaxation of variance and the steady state are completely independent of the interaction strength for the small energetic shifts considered. This is due to the fact that for local noise in the absence of interactions, each atom experiences a different time-dependent detuning, resulting in a coupling between symmetric and non-symmetric states. In this weak interaction limit, the relaxation time for global noise is longer than for local noise.

We now discuss the dynamical evolution of the distribution of excitation number and classify the type of distribution in the steady state according to the criteria mentioned above. We show the probabilities  $P_{N_e}$  for finding  $N_e$  excitations at different times in Fig. 3.7, comparing the results for global and local noise. For global noise in the absence of interactions, as shown in Fig. 3.7 (a-d), the population of ground state  $|gg\dots g\rangle$  is slowly transferred to higher excitation numbers only via the symmetric states, relaxing towards uniform distribution. The steady-state probabilities  $P_{N_e} = 1/(N+1)$ . Thus, the variance can be calculated analytically for  $N$  atom number, which is given by

$$(\Delta f_e)^2 = \frac{\sum_{N_e}^N N_e^2 - \frac{1}{N+1} \left( \sum_{N_e}^N N_e \right)^2}{\sum_{N_e}^N N_e} \quad (3.42)$$

In the presence of interactions, the population transfer via the symmetric states is followed by the transfer into non-symmetric states, giving rise to a non-uniform distribution. As shown in Fig.3.7(d), the non-uniform distribution corresponds to a super-Poissonian distribution in which the steady-state variance  $(\Delta f_e)^2 > (f_e = 0.5)$ .

Fig. 3.7 (e-h) shows the excitation distribution in the presence of local noise. The population transfer shows different behaviour compared to the case of global noise. In the absence of interactions, since the symmetric state is already coupled to non-symmetric states, the ground state population is rapidly transferred to higher excitation numbers. For  $(R^6 \ll \xi)$ , the relaxation is unchanged. The steady-state variance exhibits a Poissonian distribution for both cases  $((\Delta f_e)^2 = f_e = 0.5)$ , shown in Fig. 3.7 (h) [red and green bars]. The Poisson distribution can be expressed as

$$P(N_e, N, f_e(\infty)) = \binom{N}{N_e} f_e(\infty)^{N_e} (1 - f_e(\infty))^{N-N_e}. \quad (3.43)$$

For example, for  $N_e = 3$  and  $N = 6$  one obtains  $P(N_e, N, f_e(\infty)) \simeq 0.3125$ , in agreement with the simulation results in Fig. 3.7 (h-red and green bars).

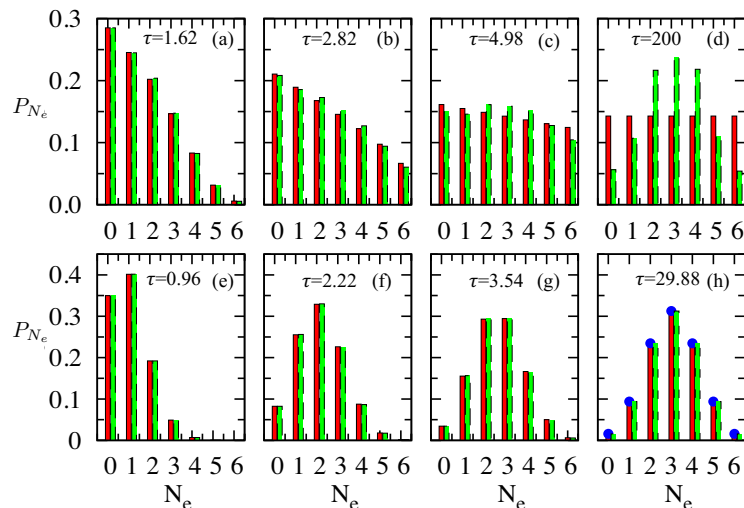


**Figure 3.7:** Dynamics of the excitation probability  $P_{N_e}$  as a function of the excitation number  $N_e$  for the non-interacting (red bars) and interacting (green bars) case in the presence of global (a-d) and local (e-h) noise. Panels (a-d) correspond to the parameters in Fig. 3.6 (a)-inset and (e-h) correspond to the parameters in Fig. 3.6(b) for  $R^6 = 0$  and  $R^6 = 0.06$ .

For intermediate interaction strengths, the distribution of excitation number for local noise starts to show a dependence on the interaction strength. As shown in Fig. 3.8(a), the increase of the interaction strength  $R^6$  slows down the variance relaxation. The slow down is followed by the emergence of a dip that corresponds to the transition of the fraction of Rydberg atoms to the transient state in Fig. 3.5. For global noise [see Fig. 3.8 (b)], as we enter the intermediate interaction regime ( $R^6 \leq \xi$ ), the interaction strength starts to slow down the relaxation and the dip emerges at a later time than for local noise [see Fig. 3.8 (c)]. This means that global noise slows down the transition to the transient state as compared to local noise.

In the presence of global noise, we have seen that the steady-state variance in a chain of 6 atoms differs for non-interacting and interacting cases. An interesting question is whether this difference depends on the atom number. Fig. 3.8(d)[inset] shows the comparison of variances between non-interacting and interacting atoms. For the non-interacting case, it is worth noting that the steady-state variance increases linearly with  $N$ . As the interaction is switched on, the fluctuations of excitation number are strongly suppressed, evident from the decrease of variance with increasing number of atoms that converges to a value  $(\Delta f_e(\infty))^2 > 0.5$ , slightly above the steady-state in the presence of local noise [see Fig. 3.8(d)]. The emergence of different steady states is due to the fact that for global noise the symmetric state for  $N_e = 1$  only gets shifted due to the global noise. For local noise, the distribution follows a Poissonian distribution for the non-interacting and interacting case, resulting in a constant variance for any number of atoms.

We have shown that both types of noise give rise to a characteristic distribution of the Rydberg excitation number. In the next section, we finally discuss implications for experiments of the two-described section above.

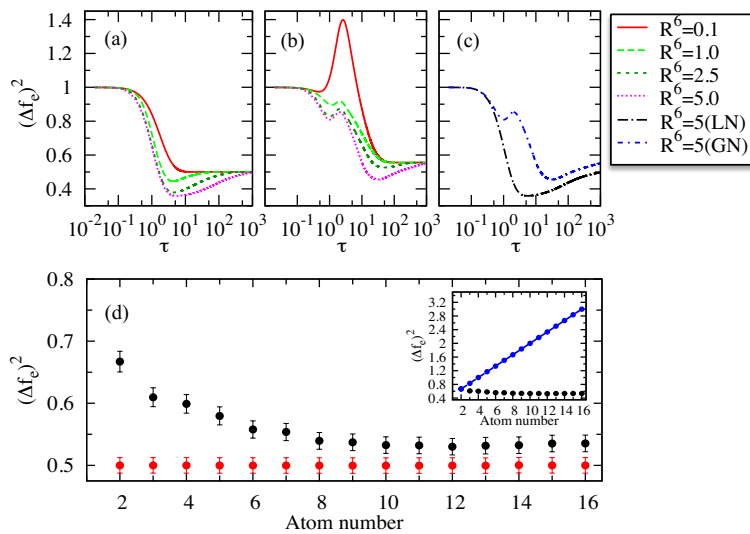


**Figure 3.8:** Variance as a function of time for  $\xi = 5$  in the limit of intermediate interactions and the presence of (a) local noise or (b) global noise. (c) shows a comparison of both cases [global noise (GN) and local noise (LN)] for  $R^6 = 5$  calculated by the master equation. Panel (d) shows the steady-state variance as a function of the atom number  $N$  for interacting atoms in the presence of global (black dots) and local (red dots) noise calculated by the Langevin equation for  $5 \times 10^4$  realisations. In the presence of global noise (inset), non-interacting atoms (blue dot-dashed) show a linear increase of the variance with the atom number (exponent :  $0.167 \pm 0.01$ ) while for interacting atoms the variance decreases.

### 3.6 Implications for experiments

For the Rydberg ensemble in the presence of laser phase noise described in section 3.1, the dynamics of the Ising-like spin-1/2 system can be experimentally realised in a transverse field with up to thirty spins, for a variety of geometries in one and two dimensional lattices, and for a wide range of interaction strengths [111]. The noise can be generated by the arbitrary waveform generator. The bandwidth of this noise can be controlled by applying a low-pass filter of cut-off frequency. For the local noise, one should use separated single beam which produces uncorrelated beams<sup>†</sup>. The interaction strength  $V_0$  can be tuned by varying the lattice spacing  $a$  and changing the principal quantum number  $n$ , since  $V_0$  scales approximately as  $n^{11}$ . For a specific example, laser excitation of Rb( $58S_{1/2}$ ) Rydberg states with  $\Omega/2\pi = 165\text{kHz}$  and  $\Gamma/2\pi = 0.7\text{MHz}$  yields  $\xi = 4$  [32]. For a lattice constant of  $a \approx 3.45\mu\text{m}$  these conditions corresponds to  $R \approx 1.5$ , i.e., well within the parameter region of strong interactions shown in Fig. 3.5(b)-(d). The interaction strength  $R$  can be increased by tuning the laser excitation to higher principle quantum numbers, for example Rb( $67S_{1/2}$ ) yields  $R \approx 2.0$  and Rb( $75S_{1/2}$ ) yields  $R \approx 2.5$ . The speed up of the variance relaxation in the limit of weak interactions [see Fig. 3.6] can be observed when choosing larger lattice spacings  $a$ . For laser excitation of Rb( $58S_{1/2}$ ), a lattice spacing in the range of  $a \approx 8 - 14\mu\text{m}$  yields  $R^6 \approx 0.01 - 0.35$ , well within the parameter region shown in Fig. 3.6 and 3.7. The dependence of the steady-state variance on the number of

<sup>†</sup> Discussion with Thierry Lahaye

atoms can be observed by adding up to 30 atoms.

# Rydberg ensembles in the presence of dissipation

## Contents

---

<b>4.1 Basic Setup</b>	<b>35</b>
<b>4.2 Rydberg lattices with two-level atoms</b>	<b>35</b>
<b>4.3 Rydberg lattices with three-level atoms</b>	<b>38</b>
<b>4.4 Emergence of long-range order</b>	<b>43</b>
<b>4.5 Implications for experiments</b>	<b>45</b>

---

In the previous chapter, we have considered the dynamics and steady state of a one-dimensional lattice of two-level atoms in the presence of laser phase noise. There, we have found intriguing relaxation behaviour and steady-state distributions. An interesting question is: How do the dynamics and steady state behave when the decoherence originates from spontaneous decay instead of laser phase noise?. The non-equilibrium physics of such driven open systems and its relation to universal behaviour [112] in equilibrium have attracted considerable interests [8, 113, 114]. We show here that driven Rydberg gases are ideal systems to experimentally access non-equilibrium steady-state phase transitions.

Previous works predicted the emergence of steady states with antiferromagnetic (AF) order on the basis of mean field theory (MF) assuming nearest neighbour (NN) interactions [33]. Yet, large single-site fluctuations related to a simple two-level driving scheme restrict the emergence of such ordering to short length scales in all lattice dimensionalities [34]. The other driving scheme (e.g. in three-level systems) in a 1D setting fails to realise crystallisation [34–36]. MF predictions are also in conflict with variational calculations [37, 38] and field-theoretical methods [39]. Hence, the possibility of long-range order in dissipative Rydberg lattices as well as the physics of the associated phase transition have

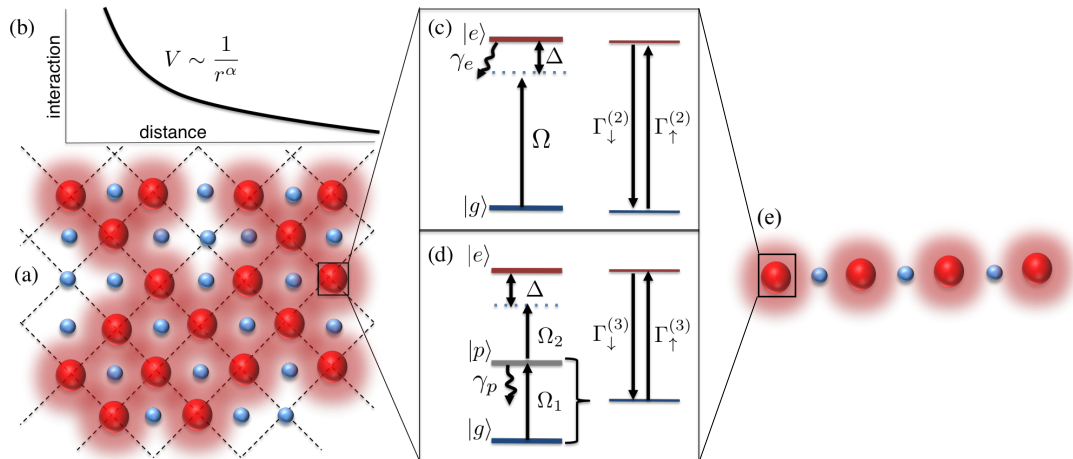


**Figure 4.1:** Schematics of a two- (a) and a one-dimensional (e) lattice in which ground-state atoms (small blue spheres) are laser excited to Rydberg states (large red spheres). The interplay of dissipation and Rydberg-Rydberg interactions (b) can give rise to antiferromagnetic long-range order, where excitations predominantly occupy one checkerboard sublattice. A possible realisation of such a two level system with tunable exception rates  $\Gamma_{\downarrow}^{(2)}$  and  $\Gamma_{\uparrow}^{(2)}$  and effective two-level systems with tunable excitation rates  $\Gamma_{\downarrow}^{(3)}$  and  $\Gamma_{\uparrow}^{(3)}$  is illustrated in (c) and (d), respectively (see text for details).

thus far remained an open question.

In this chapter, we address this issue and show that a long-range-ordered AF phase can be realised in dissipative Rydberg lattices when subjected to appropriate coherent driving. In contrast to the equilibrium physics of the corresponding unitary systems, which is well described by mean field models [67] and NN approximations [68], fluctuations as well as the weak tail of the rapidly decaying interactions are both found to be essential for the physics of the dissipative phase transition.

The chapter is organised as follows. In Sec. 4.1, we will describe the setup associated with Fig. 4.1. In Sec. 4.2, we will investigate the emergence of AF long-range order for two-level driving scheme in the presence of spontaneous decays, where the Rydberg ensembles are considered as interacting spin-1/2 particles in either in a one- or two-dimensional lattice. In Sec. 4.3, we then extend the system to three-level driving scheme in the presence of strongly spontaneous decays from the intermediate state. We characterise the emergence of AF order and determine the steady-state phase diagram in Sec. 4.4. Finally, we discuss a possible implications for experiments for the described systems in Sec. 4.5.

## 4.1 Basic Setup

We consider laser-driven atoms on a one- and a two-dimensional lattice [see Fig. 4.1 (a) and (e)]. In Sec. 4.2, an ensemble of  $N$  two-level atoms, each with a ground state  $|g\rangle$  and a highly excited (Rydberg) state  $|e\rangle$  [see Fig. 4.1(c)], is placed in neighbouring sites of a one- or quadratic lattice of length  $L$  with lattice spacing  $a$ . A pair of excited atoms at sites  $\mathbf{r}_i$  and  $\mathbf{r}_j$  experiences the van der Waals (vdW) interaction  $V_0/|\mathbf{r}_i - \mathbf{r}_j|^6$  with  $V_0 = C_6/a^6$  and  $C_6 > 0$ . For a one-dimensional (1D) lattice,  $|\mathbf{r}_i - \mathbf{r}_j| = |i - j|$  and for a two-dimensional (2D) lattice, site  $\mathbf{r}_i = (x_i, y_i)$ ,  $x_i, y_i \in [1, L]$ . Resonant transitions between two states are driven by a laser with Rabi frequency  $\Omega$ , which subject to the spontaneous decay from state  $|e\rangle$  at rate  $\gamma_e$ .

In Sec. 4.3, instead of two-level driving scheme, we consider a three-level ladder-type system which is excited and de-excited by two lasers with different Rabi frequencies  $\Omega_1, \Omega_2$  and detuning  $\Delta$ . The excited, intermediate, and ground states of atom  $i$  are denoted by  $|e^{(i)}\rangle$ ,  $|p^{(i)}\rangle$  and  $|g^{(i)}\rangle$ , respectively [see Fig.4.1 (a) and (d)]. A pair of excited atoms at sites  $\mathbf{r}_i$  and  $\mathbf{r}_j$  experiences power law interactions. For a lattice spacing  $a$  the nearest-neighbour coupling is  $V_0 = C_\alpha/a^\alpha$  where  $C_\alpha > 0$  determines the interaction strength. Dipole-dipole interactions are associated with  $\alpha = 3$  and  $\alpha = 6$  with van-der-Waals (vdW) interactions. In addition, the system undergoes decoherence due to strong spontaneous decay from state  $|p\rangle$  at rate  $\gamma_p$  [see Fig. 4.1 (d)].

## 4.2 Rydberg lattices with two-level atoms

For the setup described in the previous section, the time evolution of the density matrix and the Hamiltonian that governs the system are given in Eq. 3.30 and in Eq. 3.22, respectively. The superoperator which describes the spontaneous decay from the state  $|e\rangle$  (see Fig. 4.1 (c)) reads

$$\mathcal{L}[\hat{\rho}] = \gamma_e \sum_i \left[ \hat{\sigma}_{ge}^{(i)} \hat{\rho} \hat{\sigma}_{eg}^{(i)} - \frac{1}{2} \{ \hat{\sigma}_{ee}^{(i)} \hat{\sigma}_{ee}^{(i)}, \hat{\rho} \} \right], \quad (4.1)$$

with  $\hat{\sigma}_{\alpha\beta} = |\alpha\rangle\langle\beta|$ . The optical Bloch equations for a two-level atom are given by

$$\begin{aligned} \dot{\rho}_{gg} &= i \frac{\Omega}{2} (\rho_{ge} - \rho_{eg}) + \gamma_e \rho_{ee} \\ \dot{\rho}_{ge} &= i \frac{\Omega}{2} (\rho_{ee} - \rho_{gg}) - i \Delta \rho_{eg} - \gamma_e \rho_{eg} \\ \dot{\rho}_{eg} &= i \frac{\Omega}{2} (\rho_{gg} - \rho_{ee}) + i \Delta \rho_{ge} - \gamma_e \rho_{ge} \\ \dot{\rho}_{ee} &= i \frac{\Omega}{2} (\rho_{eg} - \rho_{ge}) - \gamma_e \rho_{ee}. \end{aligned} \quad (4.2)$$

In the presence of strong decoherence, the quantum dynamics can be reduced to the diagonal elements of  $\rho$  upon adiabatic elimination of its coherences [106]. The derivation

steps in Sec. 3.2 lead to a classical rate equation model in Eq. 3.40. In the presence of spontaneous decay, the specific form of single-atom rates of a two-level atom  $\Gamma_{\uparrow\downarrow}^{(2)}$  reads

$$\Gamma_{\uparrow}^{(2)}(\delta_i) = \frac{\Omega^2 \gamma_e}{\gamma_e^2 + 4\delta_i^2} \quad (4.3)$$

and

$$\Gamma_{\downarrow}^{(2)}(\delta_i) = \frac{\gamma_e^3 + (\Omega^2 + 4\delta_i^2) \gamma_e}{\gamma_e^2 + 4\delta_i^2}, \quad (4.4)$$

where  $\Gamma_{\uparrow}^{(2)}(\delta_i)$  and  $\Gamma_{\downarrow}^{(2)}(\delta_i)$  denote the excitation and de-excitation rates, respectively. The single-atom steady state reads

$$\bar{\rho}_i(\delta_i) = \frac{\Gamma_{\uparrow}^{(2)}}{\Gamma_{\uparrow}^{(2)} + \Gamma_{\downarrow}^{(2)}} = \frac{p_0}{1 + \delta_i^2/\omega^2}, \quad (4.5)$$

with  $p_0$

$$p_0 = \frac{\Omega^2}{(\gamma_e^2 + 2\Omega^2)}, \quad (4.6)$$

and  $\omega$  being Lorentzian width

$$\omega = \frac{\gamma_e^2 + 2\Omega^2}{4}. \quad (4.7)$$

The interactions enter through an effective frequency detuning

$$\delta_i = \Delta - V_0 \sum_{j \neq i} \frac{S_j}{|\mathbf{r}_i - \mathbf{r}_j|^6} \quad (4.8)$$

which accounts for the level shift of the  $i$ th atom due to its surrounding Rydberg excitations [24]. In order to confirm the simplification of the time evolution, we have performed quantum simulations of smaller lattices by means of Monte Carlo wave function (MCWF) method [115–118], where the detailed algorithm is given in appendix B.1. Fig. 4.2 shows the fraction of Rydberg atoms  $f_e = N_{ee}/N$  as the function of excitation probability calculated by MCWF and dynamic Monte Carlo (DMC) methods. Here,  $p_0 \leq 0.5$  is the limit of two-level driving scheme. For  $p_0 < 0.1$ , i.e.,  $\gamma_e \gg \Omega$  the dMC is in excellent agreement with MCWF, confirming the limit of the strong decoherence. As  $p_0$  increases to  $0.1 \leq p_0 \leq 0.3$ , the dMC slightly deviates from a MCWF method. The small discrepancy in the region around  $\Delta = 0$  is due to the fact that for  $\Omega \sim \gamma_e$ , is not fully justified to neglect the nonlinear short-time population dynamics. For  $p_0 > 0.3$ , i.e.,  $\Omega \gg \gamma_e$  the coherence prevails. Consequently, the discrepancy is more apparent compared to the case  $\Omega \sim \gamma_e$ .

In order to detect the AF order, we define the order parameter  $q$ ,

$$q = \frac{|N_e^A - N_e^B|}{N_{ee}}, \quad (4.9)$$

where  $N_{ee}$  is the total number of excitation in a lattice. The excited state populations



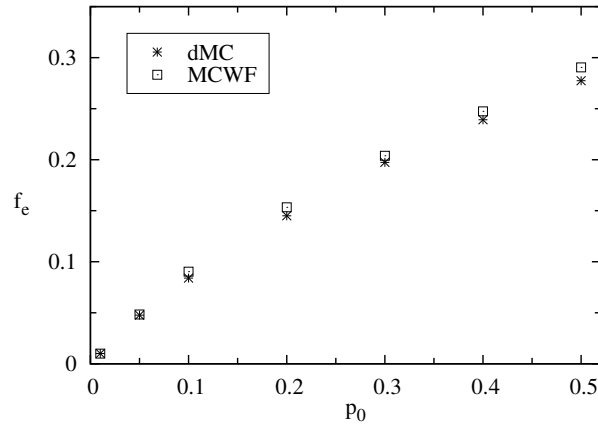


**Figure 4.2:** Fraction of Rydberg atoms in a two-dimensional lattice as a function of excitation probability  $p_0$  calculated by MCWF (rectangular points) and dMC (star points). The simulations were performed with NN approximation and the remaining parameters are  $V_0 = 1\omega$ ,  $\Delta = 0$ ,  $\alpha = 6$ , and  $N = 4 \times 4$ .

on the checkerboard sublattices A and B are denoted by  $N_e^A$  and  $N_e^B$ , respectively. As illustrated in Fig.4.1,  $q$  measures the population imbalance on the two sublattices reflecting a checkerboard ordering, with  $q > 0$  in the ordered phase and  $q = 0$  in the disordered phase that corresponds to a paramagnetic phase.

Fig. 4.3 shows the  $q$  parameter as a function of excitation probability  $p_0$  under the assumption of a NN-blockade. For two-level driving scheme, the steady state in the thermodynamic limit indeed does not exhibit the AF order for 1D and 2D settings [see Fig. 4.3 (c) and (d), where extrapolations to thermodynamic limit are shown in (a) and (b)]. This is in agreement with [34] in which the large single-site fluctuations associated with a simple two-level driving scheme restricts the emergence of that ordering to short length scales for all spatial lattice dimensions. The above model is also analytically solvable and shows no long-range order crystallisation [112]. The steady state may exhibit Néel order provided that  $p_0 \sim 0.791$ . Thus, for simple two-level driving crystallisation is impossible in any dimension since  $p_0 \leq 0.5$ . Therefore, the population inversion, e.g., via electromagnetically induced transparency [119–122], is required for the AF order to occur, i.e., the probability of populating the Rydberg state must be greater than 0.5 ( $p_0 > 0.5$ ). This is accomplished in three-level atomic systems in which there are two coherent routes for absorption that can destructively interfere, thus leading to the cancellation of absorption. In the next section, we provide the population inversion via three-level driving scheme. We investigate the dynamics of Rydberg lattices in the limit of strong decoherence.

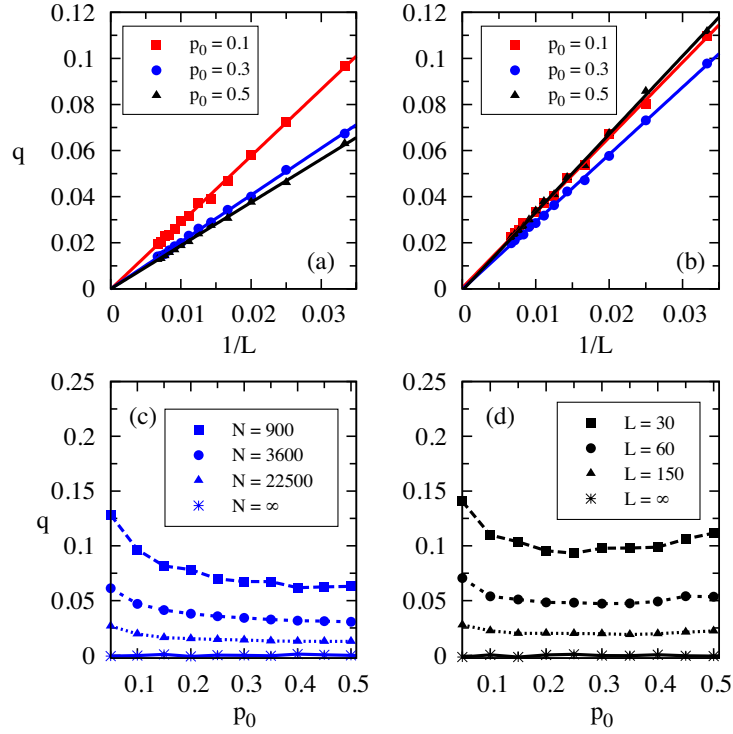


**Figure 4.3:** The extrapolation to the thermodynamic limit,  $L \rightarrow \infty$ , for 1D and 2D lattices are plotted in (a) and (b), respectively. Panels (c) and (d) show  $q$  parameter as a function of excitation probability  $p_0$  for the case of 1D and 2D, respectively. The simulations were performed with NN approximation and the symbols show results for finite system size given in the legend. The remaining parameters are  $\Delta = 0$ ,  $V_0 = 5\omega$ , and  $\alpha = 6$ .

### 4.3 Rydberg lattices with three-level atoms

For the three-level scheme described in the Sec. 4.1, the  $N$ -body density matrix is given in Eq. 3.30 and the Hamiltonian that governs the systems reads

$$\hat{H}_I = \sum_i \hat{H}_i + V_0 \sum_{i < j} \frac{\hat{\sigma}_{ee}^{(i)} \hat{\sigma}_{ee}^{(j)}}{|\mathbf{r}_i - \mathbf{r}_j|^\alpha}, \quad (4.10)$$

$$\hat{H}_i = \frac{\Omega_1}{2} \left( \hat{\sigma}_{pg}^{(i)} + \hat{\sigma}_{gp}^{(i)} \right) + \frac{\Omega_2}{2} \left( \hat{\sigma}_{ep}^{(i)} + \hat{\sigma}_{pe}^{(i)} \right) - \Delta \hat{\sigma}_{ee}^{(i)}. \quad (4.11)$$

The first part is a local Hamiltonian  $\hat{H}_i$  that contains the atom-light interactions. The second part describes the power-law interactions between two Rydberg atoms. The superoperator which describes the spontaneous decay from the state  $|e\rangle$  (see Fig. 4.1 (c)) is given by

$$\mathcal{L}[\hat{\rho}] = \gamma_p \sum_i \left[ \hat{\sigma}_{gp}^{(i)} \hat{\rho} \hat{\sigma}_{pg}^{(i)} - \frac{1}{2} \{ \hat{\sigma}_{pg}^{(i)} \hat{\sigma}_{gp}^{(i)}, \hat{\rho} \} \right], \quad (4.12)$$

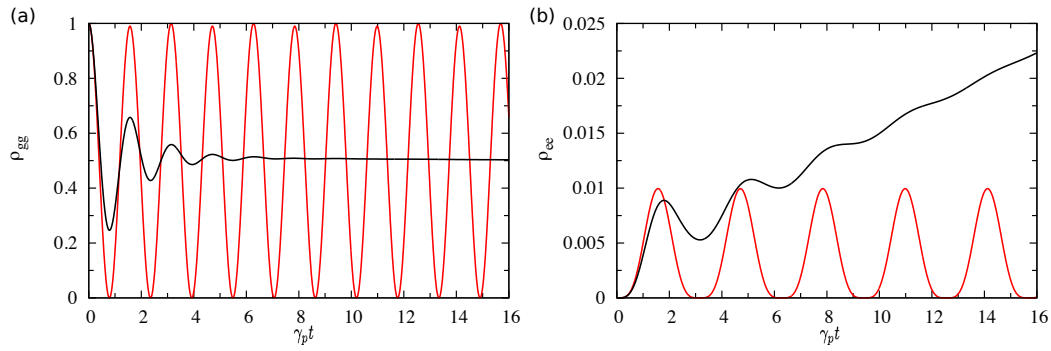


**Figure 4.4:** The population of the ground state (a) and Rydberg state (b) in the presence (black) and absence (red) of spontaneous decays from the state  $|p\rangle$ . The remaining parameters are:  $\Delta = 0$ ,  $\Omega_1 = 4\gamma_p$ , and  $\Omega_2 = 0.2\gamma_p$ .

with the OBE of a single atom for the three level scheme,

$$\begin{aligned}
\dot{\rho}_{gg} &= i\frac{\Omega_1}{2}(\rho_{gp} - \rho_{pg}) + \gamma_p\rho_{pp} \\
\dot{\rho}_{pp} &= -i\frac{\Omega_1}{2}(\rho_{gp} - \rho_{pg}) - i\frac{\Omega_2}{2}(\rho_{ep} - \rho_{pe}) - \gamma_p\rho_{pp} \\
\dot{\rho}_{ee} &= i\frac{\Omega_2}{2}(\rho_{ep} - \rho_{pe}) \\
\dot{\rho}_{gp} &= -i\frac{\Omega_1}{2}(\rho_{pp} - \rho_{gg}) + i\frac{\Omega_2}{2}\rho_{ge} - \frac{\gamma_p}{2}\rho_{gp} \\
\dot{\rho}_{ge} &= -i\frac{\Omega_1}{2}\rho_{pe} + i\frac{\Omega_2}{2}\rho_{gp} - i\Delta\rho_{ge} \\
\dot{\rho}_{pe} &= -i\frac{\Omega_1}{2}\rho_{ge} + i\frac{\Omega_2}{2}(\rho_{pp} - \rho_{ee}) - i\Delta\rho_{pe} - \frac{\gamma_p}{2}\rho_{pe} \\
\dot{\rho}_{\alpha\beta} &= (\dot{\rho}_{\beta\alpha})^*.
\end{aligned} \tag{4.13}$$

The diagonal elements  $\rho_{\alpha\alpha}$  of the density matrix (populations) indicate the probability of finding the atom at time  $t$  in the state  $|\alpha\rangle$ . The probability

$$\sum_{\alpha} \rho_{\alpha\alpha} = 1, \tag{4.14}$$

is conserved at all times. Solving a many body problem either via this single-atom basis or quantum trajectory is impossible due its complexity. For example, via a quantum trajectory method, for three-level driving scheme the corresponding Hilbert space scales as  $3^N$ . This, of course, limits the simulation to  $N < 20$  in which for one trajectory of  $N = 14$  is already time consuming. Fortunately, under the set of corresponding experimental parameters [123, 124], one can simplify the complexity of many body problem as in Sec. 3.2 and Sec. 4.2 by means of classical rate equation [125]. In the experiment [123, 124], the upper transition is much more weakly driven than the lower one ( $\Omega_2 \ll \Omega_1$ ), a typical time intensity separation obtained for typical laser intensities reads

$$\Omega_1 \gg \Omega_2 \quad \text{and} \quad \gamma_p \gg \Omega_2. \tag{4.15}$$

This allows us to define two well separated time scales, such that the transition  $|p\rangle \rightarrow |e\rangle$  is slow compared to the transition  $|g\rangle \rightarrow |p\rangle$ . As shown in Fig. 4.4, the rabi oscillation is almost completely eliminated after a short time  $\tau_m = \gamma_p^{-1}$ . During this period, the Rydberg state is hardly populated. On the other hand, the dynamics of the weak Rydberg transition are significantly slower than those of the pump transition. The latter quickly reaches ( $\sim \Omega_1^{-1}$ ) a quasi-steady state, which is only slightly affected by the weak coupling to the Rydberg level. Afterwards, the dynamics of the system proceed on the slow time scale, which is determined by  $\Omega_2^{-1}$  and will reach steady state for  $(\Omega_1/\Omega_2)^2$ . During this period, Rydberg population gradually increases as compared to the completely coherent case [see Fig. 4.4(b)], which shows that the coherence of the fast transition adiabatically follow the slow dynamics of the transitions. Under these conditions, the coherences can be expressed as a function of the populations at each instant of time, i.e., their dynamics can be eliminated adiabatically [126] by setting

$$\dot{\rho}_{\alpha\beta} = 0 \quad \text{for} \quad \alpha \neq \beta \quad (4.16)$$

Solving the algebraic equations from Eq. (4.13) and (4.16) for the populations, employing Eq. (4.14), and inserting into the differential equation for  $\rho_{pp}$  and  $\rho_{ee}$ , one obtains

$$\begin{aligned} \dot{\rho}_{pp} &= q_1\rho_{pp} + q_2\rho_{ee} + q_3, \\ \dot{\rho}_{ee} &= q_4\rho_{pp} + q_5\rho_{ee} + q_6. \end{aligned} \quad (4.17)$$

where the coefficients  $q_k = q_k(\Omega_1, \Omega_2, \Delta, \gamma_p)$  are some functions of the parameters of the three-level system. For further simplification, we use of a relation (4.14), which leads to

$$\dot{\rho}_{pp} - \dot{\rho}_{gg} = 2\dot{\rho}_{pp} + \dot{\rho}_{gg} = 0. \quad (4.18)$$

Hence, the population of the intermediate state in Eq. (4.13) can now be eliminated and we finally obtain a simple linear differential equation describing the dynamics of the Rydberg population,

$$\dot{\rho}_{ee} = -\frac{\Gamma_{\uparrow}^{(3)}}{\bar{\rho}_1}\rho_{ee} + \Gamma_{\uparrow}^{(3)}. \quad (4.19)$$

where  $\bar{\rho}_1$  denotes the steady-state occupation of state  $|e\rangle$  and can be expressed as,

$$\bar{\rho}_1 = \frac{\Omega_1^2 (\Omega_1^2 + \Omega_2^2)}{(\Omega_1^2 + \Omega_2^2)^2 + 4\Delta^2 (\gamma_p^2 + 2\Omega_1^2)}, \quad (4.20)$$

and  $\Gamma_{\uparrow}^{(3)}$  is the rate for populating the Rydberg state for the short time and is expressed as,

$$\Gamma_{\uparrow}^{(3)} = \frac{2\gamma_p (\Omega_2\Omega_1)^2 (\Omega_1^2 + \Omega_2^2)}{a_0 + a_2\Delta^2 + a_4\Delta^4}, \quad (4.21)$$

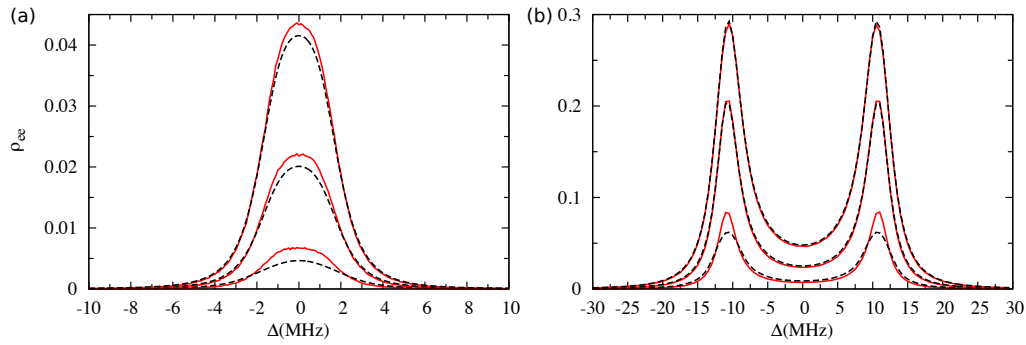


**Figure 4.5:** Population of the Rydberg state for the three-level system calculated by rate equation (4.23) (solid lines) and OBE (4.13) (dashed lines) for different pulse lengths:  $0.3 \mu\text{s}$  (lowest pair of curves),  $1.0 \mu\text{s}$  (middle pair),  $2.0 \mu\text{s}$ . The remaining parameters in MHz are  $(\Omega_1/2\pi, \Omega_2/2\pi, \gamma_p/2\pi) = (4, 0.2, 6)$  in (a) and  $(\Omega_1/2\pi, \Omega_2/2\pi, \gamma_p/2\pi) = (22.1, 0.8, 6)$  in (b)

with

$$\begin{aligned} a_0 &= (\Omega_1^2 + \Omega_2^2) \left[ (\Omega_2^2 - 2\Omega_1^2)^2 + 2\gamma_p^2 (\Omega_1^2 + \Omega_2^2) \right] \\ a_2 &= 8 (\gamma_p^4 - 4\Omega_1^4) + 4\Omega_2^2 (4\Omega_1^2 + \gamma_p^2) + 8\Omega_2^4 \\ a_4 &= 32 (\gamma_p^2 + 2\Omega_1^2). \end{aligned} \quad (4.22)$$

Introducing an effective ground state  $\rho_{gg}^{eff} = 1 - \rho_{ee}$ , one can write Eq. (4.19) in the form of a rate equation for an effective two-level atom

$$\dot{\rho}_{ee} = \Gamma_{\uparrow} \rho_{gg}^{eff} - \Gamma_{\downarrow} \rho_{ee}, \quad (4.23)$$

with de-excitation rate

$$\Gamma_{\downarrow}^{(3)} = \Gamma_{\uparrow}^{(3)} \left( \frac{1 - \bar{\rho}_1}{\bar{\rho}_1} \right). \quad (4.24)$$

A comparison of the solutions of the OBE 4.13 and the rate equation 4.23 rate equation for the Rydberg population as a function of the detuning is shown in Fig. 4.5 for one pulse length. The parameters correspond to those of the experiments [123, 124]. The solution of rate equation is in good agreement with OBE and becomes even better for longer pulses. The discrepancy in the region around  $\Delta = 0$  is due to the fact that for  $\Omega_1 < \gamma_p$ , is not fully justified to neglect the nonlinear short-time population dynamics.

The rate equation reproduces the Autler-Townes splitting of the intermediate level  $|p\rangle$  manifest in a splitting of the Rydberg line, as the steady state with its single central peak is approached for long times when the Rydberg population reaches the saturation limit. A detailed analysis of the peak structure of the Rydberg populations in this system, especially the occurrence of the Autler-Townes splitting and its impact on the excitation blockade, has been given in [106].

Let us now proceed to the case of  $N$  atoms. The effective rate equation for the joint probabilities  $\rho_{S_1, \dots, S_N}$  of Rydberg excitations being present ( $S_i = 1$ ) or not

present ( $S_i = 0$ ) at the  $i$ th site and the corresponding many-body states are connected by the single-atom excitation  $[\Gamma_{\uparrow}^{(3)}(\delta_i)]$  and de-excitation  $[\Gamma_{\downarrow}^{(3)}(\delta_i)]$  rates reads [47, 106, 127, 128]

$$\begin{aligned} \dot{\rho}_{S_1, \dots, S_N} = & \sum_i \left[ (1 - S_i) \Gamma_{\downarrow}^{(3)}(\delta_i) + S_i \Gamma_{\uparrow}^{(3)}(\delta_i) \right] \rho_{S_1, \dots, 1-S_i, \dots, S_N} \\ & - \left[ (1 - S_i) \Gamma_{\uparrow}^{(3)}(\delta_i) + S_i \Gamma_{\downarrow}^{(3)}(\delta_i) \right] \rho_{S_1, \dots, S_i, \dots, S_N} . \end{aligned}$$

The dynamics of Eq. (4.25) can be solved by dynamic Monte Carlo (DMC) technique where the algorithm is provided in the appendix B.2. However, in the full three-level case, non-physical negative rates frequently occur [129]. Although modifying the rates in such a way that the correct steady state is preserved [127], this technique is rather expensive and impractical for general systems. Therefore, we use another approach that has been developed in [128]. There, the calculation of the dynamics of the system was neglected in favour of the steady-state calculation. In this technique, we use the steady-state of Rydberg state which is given by

$$\bar{\rho}_i(\delta_i) = \frac{\Gamma_{\uparrow}^{(3)}}{\Gamma_{\uparrow}^{(3)} + \Gamma_{\downarrow}^{(3)}} = \frac{p_0}{1 + \delta_i^2/\omega^2}. \quad (4.25)$$

where

$$p_0 = \Omega_1^2 / (\Omega_1^2 + \Omega_2^2) \quad (4.26)$$

and  $\omega$  denotes Lorentzian width with

$$\omega = \frac{\Omega_1^2 + \Omega_2^2}{2\sqrt{\gamma_p^2 + 2\Omega_1^2}}, \quad (4.27)$$

For the case of  $N$  interacting atoms, deriving the interacting part of Hamiltonian 4.10 and neglecting multi-photon transitions, one ends in the structure of the master equation in which the interactions enter through an effective frequency detuning [106]

$$\delta_i = \Delta - V_0 \sum_{j \neq i} \frac{S_j}{|\mathbf{r}_i - \mathbf{r}_j|^\alpha} \quad (4.28)$$

which accounts for the level shift of the  $i$ th atom due to its surrounding Rydberg excitations. All parameters are scaled by the Lorentzian width  $\omega$ , the many-body state is fully described by only four-parameter: the power law exponent  $\alpha$ , the resonant excitation probability  $p_0$ , laser detuning  $\Delta/\omega$  and the interaction strength  $V_0/\omega$ . For the settings discussed in here [cf. Fig.4.1 (d)], the rates can be expressed as  $\Gamma_{\downarrow}^{(3)}(\delta_i) = (1 - \bar{\rho}_i)/T$ ,  $\Gamma_{\uparrow}^{(3)}(\delta_i) = \bar{\rho}_i/T$  where  $T(\delta_i)$  denotes the relaxation time. In the next section, we discuss the emergence of long-range AF order in a two-dimensional lattice case.

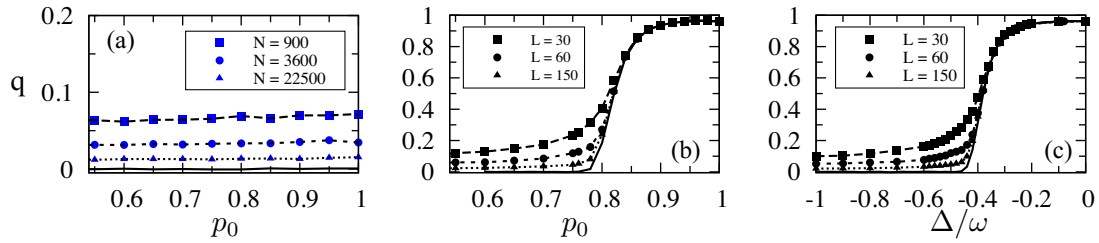


**Figure 4.6:** Panel (a)  $q$  parameter as a function of  $p_0$  for  $\Delta = 0$  and  $V_0 = 5\omega$  in the case of 1D system and (b) 2D system. The  $q$  parameter as a function of  $\Delta$  for  $p_0 \simeq 0.95$  and  $V_0 = 5\omega$  in the case of 2D system. The simulations were performed with NN approximation and the symbols show results for finite system sizes given in the legend. The thick solid line shows the extrapolation to the thermodynamic limit.  $L \rightarrow \infty$

## 4.4 Emergence of long-range order

This section provides the condition in accomplishing the AF order in a three-level driving scheme. For the one-dimensional lattice case, under the assumption of a NN-blockade, the above model is analytically solvable and shows no long-range order crystallisation [130]. This is confirmed in Fig. 4.6(b), 1D indeed shows no AF long-range order for  $p_0 \geq 0.5$ . The emergence of such ordering only occurs in a few system size, e.g.,  $N < 30$  [131]. As the system size increases to the thermodynamic limit,  $q \simeq 0$ .

In higher dimensions, the steady states of Néel order occur for  $p_0 \sim 0.7914$  in 2D and  $p_0 \sim 0.749$  in 3D square lattices [130]. In order to confirm the analytical result, we perform ssMC simulation in the NN-approximation. As shown in Fig.4.6(c), the steady state indeed exhibits Néel order provided that  $p_0 \sim 0.7914$  for  $\Delta \approx 0$  and interactions. This is due to the fact that in the three-level scheme  $p_0$  exceeds the limit of two-level driving scheme  $p_0 > 0.5$  due to the presence of the dark state. The mechanism of the dark state for lasing without inversion is given in the appendix C and can be found in [120, 132].

To Fig. 4.6, the simulations were performed with NN approximation and shows that AF order occurs for  $\Delta \simeq 0$  [see Fig. 4.6(d)]. However, when considering the full range power tail interactions for resonantly driven atoms with varying exponents  $\alpha$  and  $p_0 = 0.95$ , as shown in Fig.4.7, we do not observe long-range order for realistic interaction potentials. In particular, the NN approximation fails qualitatively for the important case of vdW interactions ( $\alpha = 6$ ). Surprisingly, the weak tail of the interactions prevents crystallisation until a rather larger value  $\alpha \approx 11$ . In fact, the simulations show that resonantly driven atoms, with vdW interactions remain in the disordered phase for any values of  $p_0$  and  $V_0$ .

The fact that there is no phase transition on resonance for  $\alpha = 6$  can be qualitatively understood as follows: a macroscopic population imbalance on the two sublattices each with a lattice constant  $\sqrt{2}a$  characterises a Néel state. Assuming that an atom on the

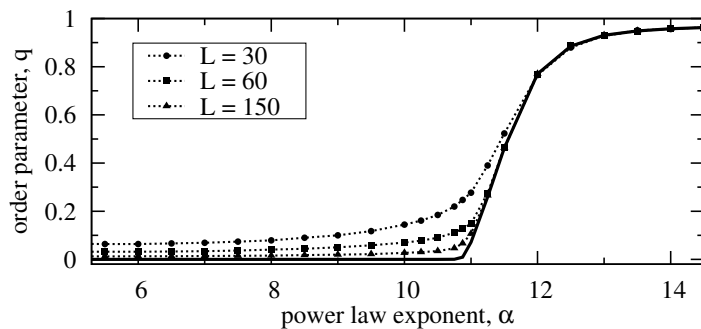


**Figure 4.7:** Order parameter  $q$  as a function of the power-law exponent  $\alpha$ , for  $p_0 = 0.95$  and  $V_0 = 5\omega$  and resonant driving  $\Delta = 0$ . The symbols correspond to different system sizes given in the legend. The thick solid line is the extrapolation to the thermodynamic limit,  $L \rightarrow \infty$ . The finite-size scaling shows a linear increase of the order parameter in the critical regime (exponent :  $1 \pm 0.05$ ). (After [40], © American Physical Society, reproduced with permission.)

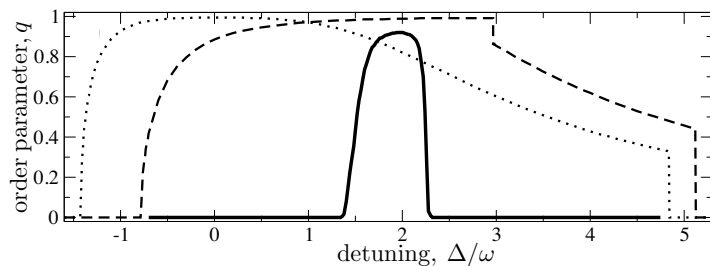


**Figure 4.8:** Order parameter  $q$  as a function of laser detunings  $\alpha$  by means of sSMC (solid line), meanfield for NN interaction (dotted line), and full vdW interactions (dashed line). The remaining parameters are  $p_0 = 0.96$  and  $V_0 = 5\omega$ . (after [40], © American Physical Society, reproduced with permission.)

highly populated sublattice has an average  $z$  nearest neighbours, the vdW interactions cause an energetic shift of  $zV_0/8\omega$  and  $z \approx 3$  near the crystallisation transition. Therefore, the laser detuning  $\Delta$  must compensate the corresponding energetic shift such that its excitation probability remains above threshold  $\bar{\rho}_1(\Delta/\omega - zV_0/8\omega) \geq p_c$ , with  $\bar{\rho}_1$  given in Eq. (4.25). As shown in Fig. 4.8, the phase transition between the AF and paramagnetic phase occurs for finite detunings  $\Delta$ .

In Fig. 4.8, we identify the advantages of Monte Carlo simulations over mean field methods to quantitatively assess the importance of fluctuations and the shape of the interaction potential [33, 35, 36]. The detail about a mean field method for three-level driving scheme with NN and full vdW interaction is provided in the appendix B.3. As shown in Fig. 4.8, the phase transition is a second order phase transition [40], in contrary to mean field predictions that suggest a first order transition. Furthermore, the AF order occurs for finite detunings  $\Delta$ ,  $p_0$  and  $V_0$  [see Fig. 4.9]. Néel-type ordering emerges within a finite detuning range and for  $p_0 > p_c \approx 0.86$ , only slightly larger than the threshold in



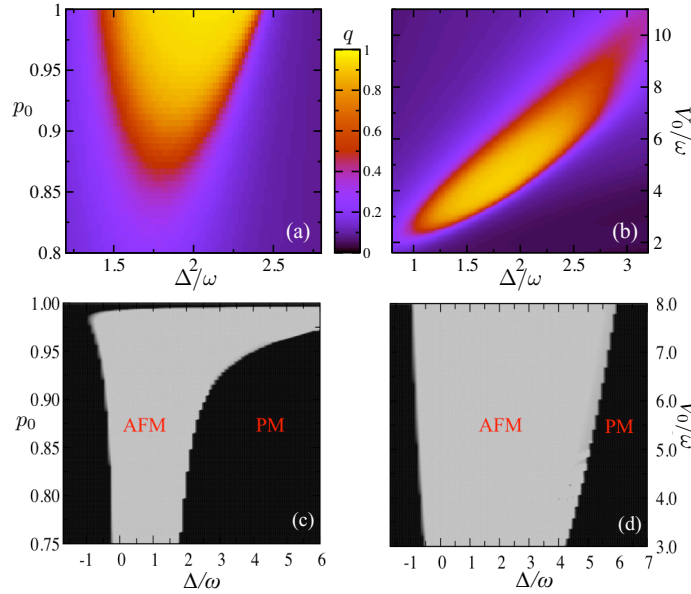


**Figure 4.9:** Order parameter obtained for a  $30 \times 30$  lattice as a function of  $\Delta$  and  $p_0$  for  $V_0 = 5\omega$  (a) and as a function of  $\Delta$  and  $V_0$  for  $p_0 = 0.96$  (b) compared to mean-field predictions for the full vdW interactions (c) and (d). AFM and PM denote antiferromagnetic and paramagnetic order, respectively. ((a) and (b) after [40], © American Physical Society, reproduced with permission.)

the NN-blockade model [130] [see Fig. 4.9 (a)]. In contrast to ssMC, no threshold is present [see Fig. 4.9(c)] for a meanfield method. Néel states are only found in a certain interval of interaction strengths  $V_0$ , since the vdW tail prevents long-range ordering beyond a critical value Fig.4.9(b).

We have shown the emergence of AF long-range order for appropriate coherent driving and certain interval of interaction strengths  $V_0$ . The fluctuations and the shape of interaction potential are both indeed found to be essential for the physics of the dissipative phase transition. In the next section, we discuss the relevant parameters towards an experimental realisation.

## 4.5 Implications for experiments

In the presence of decoherence due to spontaneous emission, the strong radiative decay of the intermediate state  $|p\rangle$  with a rate  $\gamma_p \sim \text{MHz}$  drives the relaxation towards the steady state eq.(4.25), with a tuneable  $p_0 = \Omega_1^2/(\Omega_1^2 + \Omega_2^2)$ . Such three-level excitation schemes are utilised in numerous Rydberg atom experiments, either for exploring interaction effects in the strong excitation regime ( $\Omega_1 > \Omega_2$ ) [133–136] or in quantum optics applications in the opposite limit [77, 137–139]. As a specific example, laser excitation of Rb( $35S_{1/2}$ ) Rydberg states via the intermediate Rb( $5P_{1/2}$ ) state with  $\Omega_1 = 0.5\gamma_p = 4\Omega_2$  yields  $p_0 \approx 0.9$ . For a lattice constant of  $a \approx 2\mu\text{m}$  these conditions correspond to  $V_0 \approx 5\omega$ , i.e. well within the parameter region of the ordered steady state. Rydberg excitation and trapping

[140] as well as single-site resolved Rydberg atom imaging [86] have been experimentally demonstrated in 2D lattices with  $a \approx 0.5\mu\text{m}$ . Larger lattice constants can also be realised in these settings [141] or via single-atom trapping in optical micro-trap arrays [142], such that the creation and probing of the predicted dissipative phase transition appears to be well within experimental reach.

# Interfacing Rydberg atoms and solid-state qubits

## Contents

---

5.1 The Jaynes-Cummings Model . . . . .	49
5.2 $1/f$ noise . . . . .	51
5.3 Noise effects on single-atom dynamics . . . . .	52

---

Having discussed the dynamics of Rydberg atom lattices in the previous chapters, we now describe an application of the strong interactions in such systems for quantum information processing (QIP). More specifically, we show how the special properties of Rydberg atoms can be employed to construct a coherent interface to transfer the quantum states of a superconducting qubit to an atomic quantum memory – a key component for hybrid quantum computing architectures.

A QIP platform should allow one to prepare, manipulate and read out the quantum states of a multi-qubit system. Moreover, such a platform should be scalable, i.e., the more qubits can be added and coupled in order to perform more complex calculations. Superconducting (SC) qubits satisfy these requirements and present one of the most promising current implementations [143–147]. However, the corresponding qubit states are prone to environmental noise from extrinsic (e.g., local electromagnetic environment) and intrinsic (e.g., low frequency noise) decoherence sources, leading to short qubit life times. A hybrid quantum computer presents an attractive solution to this problem by using another physical system in order to store the quantum information for long times. Cold atomic ensembles serve as a suitable quantum memory. Their hyperfine ground states feature transitions in the GHz range and can thus be coupled to the quantum states of microwave photons confined in typical superconducting cavities. In principle, such a setting permits to process quantum information rapidly using well developed SQUID tech-

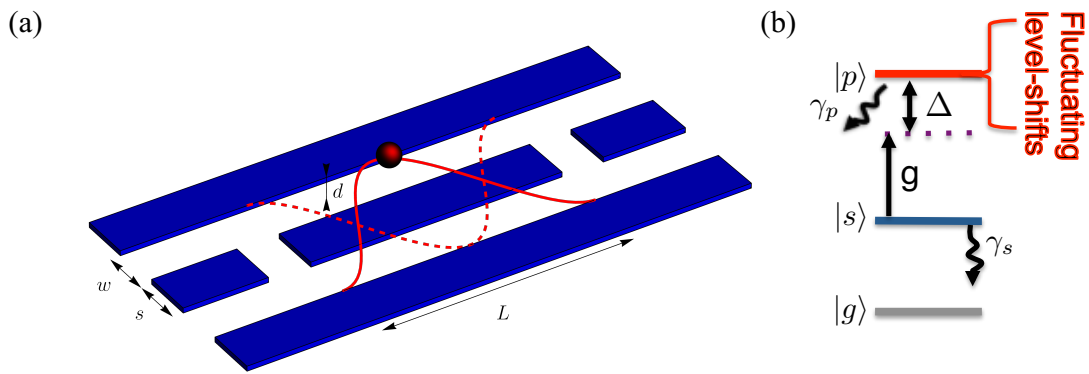


**Figure 5.1:** Illustration of Rydberg atoms coupled to SC cavity (a) and atomic level scheme in the presence of noise and spontaneous decay from the state  $|p\rangle$  and  $|s\rangle$  (b). (see text for the parameters)

nology while storing quantum information for a long times in the hyperfine ground states of atomic ensembles [148]. While a superconducting cavity provides a virtual ideal interface between the SQUID quantum states and the atomic quantum memory, the remaining outstanding challenge is to achieve an efficient and coherent transfer between quantum states encoded in microwave photons in the superconducting cavity and atomic exciton of the quantum memory.

Typically the solid-state qubit is placed at the antinode of a coplanar SC microwave cavity while the atomic ensemble is trapped above the cavity surface [149] and their hyperfine states couple to the evanescent cavity field [150–152]. In order to achieve strong coupling, the atoms must be placed very close to the metallic surface, which exposes them to harmful surface effects, such as static magnetic field noise. Even though one can achieve long coherence times,  $\sim 1$  ms, which can be achieved for  $\mu\text{m}$  atom-surface separations [153], the resulting coupling strengths in the kHz-range are not strong enough to facilitate for a coherent transfer and, even more so, compete with the decoherence time,  $\sim 1\mu\text{s}$ , of SC qubits.

A promising alternative to enhance the atom-cavity coupling is to utilise the large transition dipole moments of highly excited Rydberg states [51, 56–59]. For example,  $nS - nP$  transitions of alkaline precisely fall into the microwave regime, thus, are ideal for coupling atomic Rydberg excitations to coplanar MW cavities [51–55]. Moreover, the use of Rydberg states relaxes the requirement of placing the atoms very close to the surface and thereby eliminates the detrimental effects of magnetic surface fields. However, as the dipole moment increases ( $\propto n^2$ ) the dipole polarisability also increases ( $\propto n^7$ ). This renders the atom more susceptible to electric surface fields, as we show in the chapter, leads to additional decoherence.

## 5.1 The Jaynes-Cummings Model

The interaction of a single Rydberg atom with a near-resonant microwave cavity can be describe by the Jaynes-Cummings model, which represents one of the most simple and central models in quantum optics. As illustrated in Fig. 5.1 (a), we consider an atom with relevant states  $|s\rangle$  and  $|p\rangle$  which represent two  $|nS\rangle$  and  $|n'P\rangle$  Rydberg states whose transition frequency is assumed to be near-resonant with the cavity frequency. Further introducing the creation operator  $\hat{a}^\dagger$  of cavity photons the atom-cavity Hamiltonian can be written as

$$\hat{H} = \hbar g (\hat{a}\hat{\sigma}_{ps} + \hat{a}^\dagger\hat{\sigma}_{sp}) + \hbar\omega_{sp}\hat{\sigma}_{pp} + \hbar\omega_c\hat{a}^\dagger\hat{a} \quad (5.1)$$

where we have used the rotating wave approximation.

The Hamiltonian consists of three parts: the atom-cavity coupling with coupling strength  $g$  determined by the dipole matrix element  $\hat{\mu}_{sp}$  and the electric field per photon  $\varepsilon_c = \sqrt{\hbar\omega_c/\epsilon_0 V_c}$  within the effective cavity volume  $V_c = 2\pi w^2 L$  [see Fig. 5.1 (a)] at the surface of the cavity,

$$g = \hat{\mu}_{sp}\varepsilon_c/\hbar. \quad (5.2)$$

The second part describes the energy difference  $\hbar\omega_{sp}$  between the two atomic states, and the third the energy  $\hbar\omega_c$  of a cavity photon. The length  $L = \lambda_c$  determines the cavity frequency through

$$\omega_c = \frac{2\pi c}{\lambda_c \sqrt{\epsilon_r}}, \quad (5.3)$$

where  $c$ ,  $\lambda_c$ , and  $\epsilon_r$  denote the light speed in vacuum, the wavelength of microwave photon and the medium relative electric permittivity, respectively. We assume that the cavity is initially populated with only one photon and has a lifetime  $1/\kappa$  (typically  $\leq$  ms) larger than any other timescales in the system, so we can safely neglect it. Diagonalising Eq. (5.1) yields the dressed eigenstates of the coupled atom-cavity system

$$\begin{aligned} |+, n_p\rangle &= \sin \theta_{n_p} |s, n_p\rangle + \cos \theta_{n_p} |p, n_p - 1\rangle, \\ |-, n_p\rangle &= \cos \theta_{n_p} |s, n_p\rangle - \sin \theta_{n_p} |p, n_p - 1\rangle \end{aligned} \quad (5.4)$$

with the mixing angle

$$\tan \theta_{n_p} = \frac{\sqrt{n_p}g}{\Delta/2 + \sqrt{g^2 n_p + (\Delta/2)^2}} \quad (5.5)$$

The associated energies are given by

$$E_{n_p, \pm} = n_p \omega_c + \frac{1}{2} \left( \Delta \pm \sqrt{\Delta^2 + 4n_p g^2} \right), \quad (5.6)$$

and depend on the number  $n_p$  of photons in the cavity. For much of the present considerations the photon number is restricted to 1. In the absence of atom-cavity interactions,  $g = 0$ , the bare eigenstates are linear functions of the cavity detuning  $\Delta = \omega_{sp} - \omega_c$

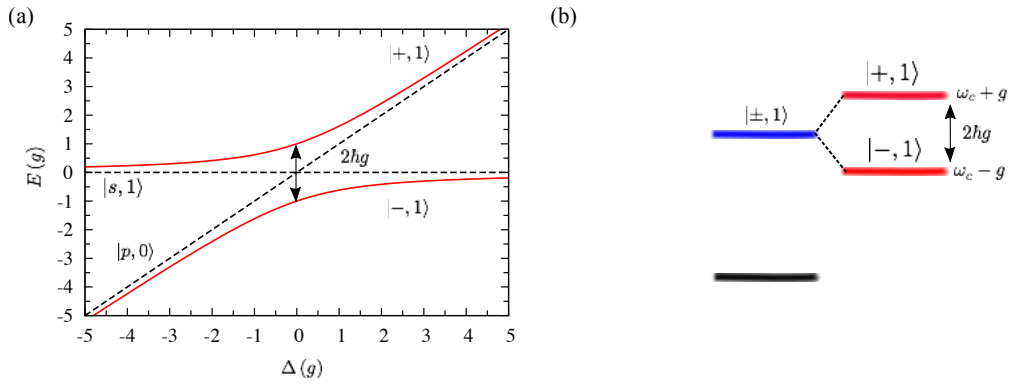


**Figure 5.2:** Panel (a) shows eigenenergy of bare (black dashed) and dressed states (red line) as the function of switchable detuning. (b) shows schematic of eigen energy of collective states.

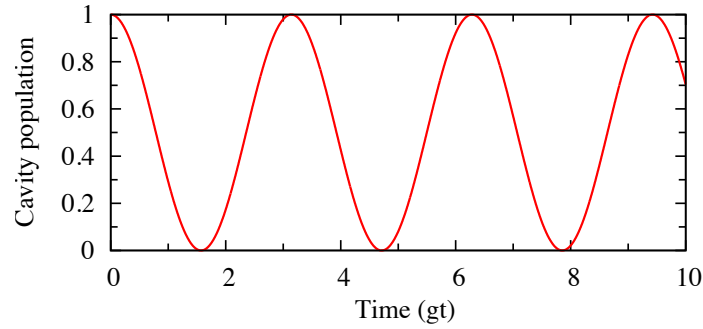


**Figure 5.3:** The cavity population which denotes the probability of single photon being in the cavity as the function of time.

[Fig. 5.2(a)]. Upon turning on the atom-cavity coupling the two states are split by  $2\hbar g$  on resonance.

The dynamics of the coupled atom-cavity system follows straightforwardly from this eigenstate structure. Starting from a fully occupied cavity, i.e. an initial state

$$|\psi(t=0)\rangle = |s, 1\rangle, \quad (5.7)$$

the resonant dynamics

$$|\psi(t)\rangle = \frac{1}{\sqrt{2}} (|+, 1\rangle + |- , 1\rangle e^{2igt}), \quad (5.8)$$

corresponds to simple Rabi oscillations with a frequency  $2g$ . This permits a complete quantum transfer between the cavity and the atomic excitation on a timescale  $\sim g^{-1}$

Thus one should place the atom as close as possible to the cavity surface in

order to speed up the transfer process while keeping surface-induced decoherence at a minimum. Decoherence due to electric and magnetic field noise close to metallic surfaces has been studied thoroughly for many decades. For instance, adatoms are shown to be the major cause of electrostatic fields in atom chip surfaces [60, 64]. Moreover, black-body (BB) radiation induces spontaneous transitions to other undesired states [153, 154], although this effect is greatly reduced at SC temperatures [155]. Finally, fluctuating electric and magnetic fields are also present in metallic components, such as the ones used in atom chips, ion trap electrodes, and coplanar MW cavities [156–159].

The detailed mechanism causing electric field noise close to metal surfaces is not completely understood. However, there is broad consensus that the resulting noise exhibits an inverse power-law dependence on the noise frequency [61, 159, 160]. In the following, we therefore present a brief discussion of such noise processes and their numerical generation.

## 5.2 1/f noise

Let us consider an electric field fluctuation  $\mathcal{F}(t)$  at the position of a Rydberg atom. Due to the different polarisability of the  $S$  and  $P$  Rydberg states ( $\alpha_S$  and  $\alpha_P$ , respectively) the transition under consideration will experience a differential Stark shift

$$\Delta E(t) = \frac{1}{2} |\alpha_S - \alpha_P| \mathcal{F}(t)^2. \quad (5.9)$$

$\mathcal{F}(t)$  resembles 1/f noise and a detailed generation of  $\mathcal{F}(t)$  is given in Ref. [161, 162]. This kind of noise is characterised by a power spectral density [ $S(\omega)$ ],

$$S(\omega) = \frac{1}{T} \int_{t=0}^{t \leq T} dt \langle g(0)g(t) \rangle e^{-i\omega_j t}, \quad (5.10)$$

where for the continuous notation it is given by

$$S(\omega) = S_0(d) / |\omega|^\kappa. \quad (5.11)$$

The noise amplitude  $S_0$  scales with the distance to the noise source  $d$  with a power law  $S_0 \propto d^{-\alpha}$ , with  $\alpha$  taking values of 1/4, 2, or 1 depending on the model and the distance itself, while  $\kappa$  takes values 1, 1/2 depending as well on the model and the frequency range considered [see [163] chapter 3].

In order to determine the noise amplitude and the scaling exponents we follow Ref. [61], and make use of the analytical model derived in Refs. [164, 165], where the dephasing rate of Ramsey and Hahn spin-echo experiments due to 1/f noise is obtained. In particular for noise producing a quadratic Stark shift and at long evolution times the coherence is found to decay as  $\exp(-\Gamma_f t/2)$  where the decoherence rate is defined as

$$\Gamma_f = \left( \frac{1}{2} \frac{\partial^2 \omega_{if}}{\partial \mathcal{F}^2} S_0 \right)^{1/\kappa}. \quad (5.12)$$

Here  $\frac{\partial^2 \omega_{if}}{\partial \mathcal{F}^2}$  is the polarisability difference between the two Rydberg states. For instance, in Ref. [163], where the states used are  $48S_{1/2} - 49S_{1/2}$ , one has  $\frac{\partial^2 \omega_{if}}{\partial \mathcal{F}^2} = 2\pi \times 600 \text{ Hz m}^2/\text{V}^2$ . From Ramsey/Hahn echo experiments,  $\Gamma_f$  can be experimentally determined and use the obtained value for estimating the noise amplitude  $S_0$  and the scaling law. The results obtained in [61], which use atom-chip surface distance of  $150 \mu\text{m}$ , give  $1/\Gamma_f = 5.3 \pm 2 \mu\text{s}$  which is consistent with values of  $20 (\text{V/m})^2 \leq S_0 \leq 40 (\text{V/m})^2$  for  $\kappa = 1$ . Thus, we assume from now  $\kappa = 1$ . Next, for the scaling with the surface distance we use the values obtained in Ref. [166] for copper surface (with a thin layer of oxide) which fit into a quartic dependence of the form

$$S(\omega, d) = \frac{S_0(d)}{\omega^\kappa} \equiv \frac{s_0}{d^4 \omega^\kappa}. \quad (5.13)$$

which is also consistent with the model of patch fields in Ref. [114]. From the data shown there we obtain  $s_0 \simeq 4 \times 10^{-17} (\text{Vm})^2$ , which at  $15 \mu\text{m}$  leads to  $S_0 = 790 (\text{V/m})^2$ .

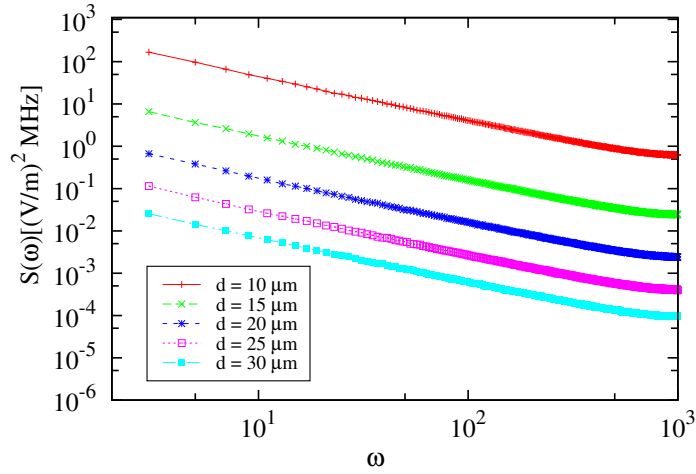
In order to simulate the  $1/f$  noise, we follow the procedure described in Ref. [161–163]. This consists of (i) Fourier transforming a Gaussian distributed white-noise signal, (ii) dividing the data by  $\omega^{1/2}$ , and (iii) inverse Fourier transforming back to time domain. Since the power spectral density (5.10) diverges at low frequencies, some cut-off must be considered. A natural cutoff is given by the integration time itself: when the signal is sampled the lowest frequency threshold is  $\omega_{ir} = 2\pi/T$ . For high frequencies there seems to be in general no strong dependence in where the cutoff is placed as the spectrum decays fast enough, and thus the largest frequency components do not play a role in the decoherence. For numerical simulations however, this cut off is imposed by the number of samples  $N$ , such that  $\omega_c = 2\pi N/T$ .

Fig. 5.4 shows the power spectral density as a function of angular frequency  $\omega$  for various distances  $d$  from the SC cavity surface in a log-log scale. As the Rydberg atom is placed away from the surface of cavity,  $S(\omega, d)$  decreases. This shows that the noise model can quantitatively describe the spectral density of noise when an atom is placed away from the surface. In the next subsection, we investigate atom-cavity coherence in the presence of  $1/f$  noise.

### 5.3 Noise effects on single-atom dynamics

We have shown that the presence of the field  $g$  induces the splitting between dressed states leading to the Rabi oscillations. We now investigate the presence of a local fluctuating  $1/f$  noise that causes the energetic shifts of dressed states [Fig. 5.6 (a)]. As an atom is placed  $d \mu\text{m}$  away from the surface of cavity, we use an approximation for the decay of the field





**Figure 5.4:** Power spectral density as the function of angular frequency for a principal quantum number  $n = 50$  and various distances between the cavity surface and the atom .

leaking out from the cavity [151], i.e.,

$$g(d) = g_0 e^{-d/x} \quad (5.14)$$

where  $g(0)$  is given in Eq. (5.2),  $d$  denotes the distance of atom-cavity surface and  $x = (s + w)/2$  [see Fig. 5.1]. Following experimental parameters from Ref. [167, 168], the electrode distance  $w \simeq 10 \mu\text{m}$  creates the effective cavity volume  $V_c \simeq 6.2 \times 10^{-12} \text{m}^3$ . Choosing  $m = 2$  yields  $\lambda_c = 2L/m \simeq 1 \text{cm}$ , and  $m + 1$  field antinodes. With effective dielectric constant  $\epsilon_c \simeq 6$ , the mode frequency is  $\simeq 2\pi \times 12 \text{GHz}$ . For  $s = 20$

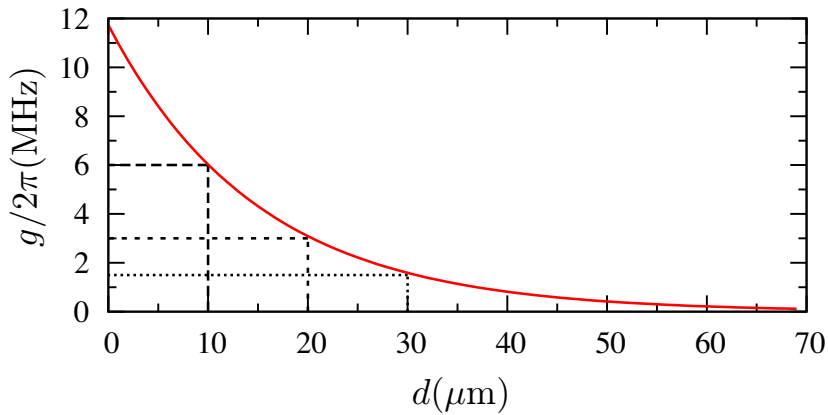


**Figure 5.5:** Atoms-cavity coupling as the function of atoms-cavity surface distance

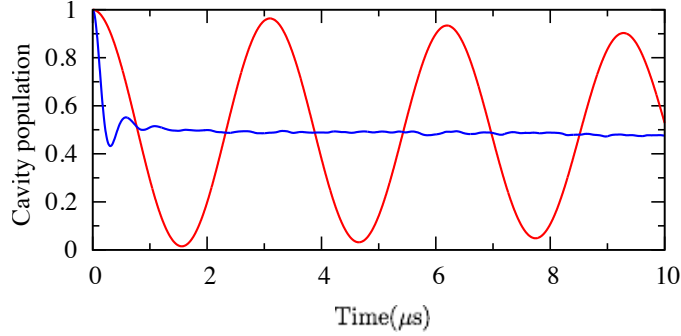


**Figure 5.6:** Cavity population as the function of time in the presence of noise for  $d \simeq 37.5 \mu\text{m}$  (red line) and  $d \simeq 15 \mu\text{m}$  (blue line) (see text for details).

$\mu\text{m}$  and  $w = 10 \simeq \mu\text{m}$  results  $x = 15 \mu\text{m}$  [54, 151]. The dipole matrix of neighbouring Rydberg states scales as  $\hat{\mu} \approx ea_0n^2$ . For  $n \simeq 50$  and  $d = 15 \mu\text{m}$ ,  $g/2\pi \simeq \times 4 \text{ MHz}$  [see Fig. 5.5], and spontaneous decays of the  $|s\rangle$  and  $|p\rangle$  state are  $\gamma_s \simeq 7 \text{ kHz}$  and  $\gamma_p \simeq 4 \text{ kHz}$ , respectively [70].

The dynamics of the system in the presence of fluctuating noise and spontaneous decay from the state  $|s\rangle$  can be simulated by means of stochastic Schrödinger equation (SSE). Since the decay rate of  $\gamma_s$  and  $\gamma_p$  is in kHz range, we can safely neglect it. A single realisation of the time dependent wave function evolves as

$$i|\dot{\psi}^{(k)}\rangle = \left[ \hat{H} + \varepsilon(t) \right] |\psi^{(k)}\rangle, \quad (5.15)$$

where  $\hat{H}$  is given in (5.1) and  $\varepsilon(t)$  denotes an energetic shift due to  $1/f$  phase noise. Starting from a fully occupied cavity, i.e., an initial state given in (5.7), for  $M$  realisations  $|\psi^{(k)}\rangle$ , we determine the cavity population and take its average

$$C_p = \frac{1}{M} \sum_{k=1}^M \langle (s, 1)^{(k)} | (s, 1)^{(k)} \rangle, \quad (5.16)$$

the resonant dynamics

$$|\psi(t)\rangle = \frac{1}{\sqrt{2}} \left( |+, 1\rangle + |-, 1\rangle e^{2i\varepsilon(t)} \right), \quad (5.17)$$

corresponds to incoherent oscillations due to an energetic shift  $\varepsilon(t) = E_{\pm,1} + \phi(t)$ , with  $\phi(t)$  being phase of fluctuating noise. Fig. 5.6 shows the dynamics of cavity population for an atom placed  $d \mu\text{m}$  away from the surface of cavity. We compare the cavity population for two different  $d$ :  $d \simeq 37.5 \mu\text{m}$  and  $d \simeq 15 \mu\text{m}$ . As  $d$  is close to the surface of SC cavity [60, 169], the coherence is completely destroyed, leading to  $C_p = 1/2$ .

---

We have shown that although the coupling is stronger due to the Rydberg states, their strong dipole polarisability causes an atom being prone to the surface noise. Therefore, we need another scheme that can compensate decoherence due to fluctuating noise from the surface of SC cavity. In the next section, we use of Rydberg lattice to overcome this problem. We will show that the presence of interactions in the Rydberg lattice, i.e., dipole-dipole interactions, can be employed to overcome inefficient interfacing between SC cavity and Rydberg atoms.



# Noise-resistant quantum interface

## Contents

---

<b>6.1 Noise effects on non-interacting ensembles</b> . . . . .	<b>58</b>
6.1.1 The Tavis-Cummings Model . . . . .	59
6.1.2 The Langevin equation . . . . .	61
<b>6.2 Effects of dipole-dipole interactions</b> . . . . .	<b>62</b>
<b>6.3 Effects of dissipative processes</b> . . . . .	<b>67</b>
<b>6.4 Transfer fidelities</b> . . . . .	<b>69</b>
<b>6.5 Robustness against <math>1/f</math> noise</b> . . . . .	<b>72</b>

---

In the previous chapter, we have shown the possibility to enhance the atom-cavity coupling by exploiting the large dipole moment of highly excited Rydberg states. However, the large polarisability ( $\propto n^7$ ) of Rydberg states also makes them more susceptible to spurious electric fields parasitising the metallic cavity surface. For a single atom coupled to SC cavity with typical atom-cavity distance [54, 55, 61, 169], the system indeed undergoes strong decoherence.

In this chapter, we propose a noise-resistant interface between a collection of Rydberg atoms and a single photon in a SC cavity by means of (resonant) dipole-dipole interactions (DDI). Instead very large atoms clouds ( $N \simeq 10^6$  atoms) [60], we use an atomic lattice with up to hundreds atoms. In such system, DDI are exploited to compensate dephasing of Rydberg states due to fluctuating electric field from the SC cavity surface. We show that this scenario is not only robust to the fluctuating noise from the cavity surface but also robust to the dissipative processes that originates from spontaneous emission from the state  $|ns\rangle$ .

This chapter is organised as follows. In Sec. 6.1, we will start with a simplest case : the interface between SC cavity and non-interacting atoms in the presence of noise.

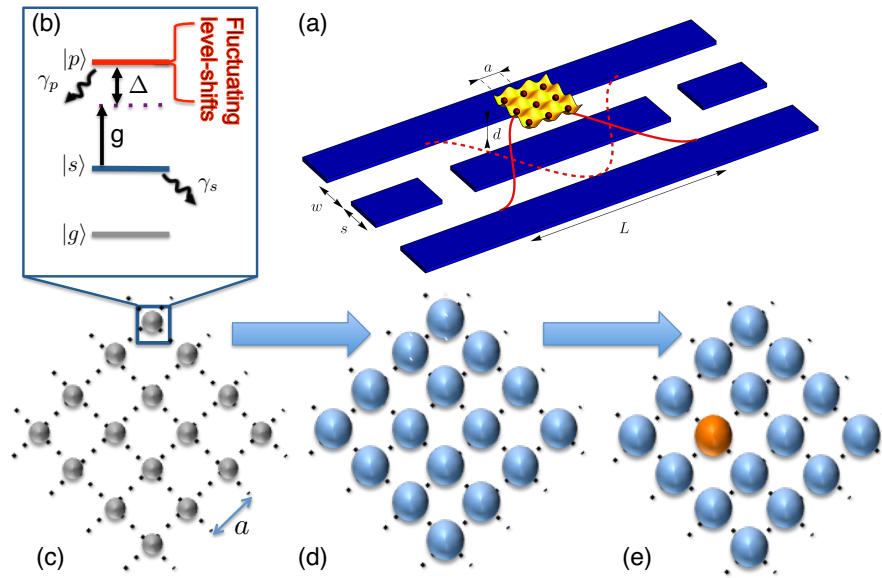


**Figure 6.1:** (a) Schematic picture of the Rydberg atom lattice coupled to a SC cavity via a single-MW photon. (b) Energy levels of a Rydberg atom. The atoms, initially in the ground state (c), are all pumped to the excited state  $|s\rangle$  (d) and (e) the cavity photon drives one of the atoms to state  $|p\rangle$ .

As the mechanism causing electric field noise to metal surface is not completely clear, we firstly use the type of noise described in chapter 3. Next, in Sec. 6.2, we include the DDI on Rydberg lattices. Here, we compare the noise-resistant coupling of Rydberg lattices and a SC cavity in the presence of DDI to the one in the absence of it. To ensure the geometrical dependence, we will discuss the comparison for a 1D lattice and a 2D lattice scenario. Next, in Sec. 6.3, we include the spontaneous decay from the state  $|ns\rangle$  and  $|np\rangle$  to investigate the effect of atom loss. In order to assure the performance of our system, we provide another figure of merit in Sec. 6.4. Finally, we discuss realistic parameters in Sec. 6.5, where  $1/f$  noise model is used instead of the type of noise described in chapter 3. We use two types of noise to ensure that our scenario is robust against two different types of noise.

## 6.1 Noise effects on non-interacting ensembles

This section is aim at presenting theoretical description of the interface between the non-interacting Rydberg atoms and SC cavity in the presence of fluctuating noise. We model atoms-cavity interactions by means of cavity quantum electrodynamics where the Hamiltonian that governs the system is typically described with Tavis-Cummings model.

### 6.1.1 The Tavis-Cummings Model

The interaction of Rydberg ensemble with a near-resonant microwave cavity can be described by the Tavis-Cummings model. As illustrated in Fig. 6.1 (a), we consider a square lattice of atoms, with site spacing  $a$  and one atom per site, held at a distance  $d$  from the surface of a coplanar superconducting-microwave cavity. All the atoms are initially pumped from the ground to the  $|s\rangle$  state [see Fig. 6.1(c) and (d)] and that the lattice spacing is large enough such that the second-order van der Waals interaction between atoms in  $|s\rangle$  states is negligible. This state is given by

$$|\phi_0\rangle = \left( \hat{a}^\dagger \prod_{i=1}^N \hat{\sigma}_{sg}^{(i)} \right) |\text{vac}\rangle \equiv \prod_{i=1}^N |s_i\rangle |1_c\rangle, \quad (6.1)$$

with  $\hat{\sigma}_{\alpha\beta}^{(i)} = |\alpha^{(i)}\rangle\langle\beta^{(i)}|$ . The operator  $\hat{a}^\dagger$  denotes creation of a single photon,  $|\text{vac}\rangle$  denotes the "vacuum state", i.e., the ground state of atoms with zero photon in the cavity ( $|\text{vac}\rangle = |g^{(i)}\rangle|0\rangle$ ), and  $|1_c\rangle$  denotes a single photon present in the cavity. The cavity photon collectively excites one of the atoms to the state  $|p\rangle$  [see Fig. 6.1 (d) and (e)], and the state is written as

$$|p_i\rangle = \hat{a} \hat{\sigma}_{ps}^{(i)} |\phi_0\rangle. \quad (6.2)$$

with  $\hat{a}$  denotes the annihilation operator of a single photon. We firstly consider the simplest case, i.e., in the absence of decay from state  $|s\rangle$  and the state  $|p\rangle$ . This implies that no atom loss to the ground state of atom (see Fig. 6.1 (b)), and hence the coherence process can be considered as an effective two-level system that consists of Eq. (6.1) and Eq. (6.2) as an effective ground and excited state, respectively. The Hamiltonian that governs the system is the Tavis-Cummings Hamiltonian which reads [126] :

$$\hat{H}_{ac} = \hbar g \sum_{i=1}^N \left( \hat{a} \hat{\sigma}_{ps}^{(i)} + \hat{a}^\dagger \hat{\sigma}_{sp}^{(i)} \right) + \hbar \Delta \sum_{i=1}^N \hat{\sigma}_{pp}^{(i)}. \quad (6.3)$$

For much of the present considerations, we set Planck's constant  $\hbar = 1$ . The first part of Hamiltonian denotes the atom-cavity coupling with a rate  $g\sqrt{N}$ , where  $N$  is the number of atoms in the lattice and  $g$  is given in Eq. (5.14). The second part of Hamiltonian (6.3) is a switchable detuning  $\Delta$  that can be switched on- and off-resonance by means of, e.g., external fields. The Rydberg states, in the absence of noise, have a bare energy separation  $\omega_{sp} \equiv \omega_p - \omega_s$  close to the cavity frequency such that initially  $\Delta \equiv \omega_{sp} - \omega_c \simeq 0$ . This energy separation is affected by external spurious electric fields due to the polarisability difference between the two Rydberg states, as we will describe later. We have assumed a typical decay length of the evanescent field on the order of the gap width [54, 151] and that all the atoms experience the same coupling strength to the cavity.

We determine the quantum dynamics of Hamiltonian (6.3) by means of Schrödinger equation. For a single realisation, we calculate the cavity population,

$$C_p = \langle \phi_0 | \phi_0 \rangle. \quad (6.4)$$

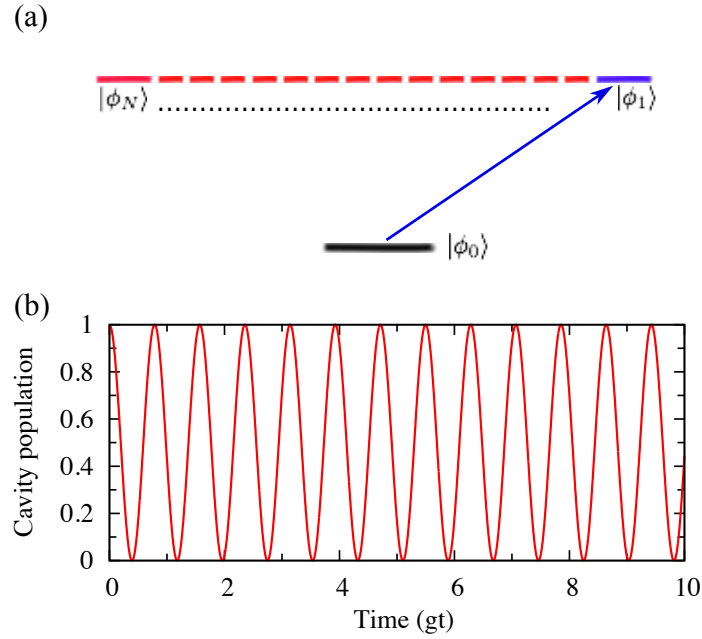


**Figure 6.2:** Panel (a) shows schematic of coupling between single photon state and the collective states of single-atom excitation. The blue and red lines denote symmetric and non-symmetric states, respectively. (b) shows the population of single photon in the cavity as the function of time for  $N = 16$ .

As shown Fig. 6.2, Rabi oscillation occurs due to the coupling to the symmetric state [see Fig. 6.2 (a)]. For  $N$  atoms, the symmetric state is written as

$$|\phi_1\rangle = \frac{1}{\sqrt{N}} \sum_{i=1}^N |p_i\rangle. \quad (6.5)$$

As the number of non-interacting atoms increases, the coupling strength increases  $\sim \sqrt{N}g$ , producing faster oscillation than a fewer atom case [see Fig. 6.2 (b)] [126]. The coupling strength between the atomic ensemble and the cavity field  $g_N$  can be defined as the matrix element of the first part in Hamiltonian 6.3. This matrix elements read

$$g_N = g \sum_{j=1}^N \sum_{i=1}^N \langle \phi_0 | \hat{a} \hat{\sigma}_{ps}^{(i)} + \hat{a}^\dagger \hat{\sigma}_{sp}^{(i)} | \phi_j \rangle = \sqrt{N}g, \quad (6.6)$$

where  $|\phi_j\rangle$  denotes collective states which read

$$|\phi_j\rangle = \sum_{i=1}^N c_j^{(i)} |p_i\rangle, \quad (6.7)$$

with  $c_j^{(i)} = \pm 1/\sqrt{N}$  and  $j$  denotes the state indices.



For the simplest case, we have shown that the increased number of atoms leads to the increase of atom-cavity coupling strength  $\sim \sqrt{N}$ . In the next subsection, we include the presence of noise and discuss its consequences.

### 6.1.2 The Langevin equation

In this subsection, we study the quantum dynamics of SC cavity coupled to non-interacting atoms in the presence of noise. The presence of noise causes the energetic shift  $\varepsilon^{(i)}(t)$  of Rydberg states that leads to decoherence. The Hamiltonian of noise is given by

$$\hat{H}_{tn} = \sum_i^N \varepsilon^{(i)}(t) \hat{\sigma}_{pp}^{(i)} \quad (6.8)$$

with  $\hat{\sigma}_{pp}$  denotes the projection operator to the state  $|p\rangle$ . Here the noise acts locally, i.e.,  $\langle \varepsilon_i \varepsilon_j \rangle = C \delta_{ij}$ . Although the most typical type of noise for SC cavity is  $1/f$  noise [60, 66, 149, 170–172] (see Subsec. 5.2), in this subsection we firstly discuss the laser phase noise [173, 174] that has been described in Sec. 3.2. To remind the math symbols, we rewrite the Langevin equation as in Sec. 3.2

$$\dot{\varepsilon} = -\gamma \varepsilon + F(t), \quad (6.9)$$

where fluctuations of energetic shift  $\varepsilon(t)$  acts as time-dependent detuning in which the correlation time  $\tau_c = 1/\gamma$ . The Gaussian white noise  $F(t)$  denotes a rapidly fluctuating force with zero ensemble average  $\overline{F(t)} = 0$  and  $\overline{F(t_1)F(t_2)} = 2D\delta(t_2 - t_1)$  with  $D$  describes the magnitude of fluctuating forces and  $\delta(t_2 - t_1)$  is Dirac delta function. Here  $D$  and  $\gamma$  characterises the spectral width  $\Gamma$  of Lorentzian line shape [173]

$$\Gamma = \frac{2D}{\gamma^2} \quad (6.10)$$

The dynamics of this system is described by the Langevin equation in which a single realisation  $k$  of the time dependent wave function evolves as  $i|\dot{\psi}^{(k)}\rangle = \hat{H}|\psi^{(k)}\rangle$ . For  $M$  realisations  $|\psi^{(k)}\rangle$  of the trajectories over  $N$  atoms, we calculate a cavity population

$$C_p = \frac{1}{M} \sum_{k=1}^M \langle \phi_0^{(k)} | \phi_0^{(k)} \rangle. \quad (6.11)$$

For sufficiently large  $M$ , the average of  $C_p$  (cavity population) converges. Fig. 6.3 shows the comparison of quantum dynamics in the absence and the presence of noise. In the absence of fluctuating noise Rabi oscillations occur perfectly between the atoms and the cavity. However, in the presence of fluctuating noise, Rabi oscillations decrease exponentially, exhibiting decoherence of quantum dynamics. This can be understood as follows: In the absence of the noise, the effective ground state  $|\phi_0\rangle$  couples to the symmetric state but

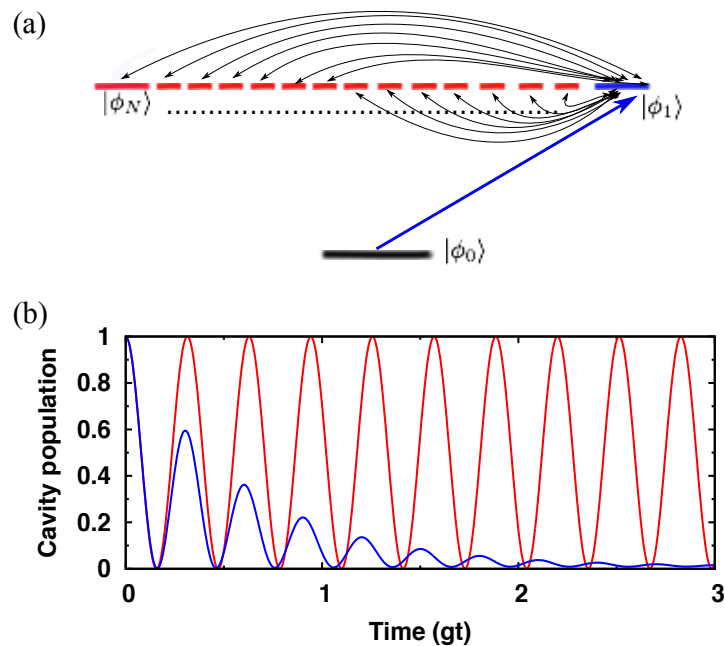


**Figure 6.3:** Panel (a) shows schematic of coupling between single photon state and the collective states of single-atom excitation. The blue and red lines denote symmetric and non-symmetric states, respectively and the curved arrows show the population transfer between a symmetric states and non-symmetric states. (b) shows the cavity population as the function of time for  $N = 100$  in the absence of noise (red line) and the presence of noise (blue line) for  $\Gamma = 5g$  and  $\gamma = 14g$ .

uncouples to the non-symmetric states [see Fig. 6.3(a)]. The non-symmetric states read

$$|\phi_{j>1}\rangle = \sum_{i=1}^N c_j^{(i)} |p_i\rangle. \quad (6.12)$$

When the noise is present, the population transfer occurs from a symmetric state into non-symmetric states, leading to a damping of Rabi oscillations [see Fig. 6.3(b)].

We have shown that the presence of noise causes the coupling between a symmetric and non-symmetric states, leading to the damping of Rabi oscillations. To this section, we have not included the presence of DDI. In the next section, we investigate a noise-resistant interface between a collection of Rydberg atoms and a single photon in a SC cavity (see Fig. 6.1) by means of (resonant) DDI.

## 6.2 Effects of dipole-dipole interactions

Strong DDI occurs between Rydberg states with similar principal quantum number but different angular momentum. It has been shown to yield coherence population exchange between different atoms [53]. Most previous works dealing with Rydberg atoms driven

by a microwave-cavity photon had considered the cloud of atom with a single Rydberg atom [51, 52, 54, 55, 60, 61], and hence the exchange interaction has not been effectively exploited so far. In addition, our numerical simulations in Sec. 5.3 and Subsec. 6.1.2 show that for both a single atom and non-interacting atoms which couple to the SC microwave cavity, the system undergoes strong decoherence. Therefore, in this section we investigate the role of DDI in compensating decoherence due to fluctuating noise from the surface of SC cavity. We also identify the advantages of the combination between SC cavity and the ensemble of atoms placed for two-different geometrical lattices.

As described in Sec. 6.1, we consider a two-dimensional lattice where all the atoms are initially pumped to a particular Rydberg state. Consequently, the cavity photon can excite one of the atoms to a different angular momentum Rydberg state, which in turn is coupled to all the nearby atoms via DDI. In this situation, the typical Hamiltonian which describes the DDI is given by

$$\hat{H}_{dd} = \hbar V_0/2 \sum_{i,j \neq i} \frac{\hat{\sigma}_{ps}^{(i)} \hat{\sigma}_{sp}^{(j)}}{|\mathbf{r}_i - \mathbf{r}_j|^3} \quad (6.13)$$

with the operators denote the exchange state  $|s\rangle$  and  $|p\rangle$  between an atom  $i$  and an atom  $j$ . A pair of excited atoms at site  $i$  and  $j$  experiences the DDI  $V_0/|\mathbf{r}_i - \mathbf{r}_j|^3$  with  $V_0 = C_3/a^3$ . For a one dimensional lattice,  $\mathbf{r}_i$  and  $\mathbf{r}_j$  is simply  $i$  and  $j$ , in which  $V_0/|i - j|^3$ . For a two dimensional lattice, two atoms located at site  $\mathbf{r}_i = (x_i, y_i)$ ,  $x_i, y_i \in [1, L]$  and  $\mathbf{r}_j$  ( $i \neq j$ ) are separated by a distance  $|\mathbf{r}_i - \mathbf{r}_j|$ .

We now consider the dynamics of system in the presence of fluctuating noise and DDI. The total Hamiltonian that governs the system consists of atom-cavity interaction in Eq. (6.3), fluctuating noise in Eq. (6.8) and DDI in Eq. (6.13). It reads

$$\hat{H}_{tot} = \hat{H}_{at} + \hat{H}_{ln} + \hat{H}_{dd}. \quad (6.14)$$

We simulate trajectories of Eq. (6.14) with the same procedure as in subsec 6.1.2. We subsequently compare the cavity population in the presence of DDI for 2D lattice to the case of non-interacting atoms in the presence of noise.

In the previous section we mention that the presence of fluctuating noise leads to the damping of Rabi oscillations and the lost of coherence. The coherence lost, however, can be overcome by means of DDI. As shown in Fig. 6.4 (a), the DDI causes the energetic shift of collective states, preventing the population transfer from the symmetric state into non-symmetric states. As the energies of the non-symmetric states are well separated from the symmetric state, the atomic frequencies are now far off resonance from the single cavity mode. Therefore,  $\omega_c$  must be chosen differently to compensate the corresponding energetic shift such that the atomic and cavity frequencies are in resonance. In order to determine  $\omega_c$ , we will later choose the value for  $\omega_c$  which equals to the eigenenergy of the symmetric state. Therefore, we perform diagonalisation of Eq. (6.13) to obtain the eigenenergies and eigenstates of collective states. For the case of many atoms and resonant

driving, the collective states read

$$|\varphi_j\rangle = \sum_{i=1} w_j^{(i)} |b_i\rangle \quad (6.15)$$

where  $w_j^{(i)} = \pm 1/\sqrt{N}$  for  $j$  denotes the state indices and  $j \in [1, N]$ . Here  $|b_i\rangle$  is similar to  $|p_i\rangle$ , but in the absence of a single photon state. Its basis is given by

$$|b_i\rangle = \hat{\sigma}_{ps}^{(i)} |\varphi_0\rangle, \quad (6.16)$$

for which  $|\varphi_0\rangle = \prod_{i=1} |s^{(i)}\rangle$ . The coupling strength of collective states of atoms can be defined as the matrix element given by

$$\tilde{G}^{(j)} = g \sum_{i=1}^N \langle \varphi_0 | \hat{\sigma}_{ps}^{(i)} + \hat{\sigma}_{sp}^{(i)} | \varphi_j \rangle, \quad (6.17)$$

where the total collective coupling is given by,

$$\tilde{G}(E) = \frac{1}{N} \sum_{j=1}^N |\tilde{G}^{(j)}|^2 \delta_{E, E_j}, \quad (6.18)$$

with  $\delta_{E, E_j}$  is a kronecker delta and  $E_j$  are eigen energies of the collective states. The numerical results of Eq. (6.18) is depicted in Fig. 6.4 (b), showing the probability of collective coupling  $\tilde{G}(E)$  as a function of collective-state energy ( $E$ ). We define  $\Delta E$ , denoting the energy separation between the eigenenergy of addressed symmetric state  $E_1$  and the closest non-symmetric state energy  $E_2$ . It is given by

$$\Delta E = |E_1 - E_2|, \quad (6.19)$$

[see also Fig. 6.4 (b)]. We now choose the value of  $\omega_c$  determined from the eigenenergy of addressed symmetric state. Switching  $\omega_c$  to it indeed restore the coherent oscillation between the microwave cavity and the atoms. This is depicted in Fig. 6.4 (c), showing the effect of the protection mechanism by plotting the cavity population as a function of time in the presence (dashed line) and absence (solid line), e.g., large lattice spacing, of interactions. In the absence of interactions, the coupling between the state  $|\phi_0\rangle$  and  $|\phi_1\rangle$  leads to Rabi oscillations of the cavity population at a frequency  $g\sqrt{N}$  [175], damped due to the dephasing induced by the local noise fluctuations. This damping is of the form  $\exp[-t/\tau_{coh}]$  with  $\tau_{coh} \simeq 0.2 g^{-1}$ . In comparison, the case where the DDI is present exhibits 25 times longer coherence time  $\tau_{coh} \simeq 5 g^{-1}$ .

We should note that the eigenstates in Eq. (6.15) do not necessarily coincide in general with the collective basis  $|\phi_j\rangle$  introduced in Eq. (6.7). So in practice, even after readjusting the detuning to compensate the shift of the addressed symmetric state, its resonant coupling to the cavity will not be perfect and the cavity will partially couple to other non-symmetric state. Nevertheless, tuning the system on resonance to the peak with the largest  $\tilde{G}$ , i.e.,  $E \simeq 87.58g$  in the Fig. 6.4 (b), guarantees that the coupling to

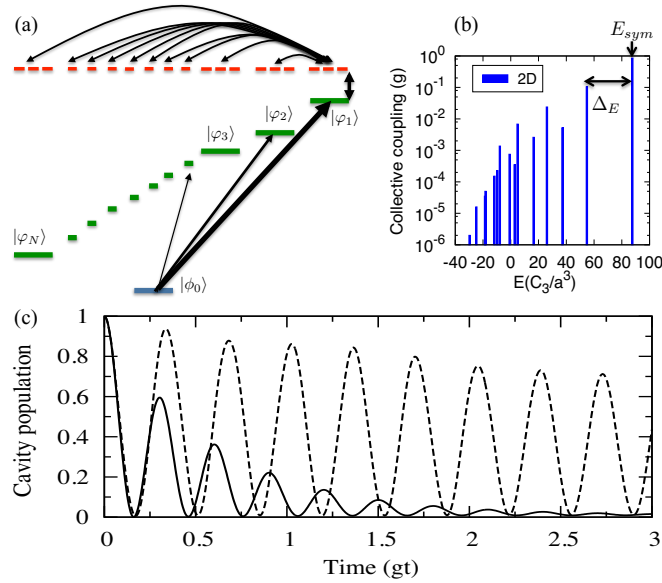


**Figure 6.4:** Panel (a) shows the scheme of coupling between microwave photon in SC cavity with an effective collective states of  $10 \times 10$  atoms. The collective states in the absence of interactions are denoted by red lines while in the presence of interactions are denoted by green lines. The thickness of arrow line corresponds to the strength of coupling to the collective states. Panel (b) shows the probability of the collective states as the function of their eigenenergies. The highest peak corresponds to the eigenenergy of addressed symmetric state  $E_{sym} = E_1$  while others correspond to the coupling of non-symmetric states. The energy separation between  $E_1$  and the adjacent non-symmetric state  $E_2$  is denoted by  $\Delta_E$ . Panel (c) shows Rabi oscillation between SC cavity and the ensemble of  $10 \times 10$  atoms for  $\Gamma = 5g$ ,  $\gamma = 14g$ ,  $V_0 = 25g$ ,  $\Delta = -87.58g$  and  $\gamma_s = 0$  in the absence of interactions (black line) and the presence of interactions (black dashed) obtained from  $10^3$  realisations of a single trajectory calculated by Langevin equation.

other non-symmetric states will still be weak as long as  $\Delta_E$  is larger than both  $g\sqrt{N}$  and the noise strength ( $\Gamma$ ).

We finally identify the advantages of the coherence of atom-cavity coupling for the case of 2D lattice. We compare the case of 2D lattice to 1D lattice scenario. As shown in Fig. 6.5, the lattice geometries indeed determine the coherence lifetime. The cavity population for a 2D lattice exponentially decreases slower ( $\tau_{coh} \simeq 5 g^{-1}$ ) than 1D lattice case ( $\tau_{coh} \simeq 0.6 g^{-1}$ ). In comparison, the coherence lifetime of 2D lattice case is 8 times longer than 1D lattice case. This can be understood from Fig. 6.6 (a) and (b), showing the coupling of collective states  $\tilde{G}(E)$  as the function of eigen energies for two different dimensional lattices.

For 1D lattice [see Fig. 6.6 (a)], the energy separation  $\Delta_E$  is much smaller than 2D lattice [see Fig. 6.6 (b)]. Therefore, for 1D lattice, although the presence of DDI, the population transfer easily occurs from the symmetric state to non-symmetric states due to  $\Gamma \sim \Delta_E$ . In contrary to 1D lattice, 2D lattice exhibits large energy separation such that  $\Delta_E \gg \Gamma$ . We should note that the energy of addressed symmetric state for 1D lattice saturates faster than 2D as the increase of atom number [see Fig. 6.6 (c)]. As the increase of atom number, the discrete energy becomes densely packed which is shown by the sat-

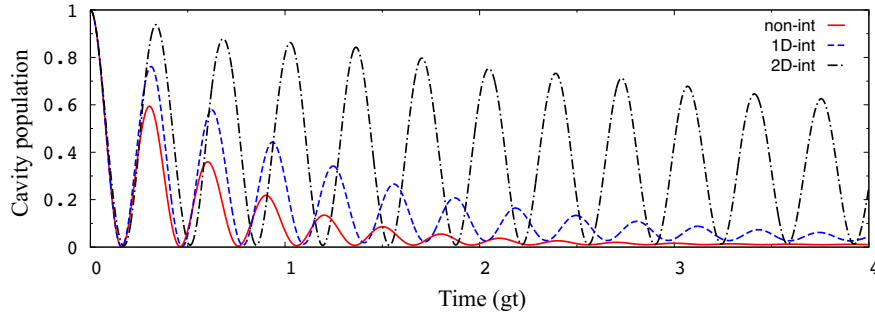


**Figure 6.5:** Cavity population as the function of time for  $\Gamma = 5g$ ,  $\gamma = 14g$ ,  $N = 10 \times 10$ , and  $V_0 = 25g$ . Red line shows the coherence for the case of non-interacting atoms while blue and black dashed show the coherence of atomic ensembles placed in 1D lattice and 2D lattice, respectively.

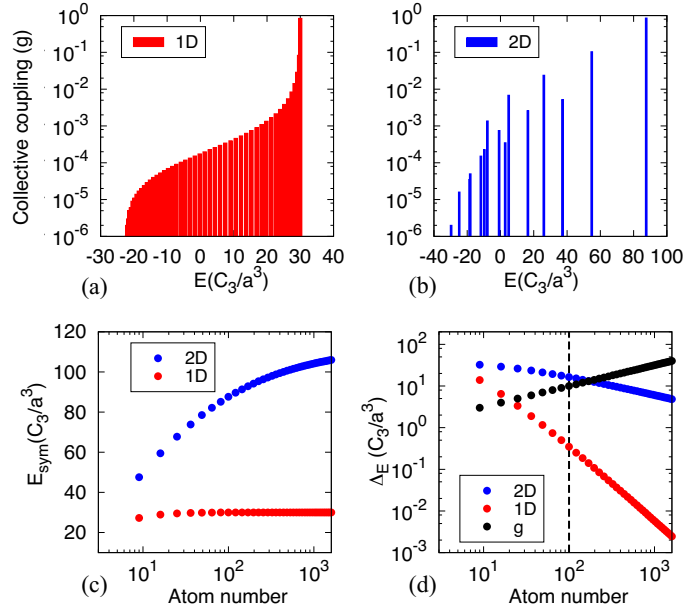


**Figure 6.6:** Collective coupling of atoms as the function of eigen energies for for (a) 1D lattice and (b) 2D lattice. The energy of symmetric state and  $\Delta_E$  as the function of atom number is shown in (c) and (d), respectively. The rest parameters are  $N = 100$  and  $V_0 = 25g$ . The vertical black dashed for  $N = 100$  will correspond to the explanation in Fig. 6.10 (d).

uration of energy of symmetric state and the decrease of  $\Delta_E$  for the case of 1D and 2D [see Fig. 6.6 (d)]. Consequently, as the atom number increases, the addressed symmetric state is likely to couple to the non-symmetric states. On the other hand, the atom-cavity coupling increases as the atom number increases. The interplay between  $g$ ,  $\Delta_E$  and  $E_{sym}$  significantly influences the coherence lifetime of the system. The consequences of this interplay will be discussed later.

To this section, we have not considered another source of decoherence which originates from atoms. In this case black body radiation induces spontaneous transitions

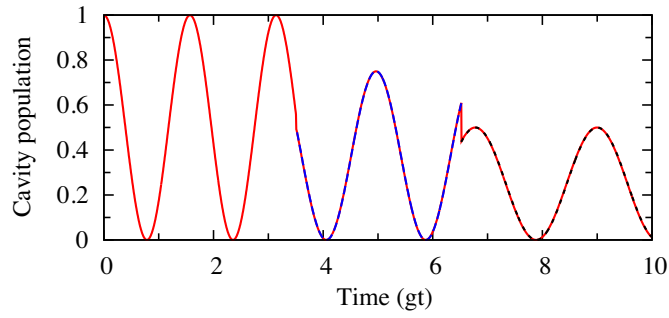


**Figure 6.7:** A single trajectory of cavity population as the function of time for  $\gamma_s = 0.1g$ ,  $\gamma_p = 0$ , and  $N = 4$ . The dashed shows the agreement with the cavity population for  $N = 3$  (blue dashed) and  $N = 2$  (black dots) in the absence of decay.

to other undesired states [55, 153], although this effect is greatly reduced at SC temperatures [155]. In the next section, we will study the dynamics of system in the presence decoherence due the spontaneous decays from the state  $|s\rangle$  and  $|p\rangle$  [see Fig. 6.1 (b)], instead of noise.

## 6.3 Effects of dissipative processes

In this section, we consider the presence of spontaneous decays from state  $|s\rangle$  and state  $|p\rangle$  with the rate  $\gamma_s$  and  $\gamma_p$  [see Fig. 6.1 (b)], respectively. We simulate the dynamics of the system by means of quantum jump algorithm [see appendix B.1 and [115–118]]. It requires more efforts to perform this numerical calculation, as we need to add more basis than the case of the absence of decays. The additional basis is needed due to the atom loss from the state  $|s\rangle$  or  $|p\rangle$  to the ground state  $|g\rangle$  of atom. Thus, this is similar to considering three-level ladder system without the presence of driving force between the state  $|g\rangle$  and state  $|s\rangle$ .

When an atom loss occurs from the state  $|s\rangle$ , the basis  $|\phi_0\rangle$  also changes into new basis state which reads

$$|G^{(j)}\rangle = \hat{\sigma}_{gs}^{(j)} \left[ \left( \hat{a}^\dagger \prod_{i \neq j} \hat{\sigma}_{sg}^{(i)} \right) |g^{(i)}\rangle |0\rangle \right], \quad (6.20)$$

where the microwave cavity still couples to the state  $|B_i\rangle$  but with less coupling strength which is given by

$$|B_i\rangle = \hat{a} \hat{\sigma}_{ps}^{(i)} |G^{(j)}\rangle \quad (6.21)$$

As a test, we simulate a single trajectory for  $\gamma_s = 0.1g$  and  $\gamma_p = 0.0g$  in the absence of DDI for  $N = 4$ . We will show that the atom loss leads to the decrease of amplitude and frequency, as it equals to  $g\sqrt{N}$ . For a single trajectory  $|\psi^{(1)}\rangle$  with  $N$  atoms, we calculate a

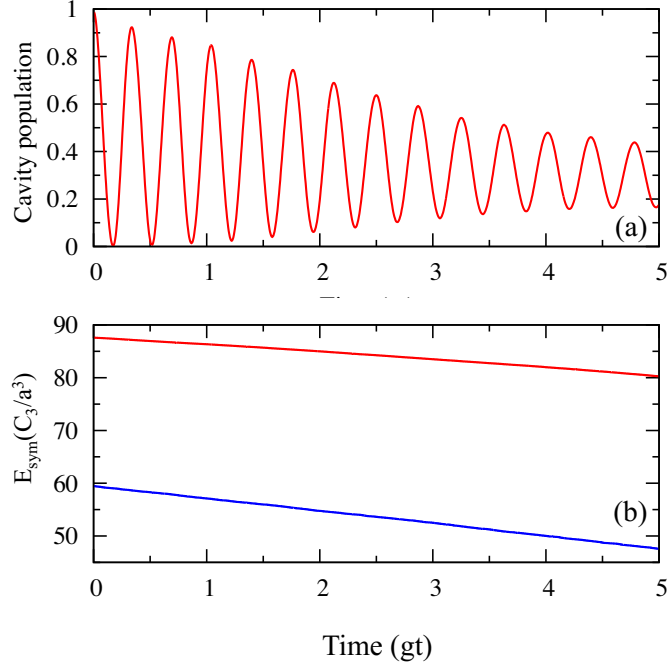


**Figure 6.8:** Panel (a) shows the dynamics of cavity population for  $N = 10 \times 10$  and (b) shows the shift of symmetric state energy for  $N = 10 \times 10$  (red line) and for  $N = 4 \times 4$  (blue line) as the function of time. The simulations were performed for  $M = 10^3$  and the rest parameters are  $\gamma_s = 0.1g$ ,  $\gamma_p = 0.1g$ ,  $\Gamma = 0$ , and  $V_0 = 25g$ .

cavity population similar to Eq. (6.11). Fig. 6.7 shows a single trajectory of non-interacting atoms in the absence of interactions (see caption) with the initial state reads  $|\phi_0\rangle$ . When the first atom loss occurs from state  $|s\rangle$  to state  $|g\rangle$ , the oscillation frequency changes from  $2g$  to the  $\sqrt{3}g$  ( $N = 4 \rightarrow N = 3$ ), accompanied by the decrease of amplitude due the loss of an atom. We perform another single trajectory for  $N = 3$ , yet in the absence of decay, to confirm the decrease of frequency. The blue dashed ( $N = 3$ ) is in agreement with the change of frequency after first atom loss, confirming the change of frequency and amplitude. For the second check, the black dots ( $N = 2$ ) also in agreement with the change of frequency after second atom loss.

We now simulate  $M$  realisations of trajectories for  $N = 10 \times 10$  in the presence of DDI and compare it to the case of  $N = 4 \times 4$  (see caption in Fig. 6.8 for detail). Technically, performing numerical simulations for this larger systems increase the dimension of Hilbert space which leads to the high time-consuming of calculations. Fortunately, since the absence of driving force between the state  $|s\rangle$  and  $|g\rangle$ , we can perform truncations of unpopulated states. The detail of truncations is given in Appendix D.

Fig. 6.8 shows the average of cavity population (a) and the shift of eigenenergy of symmetric state (b) as a function of time for  $N = 10 \times 10$  (red line),  $N = 4 \times 4$  (blue line), and  $M = 10^3$  (see caption for details). We observe the decrease of cavity population due to the change of amplitude and frequency during the decay processes [see Fig. 6.8 (a)]. The damping of oscillation is accompanied with the shift of eigenenergy of



addressed symmetric state off resonance with the cavity frequency [see Fig. 6.8 (b)]. For this time window, the atom loss from the state  $|s\rangle$  with rate  $\gamma_s = 0.1g$  yields  $\sim 40\%$  atom loss. Despite that loss, the coherence persists. This is due to the fact that for the large number of atoms, e.g.,  $N > 16$ , the shift of energy is smaller than the case of  $N \leq 16$ . Fig. 6.8 (b) shows the comparison the shift of eigenenergy of addressed symmetric state for  $N = 10 \times 10$  and  $N = 4 \times 4$ . We observe that with 40% atom loss,  $N = 10 \times 10$  produces smaller shift than the case of  $N = 4 \times 4$ .

We have shown that the system for large number of atoms produces relatively small shift of eigenenergy of addressed symmetric state. Despite the presence of atom loss, the system is sufficiently robust for the large number of atoms. Although  $\tau_{coh}$  in the previous section already provides a figure of merit to assess the performance of our system, we are interested in the transfer of the photon from the cavity to the atoms, and after a certain period of time back to the cavity. In the next section, we study the efficiency of the retrieval process as a function of the storage time in the presence of decoherence not only due to the presence of spontaneous decays but also due the presence of noise.

## 6.4 Transfer fidelities

This section is aim at investigating the efficiency of retrieval process in the presence of decoherence due to fluctuating noise and spontaneous decays. In practice this can be realised by switching the detuning off-resonance at half of a Rabi oscillation [see Fig. 6.9(a)]. After a time interval  $T_{stor}$  the atom-cavity system can be tuned on-resonance again and wait until the cavity population reaches its maximum, i.e., the retrieval efficiency  $\eta$ . This process can be performed for several realisations varying the storage time  $T_{stor}$  [see different curves in Fig. 6.9(a)]. The ability to store the photon in the Rydberg transition for a long  $T_{stor}$  is important since ideally during the storage stage one would temporarily transfer all the excited atoms to hyperfine ground states, where the lifetime can be further extended and the noise is less harmful. The longer the time window to perform this transfer process, the more efficiently can be done by means of, e.g., adiabatic population-transfer techniques.

By plotting the retrieval efficiency as a function of the storage time [Fig. 6.9(b)] we compare the performance of our protocol for interacting and non-interacting atoms. We note that the storage lifetime, denoted as  $\tau_{stor}$ , in the absence of interaction is  $\tau_{stor} \simeq 0.2g^{-1}$  and the presence of DDI is  $\tau_{stor} \simeq 4.6g^{-1}$ . This shows that  $\tau_{stor}$  in the presence of DDI is 23 times longer than in the absence of interactions for the chosen parameters. We observe that the slow decrease of the efficiency for the interacting case is accompanied by small oscillations. We attribute those not only to an imperfect resonant coupling to the symmetric state, but also weak driving of nearby non-symmetric states [see Fig. 6.4(b)].

The maximum retrieval ( $\eta_0$ ) and storage lifetime ( $\tau_{stor}$ ) can be further improved by increasing the interaction strength. This is shown in Fig. 6.10 (a) and (c), respectively.

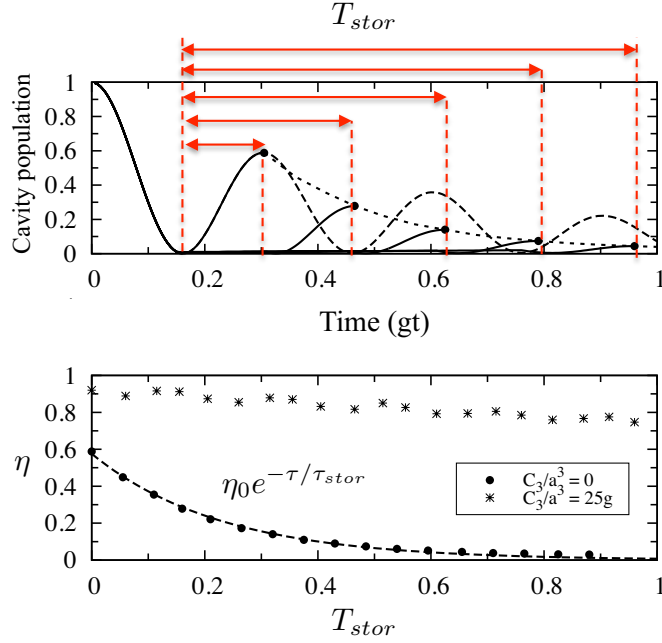


**Figure 6.9:** Panel (a) shows the storing and retrieving of microwave photon in the absence of interaction, but in the presence of noise for  $\gamma_s = 0.01g$ ,  $\gamma_p = 0.01g$ ,  $\Gamma = 5g$  and  $\gamma = 14g$ . Panel (b) shows the comparison between the lifetime of cavity population in the presence (cross) and the absence of interactions (dot).

The maximum retrieval  $\eta_0$  in the presence of spontaneous decay  $\gamma_s = \gamma_p = 0.01g$  is equal to the case of the absence of spontaneous decay [see Fig. 6.10(a)]. This is due to the fact that only a few percent of atom loss occurs after a single Rabi oscillation. Fig. 6.10 (c) shows the  $\tau_{stor}$  as the function of the interaction strength. As the interaction strength increases, the  $\tau_{stor}$  for both cases show quadratically increase. The quadratic growth of storage lifetime is associated with the geometry of the lattice, i.e., a two-dimensional lattice. In the case of a one-dimensional lattice, the growth is linear. The increase of  $\tau_{stor}$  for both cases is equal for  $C_3/a^3 < 25g$  and differ for  $C_3/a^3 \geq 25g$ . The difference can be understood as follows: for  $C_3/a^3 \geq 25$ , although produces larger  $\Delta_E$  compared to  $\Delta_E$  for  $C_3/a^3 < 25$ , the atom loss yields the large energetic shift of collective states. Consequently, during the process of atom loss the energetic shift of collective states leads the system to more far-off resonant than the case of  $C_3/a^3 < 25$ , and hence the  $\tau_{stor}$  is shorter than the one in the absence of spontaneous decay.

Finally, we also analyse the maximum retrieval efficiency  $\eta_0$  and the storage lifetime  $\tau_{stor}$  as a function of the number of atoms in the systems [see Fig. 6.10 (b) and (d), respectively]. In these figure, we not only compare the 2D lattice case in the presence (crosses) and the absence (triangles) of decays, but also compare them to the case of 1D lattice (squares) and non-interacting atoms (stars). In Fig. 6.10 (b), we observe that for the non-interacting case the cavity population after a single Rabi oscillation  $\eta_0$  increases as we include more atoms in the system. This is due to the enhancement of the collective coupling factor  $\sqrt{N}$  which reduces the time in which the noise acts on the atoms during the first oscillation. Note that at this timescales ( $1/g\sqrt{N}$ ) the spontaneous decay does not

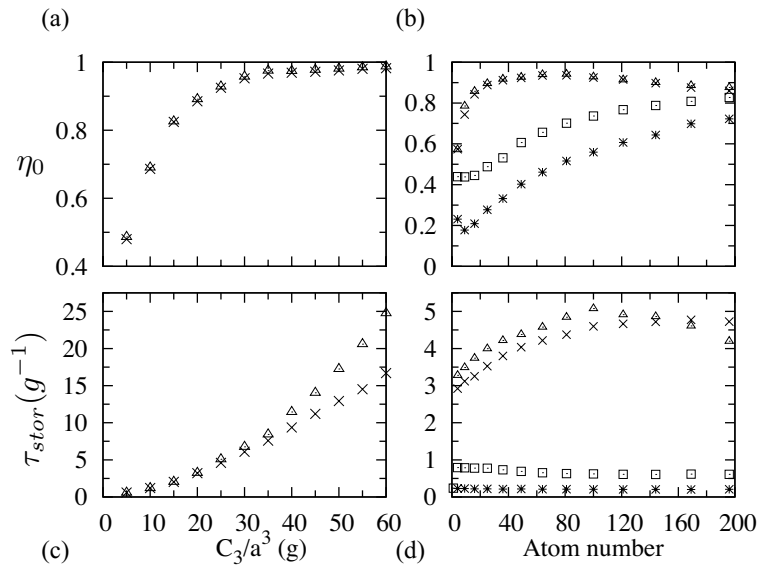


**Figure 6.10:** Panel (a) and (c) shows the maximum retrieval  $\eta_0$  and the storage lifetime  $\tau_{stor}$  as the function of interaction strength in the absence (triangles)  $\gamma_s = 0$  and the presence of spontaneous decay (crosses)  $\gamma_s = 0.01g$ ,  $\gamma_p = 0.01g$  for a 2D case. (b) and (d) shows of  $\eta_0$  and  $\tau_{stor}$  as the function of atom number in the absence (stars) and the presence of interactions (1D-squares, 2D-triangles) for  $V_0 = 25g$ . The rest of parameters are  $\Gamma = 5g$  and  $\gamma = 14g$

play a significant role.

In comparison, we observe that  $\eta_0$  is larger for interacting case. For 1D lattice case,  $\eta_0$  increases as the atom number increases. For 2D lattice case, we observe that  $\eta_0$  increases for small-intermediate atom numbers and decreases for large atom number. The decrease can be understood as follows: as we have seen in Fig. 6.6 (d) if an excessively large number of atoms is considered, the energy gap between the different collective states becomes smaller than the coupling strength. Thus the cavity can be strongly coupled to many of them, introducing an additional dephasing mechanism besides the noise <sup>†</sup>.

Fig. 6.10 (d) shows the storage lifetime  $\tau_{stor}$  of the excitation stored in the atoms. For 1D lattice, although the increase of the atom number increases  $\eta_0$ , its  $\tau_{stor}$  shows less efficient retrieval process [see Fig. 6.10 (d)] compared to 2D lattice case. The inefficient retrieval process for 1D lattice can be understood as follows: despite the larger the size of the lattice, the energy separation of symmetric state to the closest non-symmetric state  $\Delta_{E_{1D}} \sim \Gamma \ll \Delta_{E_{2D}}$  [see Fig. 6.6 (d)]. Consequently, the presence of DDI in 1D lattice case is insufficient to strongly compensate decoherence due to fluctuating noise. In contrast to 1D case, 2D lattice case exhibits  $\Delta_{E_{2D}} \gg \Gamma \gg g\sqrt{N}$  [see Fig. 6.6 (d)], and hence the presence of DDI in 2D lattice case is sufficient to strongly compensate decoherence.

We now compare the case of the presence and the absence of decays. As shown

<sup>†</sup> Atom loss can also play a role since the more atoms we prepare in the  $|s\rangle$  state the more likely is that some of them begin to spontaneously decay. This loss creates holes in the lattice that change the eigenenergies of the collective states and the collective enhancement  $\sqrt{N}$ , thus deteriorating the system performance. However, for our parameters the dominant decoherence mechanism is the fluctuating noise.

in Fig. 6.10 (d), in the absence of decays (triangles), the storage lifetime increases as the number of atom increases to  $N = 10 \times 10$  and decreases for large atom number. We find an optimal number of atoms  $N \sim 100$  for which a compromise is reached between the energy splitting  $\Delta_E$  due the interaction and the enhanced coupling strength  $g\sqrt{N}$  [see vertical dashed in Fig. 6.6 (d)]. We should note that the condition for compensating decoherence not only  $\Delta_E \gg \Gamma$  but also  $\Delta_E \gg g\sqrt{N}$ . In the presence of decays (triangles), despite shorter  $\tau_{stor}$  than the absence of noise, the increase of storage lifetime is not followed by the decrease of it for large atom number. For small-intermediate atom number, the shorter  $\tau_{stor}$  is due to 5% atom loss. However, for large number of atoms, e.g.,  $N = 11 \times 11$ , the atom loss can shift  $\Delta E$  to the regime where  $\Delta E > g\sqrt{N}$  [see Fig. 6.6 (d)]. Consequently, the optimal number of atoms may change in the presence of decays.

We have shown that 2D Rydberg lattices in the presence of DDI close to the surface of a SC cavity are a promising route towards efficient interfacing between cold atoms and SC qubits. For the chosen parameters, the system is sufficiently robust against decoherence due to local fluctuating noise and spontaneous decay. Although we have provided parameters corresponding to the model, we need to know to which state the atoms should be driven and at which distance the 2D lattice should be placed from the cavity surface. In the next section, we address the realistic parameters for atom-cavity interactions  $g$ ,  $C_3$ , the amplitude of  $1/f$  noise and decay rate  $\gamma_s$ .

## 6.5 Robustness against $1/f$ noise

In this section, we discuss the realistic parameters of Fig. 6.1 [51, 167, 168]. Instead of considering laser phase noise such in the previous sections, we focus into local noise model with typical  $1/f$  spectrum and investigate the parameters that optimise the coherence lifetime and retrieval efficiency when the cavity photon is stored in the atomic transitions. The physical system that we consider has been described in the Sec. 6.1. For a SC cavity with stripline length  $L \simeq 1$  cm and electrode distance  $w \simeq 10 \mu\text{m}$  [Fig. 6.1], the effective cavity volume is  $V_c \simeq 6.2 \times 10^{-12} \text{ m}^3$ . Choosing  $m = 2$ , the mode wavelength is  $\lambda_c = 2L/m \simeq 1$  cm, and there are  $m + 1$  field antinodes. With effective dielectric constant  $\epsilon_c \simeq 6$ , the mode frequency is  $\simeq 2\pi \times 12$  GHz. The dipole moment of the Rydberg transition  $\hat{\mu}_{sp}$  with principal quantum numbers  $n$  scales as  $\hat{\mu}_{sp} \sim n^2 a_0 e$ . Thus, for  $w \simeq 10 \mu\text{m}$ ,  $s \simeq 20 \mu\text{m}$ ,  $n \simeq 50$  and  $d \simeq 15 \mu\text{m}$  away from the cavity surface yields  $g_{sp} \simeq 2\pi \times 4$  MHz.

Additional to Sec. 6.1, we should note that the atom-cavity coupling strength depends not only on the principal quantum number  $n$  through the dipole moment ( $\simeq n^2$ ) but also indirectly through the cavity frequency. Here, we intend to fix  $\omega_c \simeq \omega_{ps} \simeq n^{-3}$  the cavity length (and thus the volume) must be adapted to match the transition frequency. This leads to the coupling strength decreasing as  $g \sim n^{-1}$ , and hence Rydberg states of arbitrarily high principal quantum number should not be considered. Therefore, we consider a lattice of  $10 \times 10$   $^{87}\text{Rb}$  atoms excited to the state  $|s\rangle = |50S_{1/2,1/2}\rangle$  that couples

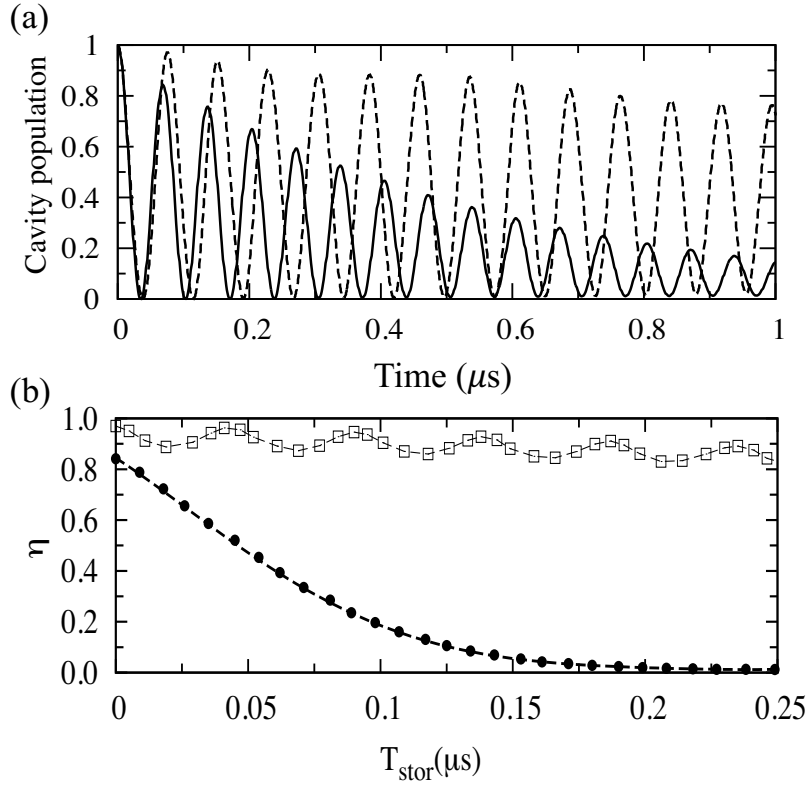


**Figure 6.11:** Panel (a) shows cavity population as a function of time in the absence (black line) and presence (black dashed) of interactions. The parameters for (b) and (c) are  $N = 100$ ,  $n = 50$ , for  $L = 1$  cm and  $w = 15 \mu\text{m}$  at  $d \simeq 15 \mu\text{m}$  from the surface produces  $g \simeq 2\pi \times 4$  MHz,  $\alpha_{np} - \alpha_{ns} \simeq 0.0274 \text{ MHz}/(V/m)^2$ ,  $S_0(d) \simeq 790 (V/m)^2$ ,  $V_0 = 2\pi \times 101.1$  MHz,  $\gamma_p \simeq 4$  kHz, and  $\gamma_s \simeq 7$  kHz obtained from  $10^3$  realisations of a single trajectory calculated by Langevin equation. (b) shows the storage lifetime and maximum retrieval efficiency in the absence (black dots) and the presence (rectangulars) interactions.

by means of microwave field to  $|p\rangle = |50P_{3/2,1/2}\rangle$ . The different electric polarisability between the state  $|s\rangle$  and state  $|p\rangle$  is  $\alpha_{np} - \alpha_{ns} \simeq 0.0274 \text{ MHz}/(V/m)^2$  and the surface noise amplitude is  $S_0(d) \simeq 790 (V/m)^2$  [114]. The spontaneous decays produced from the state  $|s\rangle$  and state  $|p\rangle$  possess the typical rate  $\gamma_s \simeq 7$  kHz and  $\gamma_p \simeq 4$  kHz [70]. For lattice spacing  $a \simeq 3 \mu\text{m}$ , the DDI of  $|50S_{1/2,1/2}, 50P_{3/2,1/2}\rangle$   $C_3 \simeq 2\pi \times 101$  MHz [101, 176].

We have now complete parameters to perform numerical simulations. Similar to the previous section, we firstly consider  $\tau_{\text{coh}}$  as a figure of merit and secondly determine  $\eta$  and  $\tau_{\text{stor}}$  to gain the information of retrieval efficiency. Fig. 6.11(a) shows the average of cavity population as a function of time for  $M = 10^3$  (see caption for detail). We compare weakly interacting Rydberg atoms for lattice spacing  $a = 30 \mu\text{m} \sim C_3/a^3 \simeq 2\pi \times 0.1$  MHz (black line) to the strongly interacting Rydberg atoms for  $a = 3 \mu\text{m} \sim C_3/a^3 \simeq 2\pi \times 101$  MHz (black dashed). In the presence of weak interaction, the local fluctuating noise of  $1/f$  spectrum leads to damping of oscillations. This is due to the fact that in the presence of weak interaction, as similarly illustrated in Fig. 6.4 (b), the energetic shift of collective

states is negligible, and thus cannot prevent the population transfer from a symmetric state to non-symmetric states.

On the other hand, in the presence of strong interaction, i.e., for a lattice spacing  $a = 3 \mu\text{m}$ , the energetic shift of the collective states are large compared to the one with the weak DDI [see Fig. 6.4 (b) red dashed], preventing the population transfer from a symmetric state to non symmetric states. Due to the shifts of collective states, we need to tune  $\Delta$  to the energy of symmetric state such as that the coherence is restored. As shown in Fig. 6.11 (a) (black dashed), the presence of strong DDI also compensate decoherence due to local fluctuating noise with  $1/f$  spectrum. The coherence lifetime in the presence of strong DDI  $\simeq 4\mu\text{s}$ , which is  $\simeq 7.4$  times longer than the presence of weak DDI  $\tau_{coh} \simeq 0.54\mu\text{s}$ . We should note that the coherence is restored as long as the energy separation between a symmetric state and closest non-symmetric state is larger than the power spectral density of  $1/f$  noise  $\Delta_E \gg S_0(15\mu\text{m})$ , and the energy separation is larger than atom-cavity coupling  $\Delta_E \gg g\sqrt{N}$ . Despite the presence of the weak tails of  $1/f$  spectrum noise, as long as the noise acts locally on the Rydberg state, the presence of DDI is sufficiently robust against decoherence due to local fluctuating noise with  $1/f$  spectrum.

Having determined  $\tau_{coh}$  as one of figure of merit, we now determine  $\eta$  and  $\tau_{stor}$ . In Fig. 6.11 (b), we compare the retrieval efficiency between weak (black dots) and strong DDI (squares). We note that the storage lifetime in the presence of strong DDI is  $\simeq 2.53 \mu\text{s}$  and the weak one is  $\simeq 0.13 \mu\text{s}$ . This shows that  $\tau_{stor}$  in the presence of strong DDI is  $\sim 19$  times longer than the weak one. We also observe that the slow decrease of the efficiency for the interacting case is accompanied by small oscillations. As described in the previous section, we attribute those to an imperfect resonant coupling to the target state  $|\varphi_1\rangle$  and to a weak driving of nearby collective states [see Fig. 6.4(a)-(b)].

The performance of our system can be further improved by reducing the lattice spacing, and thus increasing the interaction strength  $C_3/a^3$ . This is demonstrated in Fig. 6.12, where we plot (a) the maximum retrieval efficiency  $\eta_0$  and (b) the storage lifetime  $\tau_{stor}$  as a function of the lattice spacing  $a$ . We observe that the decrease of lattice spacing causes the increase of both  $\eta_0$  and  $\tau_{stor}$ . We should note that for  $2 \leq a < 3 \mu\text{m}$ , although the  $ns - ns$  van der Waals interaction is still weak in this regime, the off-diagonal  $C_6/a^6$  coefficient starts to play role in the dynamics of system. Therefore, we only consider the case  $a \geq 3 \mu\text{m}$ .

We finally analyse  $\eta_0$  (c) and  $\tau_{stor}$  (d) as a function of the number of atoms/sites in the system. Here we only compare the case of the presence of strong (squares) and weak (triangles) DDI. The rate of  $\gamma_s$  and  $\gamma_p$  introduced in the beginning of this section, is small compared to the case in Fig. 6.10 (b) and (d). Consequently, the results are similar to the non-decay case in the previous section. Fig. 6.12 (c) shows  $\eta_0$  as a function of atom number. For the case of weak DDI,  $a \simeq 30 \mu\text{m}$  (triangles), we observe that  $\eta_0$  increases as the number of atoms increases. In comparison, for interacting case,  $\eta_0$  is larger for small-intermediate atom numbers and starts to decrease for large atom numbers.

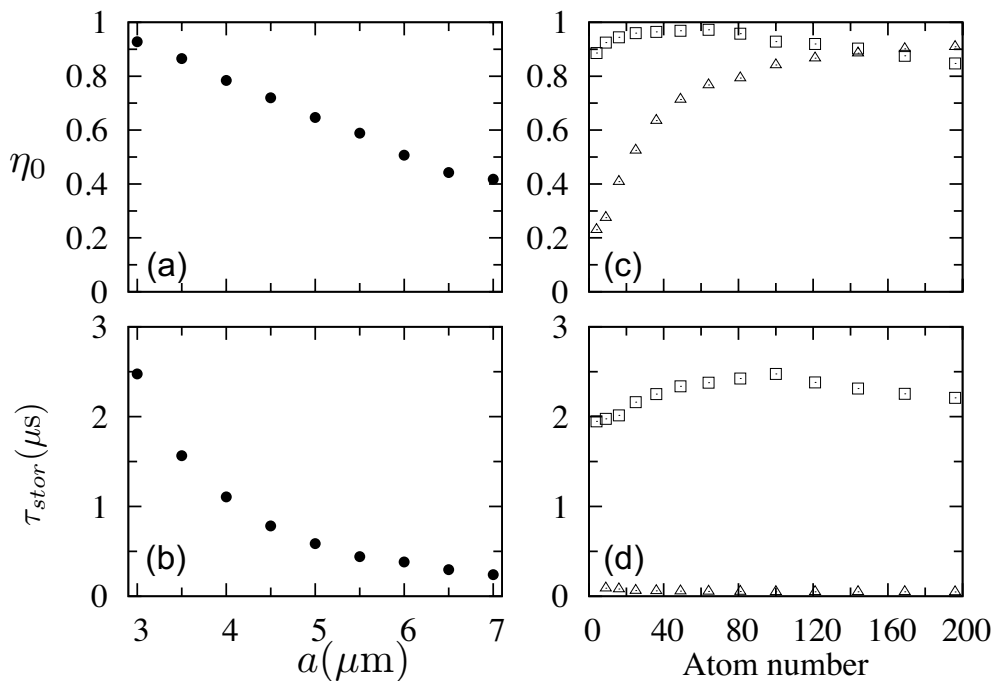


**Figure 6.12:** Panel (a) and (b) show efficiency offset and the storage lifetime as the function of lattice spacing  $a$ , respectively, for  $N = 10 \times 10$ . Panel (c) and (d) show efficiency offset and the storage lifetime as the function of atom number for two different lattice spacing (square denotes  $a \simeq 3 \mu\text{m}$  and triangular denotes  $a \simeq 30 \mu\text{m}$ ). The rest parameters are the same as in Fig. 6.11.

Focusing on the storage lifetime [see Fig. 6.10 (d)], we note that the one with strong DDI clearly outperforms the weak one. For the weak DDI,  $\tau_{stor}$  slightly decreases as the number of atoms increases, although the effect is not significant. This means that the field fluctuations are the dominant decoherence mechanism even at large atom numbers. This slight decrease for increasing atom number is mainly due to the fact that the more atoms in the system the larger the number of non-symmetric states where the population can be incoherently pumped by the fluctuating noise. This is not the case for the strong one (squares), where the lifetime is several times larger than in the non-interacting case. Moreover, for our parameters, we also find an optimal number of atoms  $N \sim 100$ . This shows that for the parameters in the current section, the atom loss is still negligible.

We should note that, overall, the scheme is very challenging to be implemented, as the as light scattered onto SC cavity hampers  $Q$  factor and SC cavity lifetime [177]. However, recent progress via optical microtraps arrays [178–183] are still very promising for realising this hybrid system. Alternatively, the two-dimensional Rydberg ensembles can also be trapped on two-dimensional magnetic microtraps that allows the atoms to be individually addressed in a lattice of  $\simeq 5 \mu\text{m}$  and feasible to be scaled-up on a single chip [184–186]. For example, Recent works shows that a two-dimensional array of traps can accommodate more than 500 atom clouds with lattice spacing  $\simeq 5 \mu\text{m}$  [184, 186] that holds promise for the development of hybrid quantum system. Using the similar parameters as described in the previous paragraph, it is possible to achieve the efficient interfacing

with  $z = 15\mu m$  owing to the development of current efforts based on magnetic trapping of atoms above SC cavity [169].



# Conclusions and Outlook

The first aim of this dissertation was to study non-equilibrium phenomena of many-body physics using systems of Rydberg atoms. Rydberg atoms feature a number of exaggerated properties[69], such as large dipole polarisability and a strong van der Waals interaction, which allow us to create controllable interaction potentials [22, 23]. Together with coherent driving and decoherence, this can lead to non-equilibrium relaxation[24–28], which was also observed experimentally [29–32], and, to non-equilibrium steady-state phase transitions [33–45]. Laser phase noise is one of decoherence source and it acts globally on the excited states of atoms. However, most of previous works considered the local noise [24–28, 46–50], marked in contrast to the nature of laser phase noise.

In chapter 3, we studied the consequences of global noise on the dynamics of driven atom lattices which was compared to local noise. We have shown that although the steady-state excitation number is identical, the excitation distributions differ considerably for both types of noise. Moreover, they feature a dependence on the interaction strength. For weak interaction strength, the relaxation of the number of excitation as well as its variance for local noise is independent of the interaction strength, while for strong interaction strength it does depend on the interaction strength. In contrast to that, the relaxation in the presence of global noise shows a dependence for weak and strong interaction strength. We found that steady-state fluctuations of the number of excitation are suppressed as the number of atoms increases, while for local noise, the fluctuations are constant.

Decoherence also arise due to dissipative processes. The interplay of coherent laser excitation, strongly interacting Rydberg atoms and dissipative processes can lead to the non-equilibrium steady-state phase transitions [33–45]. In chapter 4, we have shown that Rdyberg atom lattices can indeed undergo a dissipative phase transition to a long-range ordered antiferromagnetic phase. The use of three-level schemes that go beyond the inversion limit of a simple two-level driving and a finite laser detuning are key requirements to counteract the effects of the power-law tail of the interaction potential. In addition, fluctuations as well as the weak tail of the rapidly decaying interactions are both found to be essential. This stands marked contrast to equilibrium physics of the corre-

sponding unitary systems, which often is well described by mean-field models [67] and nearest neighbour approximations [68].

In the above cases, decoherence leads to the intriguing non-equilibrium phenomena of many-body physics. However, decoherence is a long-standing problem of coupling quantum states in atoms to solid state devices [148, 167, 168]. The second aim of dissertation was to propose a solution for that problem [51–55]. In chapter 5, we have shown the possibility to enhance the atom-cavity coupling by exploiting the large dipole moment of highly excited Rydberg states. However, the large polarisability ( $\propto n^7$ ) of Rydberg states also makes them more susceptible to spurious electric fields parasitising the metallic cavity surface. For a single atom coupled to SC cavity with typical atom-cavity distance [54, 55, 61, 169], the system indeed undergoes strong decoherence. Therefore, in chapter 6, we proposed a noise-resistant interface of a collection of Rydberg atoms and a single photon in a SC cavity by means of (resonant) dipole-dipole interactions. Instead very large atoms clouds ( $N \simeq 10^6$  atoms) [60], we use an atomic lattice with up to hundreds atoms. In such system, dipole-dipole interactions are exploited to compensate dephasing of Rydberg states due to fluctuating electric field from the SC cavity surface.

We have shown that a two-dimensional Rydberg lattice in the presence of dipole-dipole interactions close to the surface of a SC cavity are a promising route towards efficient interfacing of cold atoms and superconducting qubits. The dipole-dipole interaction protects the coherent dynamics of the atoms-cavity coupling against local electric field fluctuations arising from the surface. This leads to an enhancement of the retrieval efficiency of the MW photon into the cavity for small to moderate atom numbers and long lifetimes of the excitation stored in the atoms compared to the situation with non-interacting atoms. Moreover, for the parameters considered, we have shown that a strong coupling of the cavity and the atoms is possible, allowing to interface our system with a superconducting qubit, and that the atom loss due to spontaneous emission is negligible even for large atom numbers.

## 6.6 Future perspective

The previously discussed results have generated new questions and ideas that call for further investigations. Below, a few specific ideas are outlined, which might provide promising avenue of research.

### Rydberg ensembles in the presence of phase noise

In chapter 3, we investigated the consequences of global noise on the dynamics of driven atom lattices which was compared to local noise. We have shown that although the steady-state excitation number is identical, the excitation distributions differ considerably for both types of noise. This generates an open question of the statistics distribution

due to the presence of global noise. The experimental demonstration of atom counting statistics have been recently investigated by means of Rydberg gases [29–32]. While most previous works considered local noise [24–28, 46–50], it would further be great interest to investigate the consequences of global noise of those systems and gain insight of atom counting statistics. Moreover, the use of Langevin equation in chapter 3 limits the calculation up to  $N < 20$ . Thus, for  $N > 20$ , the use of another numerical method in the basis of matrix product states is required to determine excitation distributions in the presence of global noise.

The experimental demonstration of local and global noise can also be performed in the lattices. The experiments have reached the stage where individual atoms can be trapped in one or two dimensional arrays of optical microtraps with arbitrary geometries. The filling fractions range from 60 to 100% [111]. The noise can be generated by the arbitrary waveform generator. The bandwidth of this noise can be controlled by applying a low-pass filter of cut-off frequency. For the local noise, one should use separated single beam which produces uncorrelated beams<sup>†</sup>.

## Rydberg ensembles in the presence of dissipation

While we have focused on neutral-atom settings with *finite-range* van der Waals interactions ( $\alpha = 6$ ), effective quantum magnets with variable power-law interactions [187] are currently attracting great interest in the context of laser-cooled ion crystals in which various spin models [188] with  $\alpha = 0 \dots 3$ , can be realised in one and two dimensions [189–191]. This systems inherently feature dissipation [192] and thus provide an interesting platform to explore the dissipative phase transition in the non-equilibrium steady state also in the *long-range* interaction regime. In light of the demonstrated inadequacy of mean field theory, for example in the presence of sufficiently strong dissipation [37], it would further be of great interest to investigate other dissipative phase transitions predicted by mean field treatment [8, 35, 43] and gain insight into their validity for open systems as well as the critical dimension for long-range order in such related spin lattices.

## Noise-resistant quantum interface

In the chapter 6, we have shown that a two-dimensional Rydberg lattice in the presence of dipole-dipole interactions close to the surface of a SC cavity are a promising route towards efficient interfacing of cold atoms and superconducting qubits. However, despite the recent progress regarding atoms in optical microtraps arrays [178–183] for the implementation of the system proposed here setups without strong optical fields would be preferable as scattered photons can easily destroy the superconducting qubit state. For instance, atoms can be trapped individually addressed in two-dimensional magnetic microtraps on atom chips [184–186] or in the evanescent field of optical nanofibers [193, 194]. Those

<sup>†</sup> Discussion with Thierry Lahaye

systems would represent a promising avenue for implementing a noise-resistant hybrid interface of Rydberg atoms and superconducting qubits in microwave cavities.

# Appendix



# The multipole expansion of dipole-dipole interactions

## A.1 Multipole expansion of dipole-dipole interactions

We calculate the multipole expansion of  $V_{dd}(\hat{\mathbf{R}}, \hat{\mathbf{r}}_{1A}, \hat{\mathbf{r}}_{2B})$ . We set

$$f(x) = \frac{1}{|\hat{\mathbf{R}} - \hat{\mathbf{x}}|}, \quad (\text{A.1})$$

hence

$$V_{dd}(\hat{\mathbf{R}}, \hat{\mathbf{r}}_{1A}, \hat{\mathbf{r}}_{2B}) = f(0) - f(\hat{\mathbf{r}}_{1A}) - f(\hat{\mathbf{r}}_{2B}) + f(\hat{\mathbf{r}}_{1A} - \hat{\mathbf{r}}_{2B}). \quad (\text{A.2})$$

In addition we expand  $f$ :

$$\begin{aligned} f(0) &= \frac{1}{R} \\ \partial_i f(x) &= \frac{R_i - x_i}{|\hat{\mathbf{R}} - \hat{\mathbf{x}}|^3} \\ \partial_i f(0) &= \frac{R_i}{R^3} \\ \partial_{ij} f(x) &= \frac{\delta_{ij}}{|\hat{\mathbf{R}} - \hat{\mathbf{x}}|^3} + \frac{3(x_i - R_i)(x_j - R_j)}{|\hat{\mathbf{R}} - \hat{\mathbf{x}}|^5} \\ \partial_{ij} f(0) &= \frac{\delta_{ij}}{R^3} + \frac{3R_i R_j}{R^5}. \end{aligned}$$

Inserting these expression to the multidimensional Taylor expansion

$$f(\hat{\mathbf{x}}) = f(0) + \sum_{i=1}^3 x_i \partial_i f(0) + \frac{1}{2} \sum_{i,j=1}^3 x_i x_j \partial_{ij} f(0) + \mathcal{O}(x^3), \quad (\text{A.3})$$

we find the second order approximation

$$\begin{aligned} f(x) &= \frac{1}{R} + \frac{1}{R^3} \sum_{i=1}^3 x_i R_i + \frac{1}{2} \sum_{i,j=1}^3 x_i x_j \left( -\frac{\delta_{ij}}{R^3} + \frac{3R_i R_j}{R^5} \right) \\ &= \frac{\hat{\mathbf{x}} \cdot \hat{\mathbf{R}}}{R^3} + \frac{3}{2R^5} (\hat{\mathbf{x}} \cdot \hat{\mathbf{R}})^2 - \frac{x^2}{2R^3}. \end{aligned}$$

Inserting this second order approximation to (A.3) yields

$$\begin{aligned} V_{dd}(\hat{\mathbf{R}}, \hat{\mathbf{r}}_{1A}, \hat{\mathbf{r}}_{2B}) &= - \left( \frac{\hat{\mathbf{r}}_{1A} \cdot \hat{\mathbf{R}}}{R^3} + \frac{3}{2R^5} (\hat{\mathbf{r}}_{1A} \cdot \hat{\mathbf{R}})^2 - \frac{r_{1A}^2}{2R^3} \right) \\ &\quad - \left( \frac{-\hat{\mathbf{r}}_{2B} \cdot \hat{\mathbf{R}}}{R^3} + \frac{3}{2R^5} (\hat{\mathbf{r}}_{2B} \cdot \hat{\mathbf{R}})^2 - \frac{r_{2B}^2}{2R^3} \right) \\ &\quad + \frac{(\hat{\mathbf{r}}_{1A} - \hat{\mathbf{r}}_{2B}) \cdot \hat{\mathbf{R}}}{R^3} + \frac{3}{2R^5} [(\hat{\mathbf{r}}_{1A} - \hat{\mathbf{r}}_{2B}) \cdot \hat{\mathbf{R}}]^2 - \frac{(\hat{\mathbf{r}}_{1A} - \hat{\mathbf{r}}_{2B})^2}{2R^3} \\ &= \frac{\hat{\mathbf{r}}_{1A} \cdot \hat{\mathbf{r}}_{2B}}{R^3} + \frac{3}{R^5} (\hat{\mathbf{r}}_{1A} \cdot \hat{\mathbf{R}}) (\hat{\mathbf{r}}_{2B} \cdot \hat{\mathbf{R}}). \end{aligned} \tag{A.4}$$

Finally we arrive at the dipole-dipole interaction  $\hat{H}_{dd}$  in the limit of  $R \gg r_i$

$$\hat{H}_{dd} = \frac{\hat{\mu}_{1A} \cdot \hat{\mu}_{2B} - 3(\hat{\mu}_{1A} \cdot \mathbf{n})(\hat{\mu}_{2B} \cdot \mathbf{n})}{4\pi\epsilon_0 R^3}, \tag{A.5}$$

where the dipole moment operator is defined as  $\hat{\mu} = e\hat{\mathbf{r}}_i$  and  $\mathbf{n} = \hat{\mathbf{R}}/R$ .



# Simulation Methods

## B.1 Quantum simulations of smaller lattice

The quantum simulation based on quantum jump approach [115–118] is a numerical simulation technique which involves a stochastic evolution of wave functions. This method is equivalent to density matrix master equation and is fascinating due to the following advantages: (i) In comparison to the density matrix master equation, the dimension of corresponding Hilbert space scales as  $2^N$  rather than  $2^{2N}$ . (ii) It allows us to gain a new physical insight, e.g., two-time correlation function, that cannot be gained by the density matrix master equation.

Monte Carlo wave functions consist of two elements: (i) evolution with a non-Hermitian Hamiltonian, (ii) random jumps, followed by wave function renormalisation. More precisely, a non-hermitian Hamiltonian including the anti-commutator of Lindblad terms in (4.12) is given by,

$$\hat{H}_{nh} = \hat{H} - \frac{i}{2} \sum_{\alpha=1}^N \hat{C}_{(\alpha)}^\dagger \hat{C}_{(\alpha)} \quad (\text{B.1})$$

with  $\hat{C}_\alpha = \sqrt{\gamma_e} \hat{\sigma}^-$  [see Fig. 4.1(c) for the illustration]. For the two-level system that consists of a ground  $|g\rangle$  and an excited state  $|e\rangle$  with a lifetime  $\gamma_e^{-1}$ , the operator  $\hat{\sigma}$  can be written in the form  $\hat{\sigma}^\dagger = |e\rangle\langle g|$  and  $\hat{\sigma} = |g\rangle\langle e|$ . The time evolution of the many-body wave function  $|\psi(t)\rangle$  for an infinitesimal time step  $\delta t$  is given by

$$|\psi'(t + \delta t)\rangle = \left(1 - i\hat{H}_{nh}\delta t\right) |\psi(t)\rangle \quad (\text{B.2})$$

which is simply the expansion of the time translation operator  $\exp\left[-i\hat{H}_{nh}\delta t\right]$  to first order in  $\delta t$  and the prime ' is introduced to indicate the unnormalised wavefunction. As

$\hat{H}_{nh}$  is non-hermitian, the latest wavefunction is not normalised. The square of norm reads

$$\begin{aligned}
\langle \psi'(t + \delta t) | \psi'(t + \delta t) \rangle &= \langle \psi(t) | \left(1 - i\hat{H}_{nh}\delta t\right) \left(1 - i\hat{H}_{nh}\delta t\right) | \psi(t) \rangle \\
&= 1 - i\delta t \langle \psi(t) | \left(\hat{H}_{nh} - \hat{H}_{nh}^\dagger\right) | \psi(t) \rangle \\
&= 1 - \delta t \langle \psi(t) | C_\alpha^\dagger C_\alpha | \psi(t) \rangle \\
&= 1 - \delta p.
\end{aligned} \tag{B.3}$$

where  $\delta p$  reads as

$$\delta p = \sum_{\alpha} \delta p_{\alpha} \text{ with } \delta p_{\alpha} = \langle \psi(t) | C_{\alpha}^{\dagger} C_{\alpha} | \psi(t) \rangle \delta t \geq 0. \tag{B.4}$$

Here  $\delta p$  denotes the probability of having a jump and the time step  $\delta t$  is adjusted such that the first order calculation is valid. In particular, it requires  $\delta p \ll 1$  and hence the second order term  $\delta t^2$  is neglected. In order to determine the occurrence of the jump, the probability of having a jump is compared to the a quasi-random number  $r$ , uniformly distributed between 0 and 1. If  $r < \delta p$ , the quantum jump occurs and we choose a new normalised wavefunction at  $t + \delta t$  according to  $\delta p_{\alpha}/\delta p$

$$|\psi(t + \delta t)\rangle = \hat{C}_{\alpha} \frac{|\psi(t)\rangle}{\sqrt{\delta p_{\alpha}/\delta t}} \tag{B.5}$$

if  $r$  is larger than  $\delta p$ , which occurs in most cases since  $\delta p \ll 1$ , no quantum jump occurs and we take the following for the new normalised wavefunction at  $t + \delta t$ .

$$|\psi(t + \delta t)\rangle = \frac{|\psi'(t + \delta t)\rangle}{\sqrt{1 - \delta p}}. \tag{B.6}$$

This procedure can be translated into numerical algorithm shown in shown in the algorithm 1. Following the description in the chapter 4, for  $M$  realisations  $|\psi^{(k)}\rangle$ , we calculate the excited state population  $\langle \hat{\sigma}_{ee}^{k,\alpha} \rangle = \langle \psi^{(k)} | \hat{\sigma}_{ee}^{(\alpha)} | \psi^{(k)} \rangle$  and take its average

$$N_{ee} = \frac{1}{M} \sum_{k=1}^M \sum_{\alpha=1}^N \langle \hat{\sigma}_{ee}^{(k,\alpha)} \rangle, \tag{B.7}$$

where  $N$  is the atom number. For sufficiently large  $M$ , the average converges.

We now show that the monte Carlo wave functions are equivalent to the density matrix master equation. In particular, we consider the quantity  $\overline{\rho(t)}$  obtained by averaging  $\rho(t) = |\psi(t)\rangle\langle\psi(t)|$  over  $M$  realisations at time  $t$  of the single trajectory starting in  $|\psi(0)\rangle$ . For a single trajectory  $|\psi(t)\rangle$  at time  $t + \delta t$ , the average value of  $\rho(t + \delta t)$  over the evolution in the presence of the jump processes reads

$$\overline{\rho(t + \delta t)} = (1 - \delta p) \frac{|\psi'(t + \delta t)\rangle\langle\psi'(t + \delta t)|}{\sqrt{1 - \delta p}} + \sum_{\alpha} \delta p_{\alpha} \frac{C_{\alpha} |\psi(t)\rangle\langle\psi(t)| C_{\alpha}^{\dagger}}{\sqrt{\delta p_{\alpha}/\delta t}} \tag{B.8}$$

```

for many realisations do
  Initialise the system in the ground state;
  while  $t \leq t_{max}$  do
    Calculate the probability of jump  $\delta p = \sum_{\alpha=1}^N \delta p_{\alpha}$ ;
    Draw a random number  $r_1 \in [0, 1]$  if  $\delta p < r_1$  then
      Calculate the non-Hermitian time evolution  $\exp[-i\hat{H}_{nh}\delta t]$ ;
    else
      Draw a random number  $r_2 \in [0, 1]$ ;
      Determine the jump with probability  $\delta p_{\alpha}/\delta p$ ;
      Collapse the wave function
    end
    Normalise the wave function Update the time  $t \rightarrow t + \delta t$ 
  end
end
Average over the quantum trajectories
Algorithm 1: Monte Carlo wave function algorithm

```

Inserting (B.2) to (B.8) we find

$$\begin{aligned} \overline{\rho(t + \delta t)} &= \rho(t) - i\delta t [\hat{H}, \rho(t)] \\ &+ \sum_{\alpha} \left( -\frac{1}{2} C_{\alpha}^{\dagger} C_{\alpha} \rho(t) - \frac{1}{2} \rho(t) C_{\alpha}^{\dagger} C_{\alpha} + C_{\alpha} \rho(t) C_{\alpha}^{\dagger} \right) \end{aligned} \quad (\text{B.9})$$

For a small time step  $\delta t$ , this is simply the master equation with the time derivative written as a difference quotient,

$$\partial_t \overline{\rho(t)} = \left( \overline{\rho(t + \delta t)} - \overline{\rho(t)} \right) / \delta t = - \left[ \hat{H}, \overline{\rho(t)} \right] + \sum_{\alpha} \mathcal{L}(C_{\alpha}) \left[ \overline{\rho(t)} \right] \quad (\text{B.10})$$

where we averaged over the density matrix at time  $t$  as well. If the initial conditions of master equation and the quantum jump approach coincide, the exact density matrix and the one obtained by averaging, Eq. (B.10), coincide as well, at any time  $t$  [115].

We finally compare the result of monte Carlo wave function and density matrix master equation. We consider the case of two interacting atoms, each with a ground state  $|g\rangle$  and an excited state  $|e\rangle$ . A pair of excited atoms at sites  $\alpha$  and  $\beta$  experiences the repulsive van der Waals (vdW) interaction  $V_0/|\alpha - \beta|^6$  with  $V_0 = C_6/a^6$  and  $C_6 > 0$ . Resonant transitions between the two states are driven by a laser with Rabi frequency  $\Omega$ , which cause the spontaneous decay from the excited state  $|e\rangle$  with the decay rate  $\gamma_e$ . Fig. B.1 shows the fraction of Rydberg atoms,  $f_e = N_{ee}/N$ , as the function of time calculated by monte carlo wave function and density matrix master equation for the case of a single atom B.1 (a) and two interacting atoms B.1 (b). The results produced by monte Carlo wave functions are in well agreement with the density matrix one for large number of realisations  $M$ .

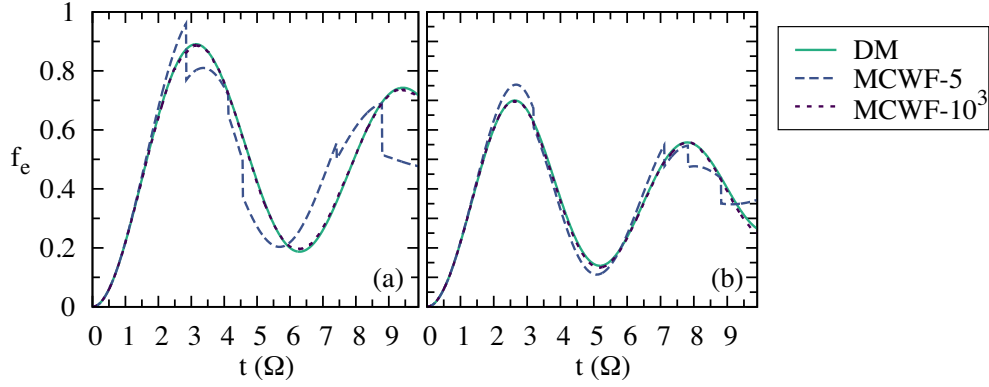


**Figure B.1:** The fraction of Rydberg atoms as the function of time for a single atom (a) and two interacting atoms with  $V_0 = 1\Omega$  (b). The fraction of Rydberg atoms from density matrix master equation (DM) is compared to the result of monte carlo wave equation (MCWF). The rest parameters are  $\gamma_e = 0.1\Omega$  (see the legend for details).

## B.2 Dynamic and Steady-state Monte Carlo

In this section, we describe the algorithms of dynamic and steady-state Monte Carlo. For dynamic Monte Carlo, we use kinetic Monte Carlo (KMC) [195, 196] algorithm, while for the steady-state evolution we use steady-state Monte Carlo (ssMC) [128]. KMC is the developed monte Carlo algorithm which is intended to overcome the time scale problem in the metropolis algorithm [197]. It is widely used in the variety of subjects, such as, surface adsorption, diffusion and growth [198–200] as well as statistical physics [201, 202]. Here, KMC is used to efficiently solve the time-dependent rate equation (4.25), which is given by,

$$\begin{aligned} \dot{\rho}_{S_1, \dots, S_N} = & \sum_i \left[ (1 - S_\alpha) \Gamma_\downarrow^{(3)}(\delta_\alpha) + S_\alpha \Gamma_\uparrow^{(3)}(\delta_\alpha) \right] \rho_{S_1, \dots, 1-S_\alpha, \dots, S_N} \\ & - \left[ (1 - S_\alpha) \Gamma_\uparrow^{(3)}(\delta_\alpha) + S_\alpha \Gamma_\downarrow^{(3)}(\delta_\alpha) \right] \rho_{S_1, \dots, S_\alpha, \dots, S_N}, \end{aligned} \quad (\text{B.11})$$

where effective rate equation for the joint probabilities  $\rho_{S_1, \dots, S_N}$  of Rydberg excitations being present ( $S_\alpha = 1$ ) or not present ( $S_\alpha = 0$ ) at the  $\alpha$ th site and the corresponding many-body states are connected by the single-atom excitation  $[\Gamma_\uparrow^{(3)}(\delta_\alpha)]$  and de-excitation  $[\Gamma_\downarrow^{(3)}(\delta_\alpha)]$  rates [47, 106, 127, 128]. In the many-body basis  $B = \{(S_1, \dots, S_N) | S \in \{0, 1\}\}$ , we can rewrite the rate equation (B.11) as [195]

$$\frac{d\sigma_\nu}{dt} = \sum_{\nu'} (\Gamma_{\nu\nu'} \sigma_{\nu'} - \Gamma_{\nu'\nu} \sigma_\nu) \quad (\text{B.12})$$

with  $\sigma_\nu \in B$ , which denoting the probability for configuration  $\nu$ ,  $\Gamma_{\nu\nu'}$  the respective excitation rates to the many-body state  $\sigma_\nu$  and  $\Gamma_{\nu'\nu}$  the respective rates of being escape from the many-body state  $\sigma_\nu$ . As the master equation is loss-gain equation,  $\Gamma_{\nu\nu} = 0$ . Defining the matrices  $(\mathbf{T})_{\nu\nu'} = \Gamma_{\nu\nu'}$ ,  $(\mathbf{U})_{\nu\nu'} = \sum_{\tilde{\nu}} \Gamma_{\tilde{\nu}\nu'}$  for  $\nu = \nu'$  and zero otherwise, we

find Eq. (B.12) can be written as the matrix notation given by

$$\frac{d\sigma}{dt} = -(\mathbf{U} - \mathbf{T})\sigma. \quad (\text{B.13})$$

We define the matrix  $\mathbf{R}(t) = \exp[-\mathbf{U}t]$  to determine the probability that the system has not yet escaped from the configuration  $\nu$ :

$$p_\nu(t) = (R)_{\nu\nu}(t) = \exp[-(U)_{\nu\nu}t]. \quad (\text{B.14})$$

Hence, the probability that the system has escaped from the configuration  $\nu$   $p_{\bar{\nu}}(t) = 1 - p_\nu(t)$ , which has the probability distribution  $\partial_t p_{\bar{\nu}} = (U)_{\nu\nu} \exp[-(U)_{\nu\nu}t]$ . The average time for escape  $\tau$  is only the first moment of the probability distribution,

$$\tau = \int_0^\infty t p_{\bar{\nu}} dt = \frac{1}{U}. \quad (\text{B.15})$$

We can thus draw the time of the first change of the system by solving  $p_{\bar{\nu}}=r$ , where  $r$  is a uniform random number on the unit interval [195], which gives simply  $\exp[-(U)_{\nu\nu}t] = r$ , or, solved for  $t$ ,

$$t = -\ln[r] / (U)_{\nu\nu}. \quad (\text{B.16})$$

In our simulation, with respect to our rate equation (B.11), the change of state depends of to the total rate  $\Gamma_{\uparrow\downarrow}$ , where the  $\Gamma_{\uparrow}$  denotes the excitation rate and  $\Gamma_{\downarrow}$  denotes de-excitation rate. The time for the next change of the system is then calculated via  $t = -\ln[r] / \Gamma_{\uparrow\downarrow tot}$ . The algorithm of numerical implementation is shown in algorithm 2. For  $M$  number of realisations, the observables converge. The typical number of realisations to produce the reasonable data is in the order of thousands.

When we solve the Eq. (B.11) by means of KMC, non-physical negative rates frequently occur [129]. Although modifying the rates in such a way that the correct steady state is preserved [127], this technique is rather expensive and impractical for general systems. Therefore, we use another approach that has been developed in [128]. There, the calculation of the dynamics of the system was neglected in favour of the steady-state calculation. In this technique, we use the steady-state of Rydberg state instead of the single-atom rates in Eq. (4.21). The detail of ssMC method including its algorithm is given in Ref. [128].

## B.3 Mean field

In the chapter 4, we identify the advantages of rate equations over the mean field method. Here, we briefly describe the mean field method that we used in Fig. 4.8 and Fig. 4.9. The essence of this method is the neglect of any correlation to simplify the complexity of full quantum problem. This method is relevant for high dimensional problems, but

```

for many realisations do
  Initialise the system in the ground state;
  while  $t \leq t_{max}$  do
    for  $\alpha \leq N$  do
      Calculate  $\Delta_{\text{eff}}$  based on the current configuration;
      if state $_{\alpha}$  is in excited state then
        Calculate  $\Gamma_{\downarrow}^{\alpha}$ ;
      else
        Calculate  $\Gamma_{\uparrow}^{\alpha}$ ;
      end
    end
    Draw random numbers  $r_1, r_2 \in [0, 1]$ ;
    Determine  $\delta t = \ln[r_1] / \Gamma_{\uparrow\downarrow tot}$ , update time;
    Determine atom  $\beta$  that changes its state via
     $\sum_{\alpha=1}^{\beta-1} \Gamma_{\uparrow\downarrow}^{\alpha} \leq r_2 \Gamma_{\uparrow\downarrow tot} < \sum_{\alpha=1}^{\beta} \Gamma_{\uparrow\downarrow}^{\alpha}$ ;
    Change state of atom  $\beta$ ;
  end
end
Average over the quantum trajectories

```

**Algorithm 2:** Kinetic Monte Carlo algorithm for the rate equation

not an accurate method for low dimensional problem. For equilibrium spin models, mean field method can efficiently predict the existence of various phases [203]. For the current nonequilibrium case, we use the approach of [113, 204]: factorise the density matrix by site,  $\rho = \bigotimes_j \rho_j$ , and work with the reduced density matrices,  $\rho_j = \text{Tr}_{\neq j} \rho$ . This accounts for on-site quantum fluctuations but not inter-site fluctuations: for atom  $j$ , the interaction  $|e\rangle\langle e|_j \otimes \sum_k |e\rangle\langle e|_k$ , is replaced with the mean field,  $|e\rangle\langle e|_j \sum_k \rho_{k,ee}$ . In high dimensions, this is a good approximation since fluctuations of the neighbours average out. Then the evolution of each  $\rho_j$  is given by

$$\begin{aligned}
\dot{\rho}_{j,gg} &= i\frac{\Omega_1}{2} (\rho_{gp} - \rho_{pg}) + \gamma_p \rho_{pp} \\
\dot{\rho}_{j,pp} &= -i\frac{\Omega_1}{2} (\rho_{gp} - \rho_{pg}) - i\frac{\Omega_2}{2} (\rho_{ep} - \rho_{pe}) - \gamma_p \rho_{pp} \\
\dot{\rho}_{j,ee} &= i\frac{\Omega_2}{2} (\rho_{ep} - \rho_{pe}) \\
\dot{\rho}_{j,gp} &= -i\frac{\Omega_1}{2} (\rho_{pp} - \rho_{gg}) + i\frac{\Omega_2}{2} \rho_{ge} - \frac{\gamma_p}{2} \rho_{gp} \\
\dot{\rho}_{j,ge} &= -i\frac{\Omega_1}{2} \rho_{pe} + i\frac{\Omega_2}{2} \rho_{gp} - i\delta_{\text{eff}} \rho_{ge} \\
\dot{\rho}_{j,pe} &= -i\frac{\Omega_1}{2} \rho_{ge} + i\frac{\Omega_2}{2} (\rho_{pp} - \rho_{ee}) - i\delta_{\text{eff}} \rho_{pe} - \frac{\gamma_p}{2} \rho_{pe} \\
\dot{\rho}_{\alpha\beta} &= (\dot{\rho}_{\beta\alpha})^* .
\end{aligned} \tag{B.17}$$

where  $\delta_{\text{eff}} \equiv \Delta - V_0 \sum_k \rho_{k,ee}$  denotes the effective two-photon detuning. The rest of the symbols have been described in chapter 4. The equations above have a steady-state

solution and its stability. The stability analysis of steady-state solution has been studied in [33, 36]. We use the order parameter  $q$  [see Eq. (4.9)] to characterise the phase transitions. As mentioned in Sec. 4.2, the lattice is divided into two sublattices, i.e., sublattice A and B. We thus have

$$\begin{aligned}
\dot{\rho}_{A,gg} &= i\frac{\Omega_1}{2}(\rho_{gp} - \rho_{pg}) + \gamma_p \rho_{pp} \\
\dot{\rho}_{A,pp} &= -i\frac{\Omega_1}{2}(\rho_{gp} - \rho_{pg}) - i\frac{\Omega_2}{2}(\rho_{ep} - \rho_{pe}) - \gamma_p \rho_{pp} \\
\dot{\rho}_{A,ee} &= i\frac{\Omega_2}{2}(\rho_{ep} - \rho_{pe}) \\
\dot{\rho}_{A,gp} &= -i\frac{\Omega_1}{2}(\rho_{pp} - \rho_{gg}) + i\frac{\Omega_2}{2}\rho_{ge} - \frac{\gamma_p}{2}\rho_{gp} \\
\dot{\rho}_{A,ge} &= -i\frac{\Omega_1}{2}\rho_{pe} + i\frac{\Omega_2}{2}\rho_{gp} - i(\Delta - V_0\rho_{B,ee})\rho_{ge} \\
\dot{\rho}_{A,pe} &= -i\frac{\Omega_1}{2}\rho_{ge} + i\frac{\Omega_2}{2}(\rho_{pp} - \rho_{ee}) - i(\Delta - V_0\rho_{B,ee})\rho_{pe} - \frac{\gamma_p}{2}\rho_{pe} \\
\dot{\rho}_{B,gg} &= i\frac{\Omega_1}{2}(\rho_{gp} - \rho_{pg}) + \gamma_p \rho_{pp} \\
\dot{\rho}_{B,pp} &= -i\frac{\Omega_1}{2}(\rho_{gp} - \rho_{pg}) - i\frac{\Omega_2}{2}(\rho_{ep} - \rho_{pe}) - \gamma_p \rho_{pp} \\
\dot{\rho}_{B,ee} &= i\frac{\Omega_2}{2}(\rho_{ep} - \rho_{pe}) \\
\dot{\rho}_{B,gp} &= -i\frac{\Omega_1}{2}(\rho_{pp} - \rho_{gg}) + i\frac{\Omega_2}{2}\rho_{ge} - \frac{\gamma_p}{2}\rho_{gp} \\
\dot{\rho}_{B,ge} &= -i\frac{\Omega_1}{2}\rho_{pe} + i\frac{\Omega_2}{2}\rho_{gp} - i(\Delta - V_0\rho_{A,ee})\rho_{ge} \\
\dot{\rho}_{B,pe} &= -i\frac{\Omega_1}{2}\rho_{ge} + i\frac{\Omega_2}{2}(\rho_{pp} - \rho_{ee}) - i(\Delta - V_0\rho_{A,ee})\rho_{pe} - \frac{\gamma_p}{2}\rho_{pe} \\
\dot{\rho}_{\alpha\beta} &= (\dot{\rho}_{\beta\alpha})^* .
\end{aligned} \tag{B.18}$$

As illustrated in Fig. 4.1 (a), the order parameter  $q$  characterise the population imbalance on the two sublattices, with  $q > 0$  in the ordered phase and  $q = 0$  in the disordered phase. Here, due to the conservation probability [see Eq. (4.14)], the  $q$  is defined as  $q = |\rho_{ee}^A - \rho_{ee}^B|$ . Following the parameters scaling in the chapter 4, we use the following parameters :

$$\Omega_2 = \Omega_1 \sqrt{\frac{1-p_0}{p_0}}, \tag{B.19}$$

and

$$\gamma_p = \sqrt{\frac{1}{2}(\Omega_1^2 + \Omega_2^2)^2 - 2\Omega_1^2}. \tag{B.20}$$

For the mean field results in Fig. 4.8, the parameters that we use are  $p_0 = 0.96$ ,  $\Omega_1 \simeq 3\omega$ , and  $V_0 = 5\omega$ . For Fig. 4.9, we fix  $\Omega_1$  and vary  $p_0$  and  $V_0$ .





# The population inversion due to the presence of dark state

Here we briefly discuss a concise way of expressing the single-atom eigenstates of Hamiltonian 4.11 in terms of the "mixing angles"  $\theta$  and  $\phi$  that are dependent in a simple way upon the Rabi couplings. For multi-photon resonance, the mixing angles are given by

$$\tan \theta = \Omega_1 / \Omega_2 \quad (\text{C.1})$$

$$\tan 2\phi = \sqrt{\Omega_1^2 + \Omega_2^2} / \Delta \quad (\text{C.2})$$

The eigenstates can then be written in terms of the bare atom states:

$$|a^+\rangle = \sin \theta \cos \phi |g\rangle + \cos \phi |p\rangle + \cos \theta \sin \phi |e\rangle \quad (\text{C.3})$$

$$|a^-\rangle = \sin \theta \cos \phi |g\rangle - \sin \phi |p\rangle + \cos \theta \cos \phi |e\rangle \quad (\text{C.4})$$

$$|a^0\rangle = \cos \theta |g\rangle - \sin \theta |e\rangle. \quad (\text{C.5})$$

When  $|a^0\rangle$  remains at zero energy, the pair states  $|a^+\rangle$  and  $|a^-\rangle$  are splitted by an amount  $\hbar\omega^\pm$ ,

$$\hbar\omega^\pm = \frac{\hbar}{2} \left( \Delta \pm \sqrt{\Delta^2 + \Omega_1^2 + \Omega_2^2} \right). \quad (\text{C.6})$$

The states  $|a^\pm\rangle$  pertain an element of all of the bare atomic states. In contrast to a states  $|a^\pm\rangle$ , state  $|a^0\rangle$  has no contribution from  $|p\rangle$  and is therefore the dark state. Due to this state, there is no possibility of excitation to a state  $|p\rangle$  and subsequent spontaneous decay.

Evolution into the dark state via optical pumping (through spontaneous decay from  $|p\rangle$ ) can be a means to trap population in this state that is well known in laser spec-

troscopy and laser-atom manipulation. Electronically induced transparency (EIT) offers an alternative, adiabatic, and much more rapid passage to evolve into this state. For the population inversion, the system starts with all the amplitude in the ground state  $|g\rangle$  via  $\Omega_1 \ll \Omega_2$ . Furthermore,  $\Omega_1$  is gradually increased while  $\Omega_2$  is gradually decreased and hence  $\Omega_1 \gg \Omega_2$ . When the probe is on resonance ( $\Delta = 0$ ), the dark state becomes  $|a^0\rangle = -|e\rangle$  and  $|a^\pm\rangle = (1/\sqrt{2})(|p\rangle \pm |e\rangle)$  becomes a ground state. Consequently, the system becomes the effective two-level driving scheme [see Fig. 4.1(d)] and the population is now fully pumped to the state  $|a^0\rangle = -|e\rangle$ .

# Appendix D

## State truncation

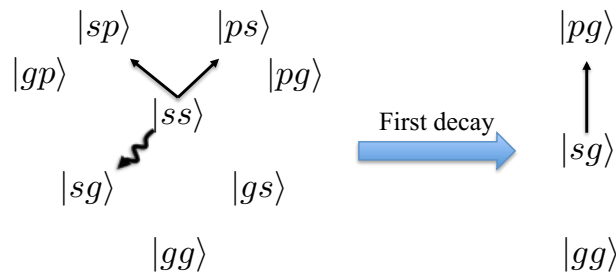


**Figure D.1:** The truncation of states due to the absence of driving force between the state  $|g\rangle$  and  $|s\rangle$ .

In this appendix, we describe the truncation of the states due to the absence of the driving force between the ground state  $|g\rangle$  and the state  $|s\rangle$ . For the sake of simplicity, we consider two-atom case. Suppose the initial condition of the system is  $|ss\rangle = 1$  and the total number of states before the atom loss processes is  $N_s = 8$  (see Fig. D.1). When the first event of spontaneous decay occurs, e.g., state  $|ss\rangle$  to state  $|sg\rangle$ . The state  $|sg\rangle$  subsequently couples to the state  $|pg\rangle$ . Consequently, the rest of the states, excepts  $|sg\rangle$  and  $|pg\rangle$ , can be truncated. In numerical implementation, this can be performed by truncating the state during dynamical process. As shown in Fig. D.1, the truncation of states leads to the 5 states reduction.



# References

- [1] M. C. Cross and P. C. Hohenberg, “Pattern formation outside of equilibrium,” *Rev. Mod. Phys.* **65**, 851 (1993).
- [2] L. Berthier and J. Kuchan, “Non-equilibrium glass transitions in driven and active matter,” *Nat. Phys.* **9**, 310–314 (2013).
- [3] J. Prost, F. Jülicher, and J.-F. Joany, “Active gel physics,” *Nat. Phys.* **11**, 111–117 (2015).
- [4] H. van Amerongen, L. Valkunas, and R. van Grondelle, *Photosynthetic Excitons* (World Scientific, Singapore, 2000).
- [5] D. R. Barbero and U. Steiner, “Nonequilibrium Polymer Rheology in Spin-Cast Films,” *Phys. Rev. Lett.* **102**, 248303 (2009).
- [6] S. Diehl, E. Rico, M. Baranov, and P. Zoller, “Topology by dissipation in atomic quantum wires,” *Nat. Phys.* **7**, 971 (2011).
- [7] M. Müller *et al.*, “,” *Adv. Atom. Mol. Opt. Phys.* **61**, 1 (2012).
- [8] T. Lee, S. Gopalakrishnan, and M. Lukin, “Unconventional Magnetism via Optical Pumping of Interacting Spin Systems,” *Phys. Rev. Lett.* **110**, 257204 (2013).
- [9] T. Ramos *et al.*, “Quantum Spin Dimers from Chiral Dissipation in Cold-Atom Chains,” *Phys. Rev. Lett.* **113**, 237203 (2014).
- [10] J. J. Mendoza-Arenas *et al.*, “Beyond mean-field bistability in driven-dissipative lattices: Bunching-antibunching transition and quantum simulation,” *Phys. Rev. A* **93**, 023821 (2016).
- [11] J. Eisert, M. Friesdorf, and C. Gogolin, “Quantum many-body systems out of equilibrium,” *Nat. Phys.* **11**, 124–130 (2015).

- 
- [12] G. Rempe *et al.*, “Optical bistability and photon statistics in cavity quantum electrodynamics,” *Phys. Rev. Lett.* **67**, 1727 (1991).
- [13] R. Blatt and C. Roos, “Quantum simulations with trapped ions,” *Nat. Phys.* **8**, 277–284 (2012).
- [14] D. S. Lobser, A. E. S. Barentine, E. A. Cornell, and H. J. Lewandowski, “Observation of a persistent non-equilibrium state in cold atoms,” *Nat. Phys.* **11**, 1009–1012 (2015).
- [15] I. Bloch, J. Dalibard, and W. Zwerger, “Many-body physics with ultracold gases,” *Rev. Mod. Phys.* **80** (2008).
- [16] S. Hofferberth *et al.*, “Non-equilibrium coherence dynamics in one-dimensional bose gases,” *Nature* **449**, 324–327 (2007).
- [17] T. Byrnes, N. Y. Kim, and Y. Yamamoto, “Exciton–polariton condensates,” *Nat. Phys.* **10**, 803–813 (2014).
- [18] G. Tan *et al.*, “Non-equilibrium processing leads to record high thermoelectric figure of merit in pbte–srte,” *Nat. Comm.* **7** (2016).
- [19] S. Biswas *et al.*, “Non-equilibrium induction of tin in germanium: towards direct bandgap  $ge_{1-x}sn_x$  nanowires,” *Nat. Comm.* **7** (2016).
- [20] S. Mann, “Self-assembly and transformation of hybrid nano-objects and nanostructures under equilibrium and non-equilibrium conditions,” *Nature Materials* **8**, 781–792 (2009).
- [21] V. V. Bel’kov *et al.*, “Pattern formation in semiconductors,” *Nature* **397** (1999).
- [22] M. Saffman, T. Walker, and K. Mølmer, “Quantum information with Rydberg atoms,” *Rev. Mod. Phys.* **82**, 2313 (2010).
- [23] T. Lahaye, C. Menotti, L. Santos, M. Lewenstein, and T. Pfau, “The physics of dipolar bosonic quantum gases,” *Rep. Prog. Phys.* **72**, 126401 (2009).
- [24] I. Lesanovsky and J. P. Garrahan, “Kinetic Constraints, Hierarchical Relaxation, and Onset of Glassiness in Strongly Interacting and Dissipative Rydberg Gases,” *Phys. Rev. Lett.* **111**, 215305 (2013).
- [25] I. Lesanovsky and J. P. Garrahan, “Out-of-equilibrium structures in strongly interacting Rydberg gases with dissipation,” *Phys. Rev. A (R)* **90**, 011603 (2014).
- [26] M. Marcuzzi *et al.*, “Universal Nonequilibrium Properties of Dissipative Rydberg Gases,” *Phys. Rev. Lett.* **113**, 210401 (2014).
- [27] R. Gutiérrez, J. P. Garrahan, and I. Lesanovsky, “Self-similar nonequilibrium dynamics of a many-body system with power-law interactions,” *Phys. Rev. E* **92**, 062144

- (2015).
- [28] M. Marcuzzi, J. Schick, B. Olmos, and I. Lesanovsky, “Self-similar nonequilibrium dynamics of a many-body system with power-law interactions,” *J. Phys. A: Mathematical and Theoretical* **47**, 48 (2014).
- [29] H. Schemp *et al.*, “Full Counting Statistics of Laser Excited Rydberg Aggregates in a One-Dimensional Geometry,” *Phys. Rev. Lett.* **112**, 013002 (2014).
- [30] N. Malossi *et al.*, “Full Counting Statistics and Phase Diagram of a Dissipative Rydberg Gas,” *Phys. Rev. Lett.* **113**, 023006 (2014).
- [31] A. Urvoy *et al.*, “Strongly Correlated Growth of Rydberg Aggregates in a Vapor Cell,” *Phys. Rev. Lett.* **114**, 203002 (2015).
- [32] M. M. Valado *et al.*, “Experimental observation of controllable kinetic constraints in a cold atomic gas,” *Phys. Rev. A (R)* **93**, 040701 (2016).
- [33] T. E. Lee, H. Häffner, and M. C. Cross, “Antiferromagnetic phase transition in a nonequilibrium lattice of Rydberg atoms,” *Phys. Rev. A* **84**, 031402 (2011).
- [34] M. Höning, D. Muth, D. Petrosyan, and M. Fleischhauer, “Steady-state crystallization of Rydberg excitations in an optically driven lattice gas,” *Phys. Rev. A* **87**, 023401 (2013).
- [35] J. Qian, L. Zhang, J. Zhai, and W. Zhang, “Dynamical phases in a one-dimensional chain of heterospecies Rydberg atoms with next-nearest-neighbor interactions,” *Phys. Rev. A* **92**, 063407 (2015).
- [36] J. Qian, G. Dong, L. Zhou, and W. Zhang, “Phase diagram of Rydberg atoms in a nonequilibrium optical lattice,” *Phys. Rev. A* **85**, 065401 (2012).
- [37] H. Weimer, “Variational Principle for Steady States of Dissipative Quantum Many-Body Systems,” *Phys. Rev. Lett* **114**, 040402 (2015).
- [38] V. Overbeck and H. Wiemer, “Time evolution of open quantum many-body systems,” *Phys. Rev. A* **93**, 012106 (2016).
- [39] M. F. Maghrebi and A. V. Gorshkov, “Nonequilibrium many-body steady states via Keldysh formalism,” *Phys. Rev. B* **93**, 014307 (2016).
- [40] M. Höning, W. Abdussalam, M. Fleischhauer, and T. Pohl, “Antiferromagnetic long-range order in dissipative Rydberg lattices,” *Phys. Rev. A (R)* **90**, 021603 (2014).
- [41] N. Lang and H. P. Büchler, “Exploring quantum phases by driven dissipation,” *Phys. Rev. A* **92**, 012128 (2015).
- [42] B. Vermesch *et al.*, “Dynamical preparation of laser-excited anisotropic Rydberg

- crystals in 2D optical lattices,” *New journal of Physics* **17**, 013008 (2015).
- [43] C.-K. Chan, T. E. Lee, and S. Gopalakrishnan, “Limit-cycle phase in driven-dissipative spin systems,” *Phy. Rev. A (R)* **91**, 051601 (2015).
- [44] C. Ates, B. Olmos, J. P. Garrahan, and I. Lesanovsky, “Dynamical phases and intermittency of the dissipative quantum Ising model,” *Phys. Rev. A* **85**, 043620 (2012).
- [45] A. hu, T. E. Lee, and C. W. Clark, “Spatial correlations of one-dimensional driven-dissipative systems of Rydberg atoms,” *Phys. Rev. A* **88**, 053627 (2013).
- [46] J. V. Hernández and F. Robicheaux, “Simulation of a strong van der Waals blockade in a dense ultracold gas,” *J. Phys. B* **41**, 4 (2008).
- [47] D. W. Schönleber, M. Gärttner, and J. Evers, “Coherent versus incoherent excitation dynamics in dissipative many-body Rydberg systems,” *Phys. Rev. A* **89**, 203002 (2014).
- [48] J. Honer, R. Löw, H. Weimer, T. Pfau, and H. P. Büchler, “Artificial Atoms Can Do More Than Atoms: Deterministic Single Photon Subtraction from Arbitrary Light Fields,” *Phy. Rev. Lett* **107**, 093601 (2011).
- [49] J. V. Hernández and F. Robicheaux, “Simulations using echo sequences to observe coherence in a cold Rydberg gas,” *J. Phys. B* **41**, 19 (2008).
- [50] Z. Kurucz, J. H. Wesenberg, , and K. Mølmer, “Spectroscopic properties of inhomogeneously broadened spin ensembles in a cavity,” *Phys. Rev. A* **83**, 053852 (2011).
- [51] D. Petrosyan and M. Fleischhauer, “Quantum Information Processing with Single Photons and Atomic Ensembles in Microwave Coplanar Waveguide Resonators,” *Phys.Rev. Lett.* **100**, 170501 (2009).
- [52] D. Petrosyan, G. Bensky, G. Kurizki, I. Mazets, J. Majer, and J. Schiedmayer, “Reversible state transfer between superconducting qubits and atomic ensembles,” *Phys.Rev. A (R)* **79**, 040304 (2009).
- [53] S. Hogan *et al.*, “Driving Rydberg-Rydberg transitions from a Coplanar Microwave waveguide,” *Phys. Rev. Lett.* **108**, 063004 (2012).
- [54] J. Pritchard, J. A. Isaacs, M. A. Beck, R. McDermott, and M. Saffman, “Hybrid atom-photon quantum gate in a superconducting microwave resonator,” *Phys.Rev. A (R)* **89**, 010301 (2014).
- [55] L. Sárkanány, J. Fortágh, and D. Petrosyan, “Long-range quantum gate via Rydberg states of atoms in a thermal microwave cavity,” *Phys.Rev. A (R)* **92**, 030303 (2015).
- [56] J. M. Raimond, M. Brune, and S. Haroche, “Colloquium: Manipulating quantum



- entanglement with atoms and photons in a cavity,” *Rev. Mod. Phys.* **73**, 565–582 (2001).
- [57] M. Brune *et al.*, “Quantum Rabi Oscillation: A Direct Test of Field Quantization in a Cavity,” *Phys. Rev. Lett.* **76**, 11 (1996).
- [58] G. Rempe, H. Walther, and N. Klein, “Observation of Quantum Collapse and Revival in a One-Atom Maser,” *Phys. Rev. Lett.* **58**, 4 (1987).
- [59] D. Meschede, H. Walther, and G. Müller, “One-Atom Maser,” *Phys. Rev. Lett.* **54**, 6 (1985).
- [60] H. Hatterman *et al.*, “Detrimental adsorbate fields in experiments with cold Rydberg gases near surfaces,” *Phys. Rev. A* **86**, 022511 (2012).
- [61] J. Carter and J. D. D. Martin, “Coherent manipulation of cold Rydberg atoms near the surface of an atom chip,” *Phys. Rev. A* **88**, 043429 (2013).
- [62] L. A. Jones, J. D. Carter, and J. D. D. Martin, “Rydberg atoms with a reduced sensitivity to dc and low-frequency electric fields,” *Phys. Rev. A* **87**, 023423 (2013).
- [63] J. Carter, O. Chery, and J. D. D. Martin, “Electric-field sensing near the surface microstructure of an atom chip using cold Rydberg atoms,” *Phys. Rev. A* **86**, 053401 (2012).
- [64] K. Chan, M. Siercke, C. Hufnagel, and R. Dumke, “Adsorbate electric fields on a cryogenic atom chip,” *Phys. Rev. Lett.* **112** (2014).
- [65] T. Thiele *et al.*, “Manipulating rydberg atoms close to surfaces at cryogenic temperatures,” *Phys. Rev. A* **90** (2014).
- [66] C. Hermann-Avigliano *et al.*, “Long coherence times for Rydberg qubits on a superconducting atom chip,” *Phys. Rev. A (R)* **90**, 040502 (2014).
- [67] H. Weimer, R. Löw, T. Pfau, and H. P. Büchler, “Quantum Critical Behavior in Strongly Interacting Rydberg Gases,” *Phys. Rev. Lett.* **101**, 250601 (2008).
- [68] S. Ji, C. Ates, and I. Lesanovsky, “Two-dimensional Rydberg Gases and the Quantum Hard-Squares Model,” *Phys. Rev. Lett.* **107**, 060406 (2011).
- [69] T. F. Gallagher, *Rydberg atoms (Cambridge Monographs on Atomic, Molecular and Chemical Physics)*, 1st ed., ISBN 0521385318 (Cambridge University Press, 1994).
- [70] I. I. Beterov *et al.*, “Quasiclassical calculations of BB,” *Phys. Rev. A* **79**, 052504 (2009).
- [71] A. Dalgarno, *Rydberg atoms in astrophysics*, isbn 9780521189736 ed., edited by R. F. Stebbing and F. B. Dunning (Cambridge University Press, 1983).

- [72] Y. N. Gnedin *et al.*, “Rydberg atoms in astrophysics,” *New astronomy reviews* **53**, 259–265 (2009).
- [73] G. Vitrant *et al.*, “Rydberg to plasma evolution in a dense gas of very excited atoms,” *J. Phys. B: Atom. Molec. Phys*, **15**, L49–55 (1982).
- [74] T. Killian, T. Pattard, T. Pohl, and J. M. Rost, “Ultracold neutral plasmas,” *Physics reports* **449**, 77–130 (2007).
- [75] T. Pohl, C. S. Adams, and H. R. Sadeghpour, “Cold rydberg gases and ultra-cold plasmas.” *J. Phys. B: Atom. Molec. Phys*, **44**, 180201 (2011).
- [76] S. Sevincli, “Nonlocal nonlinear optics in cold rydberg gases,” *Phy. Rev. Lett.* **107** (2011).
- [77] T. Peyronel *et al.*, “Quantum nonlinear optics with single photons enabled by strongly interacting atoms,” *Nature* **488**, 57 (2012).
- [78] A. V. Gorshkov, R. Nath, and T. Pohl, “Dissipative many-body quantum optics in rydberg media,” *Phy. Rev. Lett.* **110** (2013).
- [79] C. Murray and T. Pohl, *Quantum and Nonlinear Optics in Strongly Interacting Atomic Ensembles*, edited by E. Arimondo, C. C. Lin, and S. F. Yelin, Vol. **65** (Zoe Kruze - Elsevier, 2016).
- [80] R. Löw *et al.*, “An experimental and theoretical guide to strongly interacting rydberg gases,” *J. Phys. B: Atom. Molec. Phys*, **45**, 113001 (2012).
- [81] M. D. Lukin, “Dipole blockade and quantum information processing in mesoscopic atomic ensembles,” *Phys. Rev. Lett.* **87** (2001).
- [82] D. Comparat and P. Pillet, “Dipole blockade in a cold rydberg atomic sample [invited],” *J. Opt. Soc. Am. B* **27**, A208 (2010).
- [83] H. Weimer *et al.*, “A rydberg quantum simulator,” *Nat. Phys.* **6**, 382 (2010).
- [84] I. Bloch, J. Dalibard, and S. Nascimbéne, “Quantum simulations with ultracold quantum gases,” *Nat. Phys.* **8** (2012).
- [85] R. Blatt, I. Bloch, I. Cirac, and P. Zoller, “Quantum simulation - an exciting adventure,” *Annalen der Physik* **525**, A153–A154 (2013).
- [86] P. Schauss *et al.*, “Observation of spatially ordered structures in a two-dimensional Rydberg gas,” *Nature* **491**, 87 (2012).
- [87] P. Schauss *et al.*, “Crystallisation in ising quantum magnets,” *Science* **347**, 1455–1458 (2015).

- [88] J. Zeiher *et al.*, “Many-body interferometry of rydberg-dressed spin lattice,” *Nat. Phys.* **3835** (2016).
- [89] H. S. Friedrich, *Theoretical Atomic Physics*, 3rd ed., ISBN 9783642065033 (Springer, 2010).
- [90] M. Marinescu, H. R. Sadeghpour, and A. Dalgarno, “Dispersion coefficients for alkali-metal dimers,” *Phy. Rev. A* **49** (1994).
- [91] M. Weidemüller and C. Zimmermann, *Cold atoms and Molecules*, 1st ed., ISBN 9783527407507 (Wiley-VCH, 2009).
- [92] W. Li, I. Mourachko, M. W. Noel, and T. F. Gallagher, “Milimeter-wave spectroscopy of cold rb rydberg atoms in a magneto-optical trap: Quantum defects of the ns, np, and nd series,” *Phy. Rev. A* **67** (2003).
- [93] J. Han, “Rb *nf* quantum defects from milimeter-wave spectroscopy of cold <sup>86</sup>rb rydberg atoms,” *Phy. Rev. A* **74** (2006).
- [94] R. G. Hulet and D. Kleppner, “Rydberg atoms in "circular" states,” *Phys. Rev. Lett.* **51** (1983).
- [95] A. Messiah, *Quantum Mechanics. Two volumes Bound as One*, ISBN 0486409244 (Dover Publications, Inc., 1999).
- [96] J. D. Pritchard, *Cooperative Optical Non-linearity in a blockaded Rydberg Ensemble*, Ph.D. thesis, Department of Physics, Durham University (2011).
- [97] J. O. Day, E. Brekke, and T. G. Walker, “Dynamics of low-density ultracold rydberg gases,” *Phy. Rev. A* **77** (2008).
- [98] C. Kittel and H. Kroemer, *Thermal Physics* (Freeman, New York, 1980).
- [99] C. S. Hofmann, “An experimental approach for investigating many-body phenomena in rydberg-interacting quantum systems,” *Front. Phys.* **9**, 571–586 (2013).
- [100] K. Singer, J. Stanojevic, M. Weidemüller, and R. Côté, “Long-range interactions between alkali rydberg atoms pairs correlated to the ns-ns, np-np and nd-nd asymptotes,” *J. Phys. B: Atom. Molec. Phys.* **38**, S295 (2005).
- [101] R. van Bijnen, *Quantum engineering with ultracold atoms*, Ph.D. thesis, Technische Universiteit Eindhoven (2013).
- [102] N. Henkel, *Rydberg-dressed Bose-Einstein condensates*, Ph.D. thesis, Technische Universität Dresden (2013).
- [103] P. Avan and C. Cohen-Tannoudji, “One-Atom Maser,” *J. Phys. B: Atom. Molec. Phys.* **10**, 2 (1977).

- 
- [104] M. Sargent, M. Scully, and W. E. L. Jr., *Laser Physics* (Addison Wesley, 1974) p. 311.
- [105] H.-P. Breuer and F. Petruccione., *The theory of open quantum systems* (Oxford University Press, 2002).
- [106] C. Ates, T. Pohl, T. Pattard, and J. M. Rost, “Antiblockade in Rydberg Excitation of an Ultracold Lattice Gas,” *Phys. Rev. Lett* **98**, 023002 (2007).
- [107] B. Olmos, I. Lesanovsky, and J. P. Garrahan, “Out-of-equilibrium evolution of kinetically constrained many-body quantum systems under purely dissipative dynamics,” *Phys. Rev. E* **90**, 042147 (2014).
- [108] M. Mattioli, A. Glätzle, and W. Lechner, “From classical to quantum non-equilibrium dynamics of Rydberg excitations in optical lattices,” *New Journal of Physics* **17**, 113039 (2015).
- [109] A. M. Fox, *Quantum optics: an introduction* (Oxford University Press, 2006).
- [110] R. H. Dicke, “Coherence in spontaneous radiation processes,” *Phys. Rev.* **93** (1954).
- [111] H. Labuhn *et al.*, “A highly-tunable quantum simulator of spin systems using two-dimensional arrays of single Rydberg atoms,” arxiv **509.0454** (2015).
- [112] P. C. Hohenberg and B. I. Halperin, “Theory of dynamic critical phenomena,” *Rev. Mod. Phys.* **49**, 435–479 (1977).
- [113] S. Diehl *et al.*, *Phys. Rev. Lett.* **105** (2010).
- [114] M. Müller *et al.*, “Prospects for fast Rydberg gates on an atom chip,” *Quantum Information Processing* **10**, 771–792 (2011).
- [115] K. Molmer, Y. Castin, and J. Dalibard, “Monte Carlo wave-function method in quantum optics,” *Journal of Optical Society of America B* **93**, 030524 (1993).
- [116] H. J. Carmichael, *An open systems approach to quantum optics* (Springer, 1993).
- [117] R. Dum, P. Zoller, and H. Ritsch, “Monte carlo simulation of the atomic master equation for spontaneous emission,” *Phy. Rev. A* **45**, 4879–4887 (1992).
- [118] J. Dalibard, Y. Castin, and K. Molmer, “Wave-function approach to dissipative processes in quantum optics,” *Phy. Rev. Lett.* **68** (1992).
- [119] E. Arimondo, “Coherent population trapping in laser spectroscopy,” *Prog. Opt.* **35** (1996).
- [120] A. I. M. Fleischhauer and J. P. Marangos, “Electromagnetically induced transparency: Optics in coherent media,” *Rev. Mod. Phys.* **77** (2005).

- 
- [121] O. Kocharovskaya, “Amplification and lasing without inversion,” *Phys. Rep.* **219** (1992).
- [122] G. Alzetta *et al.*, “An experimental method for the observation of r.f. transitions and laser beat resonances in oriented sodium vapour,” *Nuovo Cimento Soc. Ital. Fis. B* **36** (1976).
- [123] K. Singer *et al.*, “Suppression of excitation and spectral broadening induced by interactions in a cold gas of Rydberg atoms,” *Phys. Rev. Lett.* **93** (2004).
- [124] T. C. Liebisch *et al.*, “Atom counting statistics in ensembles of interacting Rydberg atoms,” *Phys. Rev. Lett.* **95** (2005).
- [125] C. Ates, T. Pohl, T. Pattard, and J. M. Rost, “Many-body theory of excitation dynamics in an ultracold Rydberg gas,” *Phys. Rev. A* **76**, 013413 (2007).
- [126] C. Cohen-Tannoudji *et al.*, *Atom-Photon interactions: Basic Processes and Applications* (John Wiley and Sons, 1992).
- [127] C. Ates, S. Sevincli, and T. Pohl, “Electromagnetically induced transparency in strongly interacting Rydberg gases,” *Phys. Rev. A* **83**, 041802 (2011).
- [128] K. P. Heeg, M. Gärttner, and J. Evers, “Hybrid model for Rydberg gases including exact two-body correlations,” *Phys. Rev. A* **86**, 063421 (2012).
- [129] L. R. Wilcox and W. E. Lamb, “Fine structure of short-lived states of hydrogen by a microwave-optical method. ii,” *Phys. Rev.* **119** (1960).
- [130] P. Pearce and K. Seaton, “A classical theory of hard squares,” *J. Stat. Phys.* **53**, 1061–1072 (1988).
- [131] J. Sanders *et al.*, “Wireless network control of interacting Rydberg atoms,” *Phys. Rev. Lett.* **112** (2014).
- [132] M. O. Scully and M. S. Zubairy, *Quantum Optics* (Cambridge University Press, 1997).
- [133] H. Schempp *et al.*, “Coherent Population Trapping with Controlled Interparticle Interactions,” *Phys. Rev. Lett.* **104**, 173602 (2010).
- [134] A. Schwarzkopf, D. A. Anderson, N. Thaicharoen, and G. Raithel, “Spatial correlations between Rydberg atoms in an optical dipole trap,” *Phys. Rev. A* **88**, 061406 (2013).
- [135] J. Nipper *et al.*, “Atomic Pair-State Interferometer: Controlling and Measuring an Interaction-Induced Phase Shift in Rydberg-Atom Pairs,” *Phys. Rev. X* **2**, 031011 (2012).
- [136] M. Viteau *et al.*, “Cooperative Excitation and Many-Body Interactions in a Cold

- Rydberg Gas,” *Phys. Rev. Lett.* **109**, 053002 (2012).
- [137] J. D. Pritchard *et al.*, “Cooperative Atom-Light Interaction in a Blockaded Rydberg Ensemble,” *Phys. Rev. Lett.* **105**, 193603 (2010).
- [138] Y. Dudin and A. Kuzmich, “Strongly Interacting Rydberg Excitations of a Cold Atomic Gas,” *Science* **336**, 887 (2012).
- [139] D. Maxwell *et al.*, “Storage and Control of Optical Photons Using Rydberg Polaritons,” *Phys. Rev. Lett.* **110**, 103001 (2013).
- [140] S. E. Anderson, K. C. Younge, and G. Raithel, “Trapping Rydberg Atoms in an Optical Lattice,” *Phys. Rev. Lett.* **107**, 263001 (2011).
- [141] T. Fukuhara *et al.*, “Microscopic observation of magnon bound states and their dynamics,” *Nature* **502**, 76 (2013).
- [142] L. beguin *et al.*, “Direct Measurement of the van der Waals Interaction between Two Rydberg Atoms,” *Phys. Rev. Lett.* **110**, 263201 (2013).
- [143] Y. Nakamura *et al.*, “Coherent control of macroscopic quantum states in a single-cooper-pair box,” *Nature* **398** (1999).
- [144] D. Vion *et al.*, “Manipulating the quantum state of an electrical circuit,” *Science* **296** (2002).
- [145] J. R. Friedman *et al.*, “Quantum superposition of distinct macroscopic states,” *Nature* **406** (2000).
- [146] C. H. van der Wal *et al.*, “Quantum superposition of macroscopic persistent-current states,” *Science* **290**, 773–7 (2000).
- [147] Y. Yu *et al.*, “Coherent temporal oscillations of macroscopic quantum states in a josephson junction,” *Science* **296**, 889–892 (2002).
- [148] Z. L. Xiang, S. Ashhab, J. Q. You, and F. Nori, “Hybrid quantum circuits: Superconducting circuits interacting with other quantum systems,” *Rev. Mod. Phys.* **85**, 623 (2013).
- [149] J. Fortagh and C. Zimmerman, “Magnetic microtraps for ultracold atoms,” *Rev. Mod. Phys.* **79**, 235 (2007).
- [150] P. Rabl, D. DeMille, J. M. Doyle, M. D. Lukin, R. J. Schoelkopf, and P. Zoller, “Hybrid quantum processors: Molecular ensembles as quantum memory for solid state circuits,” *Phys. Rev. Lett.* **97**, 033003 (2006).
- [151] J. Verdú, H. Zoubi, C. Koller, J. Majer, H. Ritsch, and J. Schmiedmayer, “Strong magnetic coupling of an ultracold gas to a superconducting waveguide cavity,” *Phys.*

- Rev. Lett. **103**, 043603 (2009).
- [152] C. O'Brien, N. Lauk, S. Blum, G. Morigi, and M. Fleischhauer, "Interfacing superconducting qubits and telecom photons via a rare-earth-doped crystal," Phys. Rev. Lett. **113**, 063603 (2014).
- [153] P. Treutlein, P. Hommelhoff, T. Steinmetz, T. W. Hänsch, and J. Reichel, "Coherence in microchip traps," Physical review letters **92**, 203005 (2004).
- [154] L. Sárkány, P. Weiss, H. Hattermann, and J. Fortágh, "Controlling the magnetic-field sensitivity of atomic-clock states by microwave dressing," Phys. Rev. A **90** (2014).
- [155] B. Kasch, H. Hattermann, D. Cano, T. E. Judd, S. Scheel, C. Zimmermann, R. Kleiner, D. Koelle, and J. Fortágh, "Cold atoms near superconductors: atomic spin coherence beyond the Johnson noise limit," New Journal of Physics **12**, 065024 (2010).
- [156] Y. Nakamura, Y. A. Pashkin, T. Yamamoto, and J. Tsai, "Charge echo in a Cooper-pair box," Physical review letters **88**, 047901 (2002).
- [157] J. Labaziewicz, Y. Ge, P. Antohi, D. Leibbrandt, K. R. Brown, and I. L. Chuang, "Suppression of heating rates in cryogenic surface-electrode ion traps," Phys. Rev. Lett. **100** (2008).
- [158] J. Bylander, S. Gustavsson, F. Yan, F. Yoshihara, K. Harrabi, G. Fitch, D. G. Cory, Y. Nakamura, J.-S. Tsai, and W. D. Oliver, "Noise spectroscopy through dynamical decoupling with a superconducting flux qubit," Nature Physics **7**, 565–570 (2011).
- [159] J. Burnett *et al.*, "Evidence for interacting two-level systems from the  $1/f$  noise of a superconducting resonator," Nat. com. **5**, 4119 (2014).
- [160] S. Scheel *et al.*, "Atomic spin decoherence near conducting and superconducting films," Phys. Rev. A **72**, 042901 (2005).
- [161] N. J. Kasdin, "Discrete simulation of colored noise and stochastic processes and  $1/f^\alpha$  power law noise generation," IEEE (1995).
- [162] M. Stoyanov, M. Gunzburger, and J. Burkardt, "Pink noise,  $1/f^\alpha$ , and their effect on solutions of differential equations," International Journal for Uncertainty Quantification **1**, 257–278 (2011).
- [163] J. D. Carter, *Electric field sensing near the surface microstructure of an atom chip using cold Rydberg atoms*, Ph.D. thesis, University of Waterloo (2013).
- [164] G. Ithier *et al.*, "Decoherence in a superconducting quantum bit circuit," Phys. Rev. B **72**, 134519 (2005).
- [165] Y. Makhlin and A. Shnirman, "Dephasing of Solid-State Qubits at Optimal Points,"

- Phys. Rev. Lett. **92**, 178301 (2004).
- [166] Kumph *et al.*, “Electric-field noise above a thin dielectric layer on metal electrodes,” *New Journal of Physics* **18**, 23020 (2016).
- [167] A. Blais *et al.*, “Cavity quantum electrodynamics for superconducting electrical circuits: An architecture for quantum computation,” *Phys. Rev. A* **69**, 062320 (2004).
- [168] R. J. Schoelkopf and S. M. Girvin, “Wiring up quantum systems,” *Nature* **451**, 664 (2008).
- [169] S. Bernon *et al.*, “Manipulation and coherence of ultra-cold atoms on a superconducting atom chip,” *Nat. Comm.* **4**, 2380 (2013).
- [170] G. Hohenester, A. Eiguren, S. Scheel, and E. A. Hinds, “Spin-flip lifetimes in superconducting atom chips: Bardeen-Cooper-Schrieffer versus Eliashberg theory,” *Phys. Rev. A* **76**, 033618 (2007).
- [171] C. Henkel, S. Pötting, and M. Wilkens, “Loss and heating of particles in small and noisy traps,” *Applied Physics B* **69**, 379–387 (1999).
- [172] M. Mackl *et al.*, “All-optical measurement of Rydberg-state lifetimes,” *Phys. Rev. A* **92**, 012517 (2015).
- [173] P. Avan and C. Cohen-Tannoudji, “One-Atom Maser,” *J. Phys. B: Atom. Molec. Phys.*, **10**, 2 (1977).
- [174] M. S. III, M. Scully, and W. E. L. Jr., *Laser Physics* (Addison Wesley, 1974) p. 311.
- [175] E. T. Jaynes and F. W. Cummings, “Comparison of quantum and semiclassical radiation theories with application to the beam maser,” *Proc. IEEE* **51**, 89 (1963).
- [176] Private communication with Rick van Bijnen.
- [177] R. Barends *et al.*, “Minimizing quasiparticle generation from stray infrared light in superconducting quantum circuits,” *Appl. Phys. Lett.* **99**, 113507 (2011).
- [178] H. Labuhn *et al.*, “A highly-tunable quantum simulator of spin systems using two-dimensional arrays of single Rydberg atoms,” *arxiv* **509.0454** (2015).
- [179] D. Barredo *et al.*, “Coherent Excitation Transfer in a Spin Chain of Three Rydberg Atoms,” *Phys. Rev. Lett.* **114**, 113002 (2015).
- [180] H. Labuhn *et al.*, “Single-atom addressing in microtraps for quantum-state engineering using Rydberg atoms,” *Phys. Rev. A* **90**, 023415 (2014).
- [181] F. Nogrette *et al.*, “Single-Atom Trapping in Holographic 2D Arrays of Microtraps with Arbitrary Geometries,” *Phys. Rev. X* **4**, 021034 (2014).



- 
- [182] D. Barredo *et al.*, “Demonstration of a Strong Rydberg Blockade in Three-Atom Systems with Anisotropic Interactions,” *Phys. Rev. Lett.* **112**, 183002 (2014).
- [183] L. beguin *et al.*, “Direct Measurement of the van der Waals Interaction between Two Rydberg Atoms,” *Phys. Rev. Lett.* **110**, 263201 (2013).
- [184] V. Y. F. Leung, A. Tauschinsky, N. J. van Druten, and R. J. C. Spreeuw, “Microtrap arrays on magnetic film atom chips for quantum information science,” *Quantum Inf Process* **10**, 955–974 (2011).
- [185] A. Tauschinsky *et al.*, “Spatially resolved excitation of Rydberg atoms and surface effects on an atom chip,” *Phys. Rev. A* **81**, 063411 (2010).
- [186] S. Whitlock, R. Gerritsma, T. Fernholz, and R. J. C. Spreeuw, “Two-dimensional array of microtraps with atomic shift register on a chip,” *New journal of Physics* **11**, 023021 (2009).
- [187] J. Schahenmayer, B. P. Lanyon, C. F. Roos, and A. J. Daley, “Entanglement growth in quench dynamics with variable range interactions,” *Phys. Rev. X* **3** (2013).
- [188] D. Porras and J. Cirac, “Effective Quantum Spin Systems with Trapped Ions,” *Phys. Rev. Lett.* **92**, 207901 (2004).
- [189] J. W. Britton *et al.*, “Engineered two-dimensional Ising interactions in a trapped-ion quantum simulator with hundreds of spins,” *Nature* **484**, 489–492 (2012).
- [190] R. Islam *et al.*, “Emergence and Frustration of Magnetism with Variable-Range Interactions in a Quantum Simulator,” *Science* **340**, 583 (2013).
- [191] P. Richerme *et al.*, “Non-local propagation of correlations in quantum systems with long-range interactions,” *Nature* **511**, 198–201 (2014).
- [192] M. Foss-Feig *et al.*, “Nonequilibrium dynamics of arbitrary-range Ising models with decoherence: An exact analytic solution,” *Phys. Rev. A* **87**, 042101 (2013).
- [193] E. Vetsch, D. Reitz, G. Sagué, R. Schmidt, S. T. Dawkins, and A. Rauschenbeutel, “Optical interface created by laser-cooled atoms trapped in the evanescent field surrounding an optical nanofiber,” *Phys. Rev. Lett.* **104**, 203603 (2010).
- [194] N. V. Corzo, B. Gouraud, A. Chandra, A. Goban, A. S. Sheremet, D. V. Kupriyanov, and J. Laurat, “Large bragg reflection from one-dimensional chains of trapped atoms near a nanoscale waveguide,” *Phys. Rev. Lett.* **117**, 133603 (2016).
- [195] A. P. J. Jansen, *An Introduction to Kinetic Monte Carlo Simulations of Surface Reactions*, ISBN: 978-3-642-29487-7, Vol. 856 (Springer, 2012).
- [196] A. Chotia, M. Viteau, T. Vogt, D. Comparat, and P. Pillet, “Kinetic monte carlo mod-

- eling of dipole blockade in rydberg excitation experiment,” *New Journal of Physics* **10** (2008).
- [197] N. Metropolis *et al.*, “Equation of state calculations by fast computing machines,” *J. Chem. Phys.* **21** (1953).
- [198] R. Gordon, “Adsorption isotherms of lattice gases by computer simulation,” *J. Chem. Phys.* **48**, 1408 (1968).
- [199] F. F. Abraham and G. W. White, *J. Appl. Phys.* **41**, 1841 (1970).
- [200] G. H. Gilmer and J. D. Weeks, “Statistical properties of steps on crystal surfaces,” *J. Chem. Phys.* **35** (1976).
- [201] A. B. Bortz, M. H. Kalos, and J. L. Lebowitz, “A new algorithm for monte carlo simulation of ising spin systems,” *J. Comp. Phys.* **17** (1975).
- [202] K. Binder, *Monte Carlo methods in Statistical Physics*, edited by K. Binder, Vol. 7 (Springer, 1979).
- [203] N. W. Ashcroft and N. D. Mermin, *Solid State Physics* (Brooks, 1976).
- [204] A. Tomadin, S. Diehl, and P. Zoller, *Phys. Rev. A* **83** (2011).

# Acknowledgements/Danksagung

I would like to thank to Prof. Jan Michael Rost for giving me an opportunity to conduct my doctoral studies at the MPI-PKS. I truly benefited from very international atmosphere and well equipped infrastructure of the institute. I would like to express my sincere gratitude to my supervisor, Dr. Thomas Pohl for his guidance not only on subject matters but also in general for research skills. As an Indonesian, I am fortunate to be in his group.

I would like to also acknowledge many of the group members with whom I have had the good fortune of discussing physics among other things. Many thanks to Adrian for his friendship and support. Georg, for teaching me how to code efficiently. Laura, it was very nice working with you. Dani, for having fruitful discussion of physics, and of course proofreading. Robert, thanks for proofreading. Michael Genkin, thanks for proofreading. Karsten, although we meet not very often, you are always willing to help me.

Many thanks to the entire IT department for their patience and constant support. Special thanks to the Guest program of the MPI-PKS, Katrin, for providing me a useful information of an immigration rule in Germany. Lastly, this thesis is dedicated to my family: my wife Grace, my daughter Zahwa and looking forward for Ziyad :), Ibu Ike, Bapak Odik, Mak Ili, Mamah, Mila, Ihsan, Sherly and Nino. Thank you for your love, understanding and support.



# Versicherung

Hiermit versichere ich, dass ich die vorliegende Arbeit ohne unzulässige Hilfe Dritter und ohne Benutzung anderer als der angegebenen Hilfsmittel angefertigt habe; die aus fremden Quellen direkt oder indirekt übernommenen Gedanken sind als solche kenntlich gemacht. Die Arbeit wurde bisher weder im Inland noch im Ausland in gleicher oder ähnlicher Form einer anderen Prüfungsbehörde vorgelegt.

Die Arbeit wurde am Max-Planck-Institut für Physik komplexer Systeme in der Abteilung „Endliche Systeme“ angefertigt und von Prof. Dr. Jan Michael Rost betreut.

Ich erkenne die Promotionsordnung der Fakultät Mathematik und Naturwissenschaften der Technischen Universität Dresden vom 01.10.2012 an.

-----

Datum

-----

Unterschrift